Spring 2009

Computational simulation of strain localization: From theory to implementation

Shouxin Wu
Louisiana Tech University

COMPUTATIONAL SIMULATION OF

STRAIN LOCALIZATION:

FROM THEORY TO IMPLEMENTATION

by

Shouxin Wu, M.S.

A Dissertation Presented in Partial Fulfillment
of the Requirements for the Degree
Doctor of Philosophy

COLLEGE OF ENGINEERING AND SCIENCE
LOUISIANA TECH UNIVERSITY

May 2009

UMI Number: 3358250

INFORMATION TO USERS

The quality of this reproduction is dependent upon the quality of the copy
submitted. Broken or indistinct print, colored or poor quality illustrations
and photographs, print bleed-through, substandard margins, and improper
alignment can adversely affect reproduction.

In the unlikely event that the author did not send a complete manuscript
and there are missing pages, these will be noted. Also, if unauthorized
copyright material had to be removed, a note will indicate the deletion.

UMI®

LOUISIANA TECH UNIVERSITY

THE GRADUATE SCHOOL
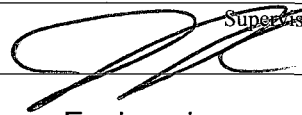
April 7, 2009
_____
Date

We hereby recommend that the dissertation prepared under our supervision

by___Shouxin Wu_____

entitled_____Computational Simulation of Strain Localization: From Theory to_____

_____Implementation_____

_____

_____

_____

be accepted in partial fulfillment of the requirements for the Degree of

Doctor of Philosophy
_____

_____
Supervisor of Dissertation Research

_____
Head of Department

Engineering
_____
Department

Recommendation concurred in:

_____

_____
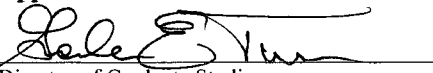
_____   Advisory Committee

_____

Approved:

_____
Director of Graduate Studies

_____
Dean of the College

Approved:

_____
Dean of the Graduate School

ABSTRACT

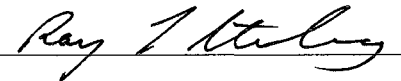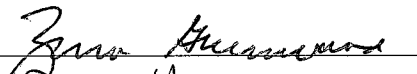Strain localization in the form of shear bands or slip surfaces has widely been observed in most engineering materials, such as metals, concrete, rocks, and soils. Concurrent with the appearance of localized deformation is the loss of overall load-carrying capacity of the material body. Because the deformation localization is an important precursor of material failure, computational modeling of the onset and growth of the localization is indispensable for the understanding of the complete mechanical response and post-peak behavior of materials and structures. Simulation results can also be used to judge the failure mechanisms of materials and structures so that the design of materials and structures can be improved.

Although the mechanisms responsible for localized deformation vary widely from one material to another, strain softening behavior is often observed to accompany the deformation localization in geotechnical materials. In this dissertation, a rate-independent strain softening plasticity model with associated flow rule and isotropic softening law is formulated within the framework of classical continuum mechanics to simulate the strain localization. A stress integration algorithm is developed to solve the nonlinear system of equations that comes from the finite element formulation of the incremental boundary value problem for linear strain softening plasticity. Two finite element programs, EP1D and EPLAS, are developed to simulate strain localization for 1-D and 2-D problems. Numerical examples show that the developed strain softening model and

computer programs can reproduce well the occurrence and development of strain localization or shear band localization.

Because the classical strain softening model does not contain a material length scale, the finite element simulation suffers from pathological mesh dependence. To regularize the mesh dependence of a classical strain softening model, gradient plasticity theory or nonlocal plasticity theory has to be used. To provide correct boundary conditions for higher-order differential constitutive equations with regard to internal state variables, a comparison of boundary conditions for gradient elasticity with gradient plasticity is carried out to show that the Dirichlet boundary condition is the correct boundary condition to force the strain to be localized into a small region and to remove the mesh-dependence.

A nonlocal plasticity model with C^0 finite elements is proposed to simulate strain localization in a mesh independent manner. This model is based on the integral-type nonlocal plasticity model and the cubic representative volumetric element (RVE). Through a truncated Taylor expansion, a mathematical relationship between an integral-type nonlocal plasticity model and a gradient plasticity model is established, which makes it possible to use the C^0 elements to approximate the internal state variable field. Variational formulae and Galerkin's equations of the two coupled fields, displacement field and plastic multiplier field, are developed based on the C^0 elements. An algorithm consisting of nonlocal elements and moving boundary technique is proposed to solve the two coupled fields. A numerical example shows the ability of the proposed model and algorithm to achieve mesh-independent simulation of strain localization.

APPROVAL FOR SCHOLARLY DISSEMINATION

The author grants to the Prescott Memorial Library of Louisiana Tech University the right to reproduce, by appropriate methods, upon request, any or all portions of this Dissertation. It is understood that "proper request" consists of the agreement, on the part of the requesting party, that said reproduction is for his personal use and that subsequent reproduction will not occur without written approval of the author of this Dissertation. Further, any portions of the Dissertation used in books, papers, and other works must be appropriately referenced to this Dissertation.

Finally, the author of this Dissertation reserves the right to publish freely, in the literature, at any time, any or all portions of this Dissertation.

Author _Shouxin Wu_

Date _April 24, 2009_

DEDICATION

To My Parents

TABLE OF CONTENTS

LIST OF TABLES

LIST OF FIGURES

ACKNOWLEDGMENTS

I would like to express my sincere gratitude and appreciation to my advisor Dr. Xingran (Jay) Wang for his invaluable advice and encouragement, and his continuous and generous support throughout my PhD studies.

I wish to express my heartfelt thanks to Dr. Raymond Sterling for his providing me the opportunity and initial financial support to study at Louisiana Tech University. I am very grateful for his kind, long-term help and advice, and I appreciate his understanding during all my years at Louisiana Tech University.

I would also like to thank Dr. David Hall for his guidance and advice in the finite element modeling using ANSYS package, and for his service on my advisory committee. My sincere gratitude is also extended to Dr. Bernd Schröder and Dr. Zeno Greenwood for their guidance and help in my course work, their kindness of serving as my advisory committee members, and their contribution in reviewing this dissertation.

I am also grateful to the staff of Prescott Memorial Library for their assistance in finding and checking out important reference materials. Special thanks go to Mr. Bob Woody for his kind help.

I also wish to express my appreciation to the staff in the Trenchless Technology Center, Department of Civil Engineering, and Office of Graduate Studies of College of Engineering and Science, for their support and help during my studies and research.

I will be forever indebted to my parents, my sister, and my brother for their unreserved support and love over all the years of my studies and research.

CHAPTER 1

INTRODUCTION

1.1 Engineering Background

It is frequently observed that deformation is concentrated in one or several narrow

zones of intense straining in the failure processes of a number of solids, such as metals

(Figure 1.1 and 1.3), concrete (Figure 1.5), rocks (Figure 1.6) [1], and soils (Figure 1.7)

[2-4]. When the behavior of these materials approaches failure, a smoothly varying

deformation pattern will change into one that involves highly localized deformations.

This phenomenon is generally called "strain localization," and it occurs in a wide range

of engineering materials. Because the strain localization generally manifests itself in the

form of shear banding, the strain localization is often called "shear band localization"

except for the idealized one-dimensional cases.

1.1.1 Localization of Deformation in Metallic Materials

Physical processes of the strain localization vary widely, depending on the types

of materials, their microstructures, loading paths and environment (temperature).

Localization of deformation in single crystal metals is a natural outcome of plastic

deformation. For cubic crystals, the plastic deformation involves a relative slip along

certain lattice planes in certain lattice directions. In face-centered cubic crystals there are

1

12 slip systems, and a yield surface vertex results from the discreteness of the slip systems. When the crystal deforms plastically, under boundary constraints, the material lattices can rotate relative to each other and thenceforth induce geometrical softening. Asaro [5] has shown that both yield surface vertex effects and geometrical softening effects contribute significantly to the localization process of single crystals. Although coarse slip bands form before the maximum load is reached, macroscopic shear bands do not form until the maximum load point after which necking occurs. Chang and Asaro [6] also have shown that the material plane of macroscopic shear bands is not aligned with the operative crystallographic slip plane (Figure 1.1(a)). The deformation is homogeneous before the maximum load point is reached.

Shear bands in high-strength, low-hardening crystals appear abruptly with very little necking, while, in low-strength, high-hardening crystals, macroscopic shear bands gradually form after considerable diffuse necking. Diffuse necking itself causes nonuniform lattice rotation, which leads to geometrical softening, and in turn advances the localization (Figure 1.1(b) and (c)) [6]. In any case, macroscopic shear bands form in the necked-down region.

For ductile metal polycrystals, Anand and Spitzig [7] have shown that shear band localization is also initiated by microstructural inhomogeneities through testing a specimen made of aged maraging steel subject to plane strain tensile loading. The deformation is still homogeneous up to the maximum load point, and no shear bands are observed prior to the onset of diffuse necking. The shear bands first form shortly after the beginning of diffuse necking with the material being still in the strain-hardening phase.

The shear bands are densely distributed near the center of the neck, and there are connected shear bands spreading diagonally across the specimen (Figure 1.1(d)) [7].
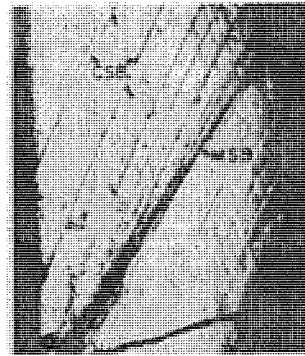
(a)

(b)
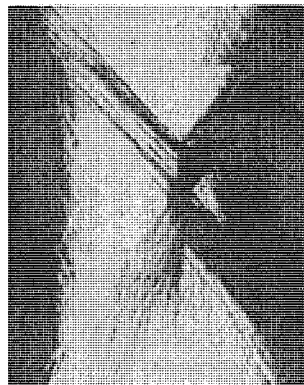
(c)
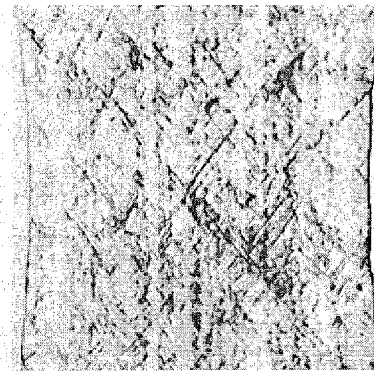
(d)

Figure 1.1 Shear bands in single crystal and polycrystalline metals: (a) shear banding in aluminum-copper single crystals; (b) shear bands in a relatively soft, high-hardening crystal; (c) shear bands in a relatively strong, low-hardening crystal; (d) shear bands in polycrystalline metals [6-7][11].

Figure 1.2 is a typical stress-strain curve for metals under uniaxial tension. In most cases, macroscopic shear bands occur at or near the peak load point B after which the load-carrying capacity of the specimen decreases with increased strain. The eventual failure mode usually involves fracture along one of these bands. The shear banding failure mode is most often observed in the plane strain tensile test, while the cup-and-

cone fracture mode is generally observed following the diffuse necking in the standard tensile test.

The Lüders bands are often observed under room temperature in impure polycrystalline body-centered cubic metals (see Figure 1.3 (a)) and some polycrystalline shape memory alloys, for example, Nitinol (see Figure 1.3 (b)). Figure 1.4 shows a typical stress-strain behavior for a polycrystalline mild steel at a constant strain rate. The Lüders bands nucleate at the upper yield point A, and is fully developed when the stress drops to the lower yield point B. From the lower yield point B on, the Lüders bands propagate along the specimen axis roughly at constant stress. When the entire sample has yielded, the plateau on the stress-strain curve terminates at the Lüders strain ε_{Lu}. From that point on, the stress will rise with increased strain, indicating that the strain hardening process proceeds (see Wang [8]).
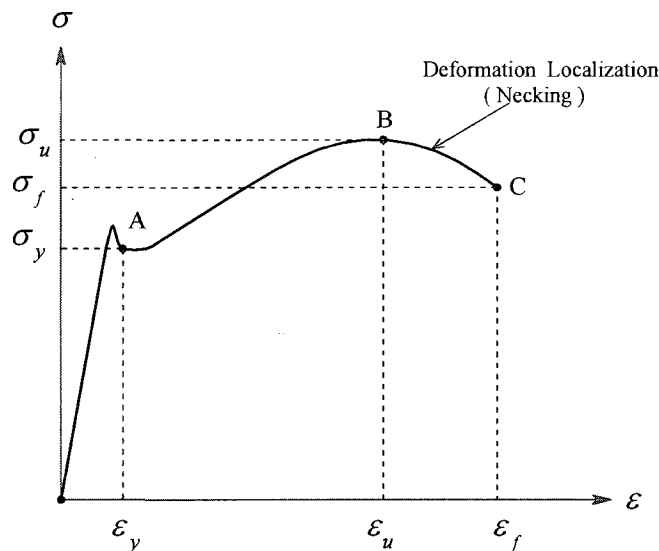
Figure 1.2 Typical stress-strain behavior for metal.

(a) (b)
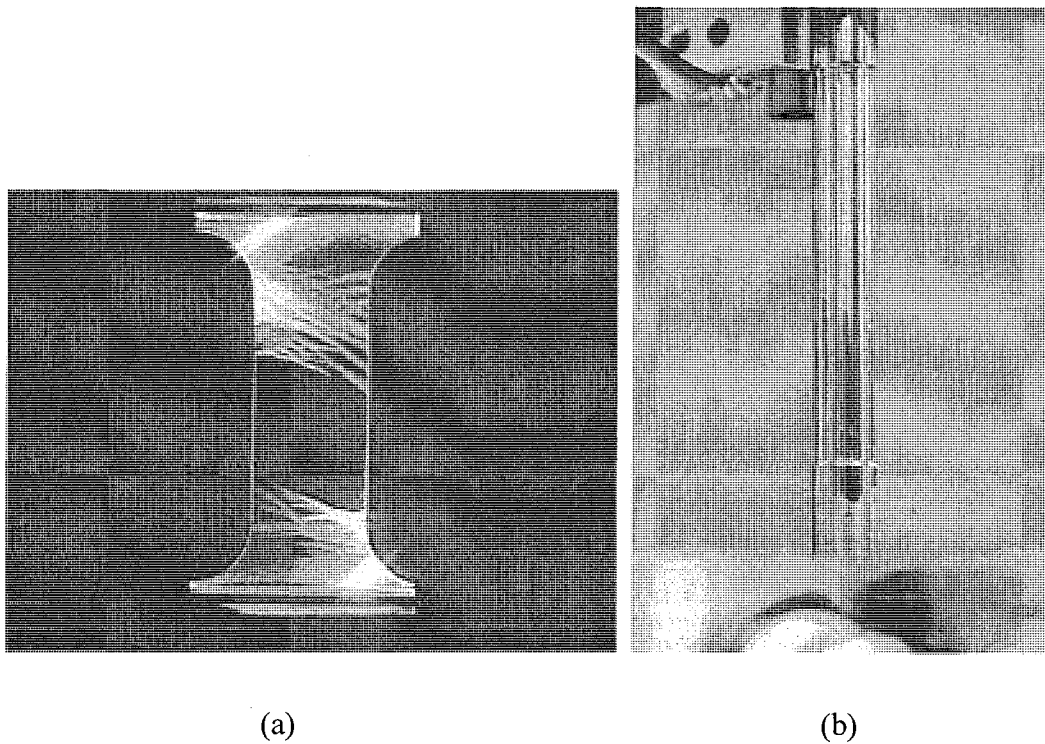
Figure 1.3 Lüders bands in metals: (a) mild steel plate (courtesy of Mike Meier, University of California, Davis); (b) Nitinol tube [17].
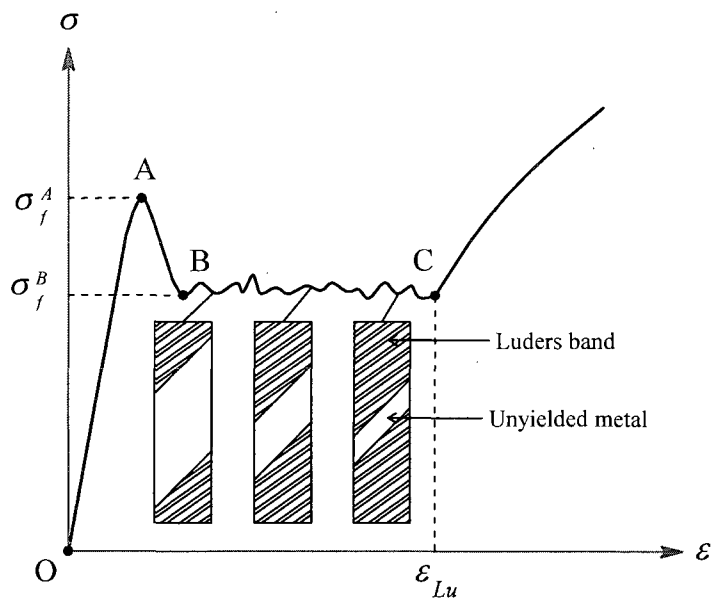
Figure 1.4 Typical stress-strain curve for Lüders band.

The Lüders bands occur in certain types of steel, such as low carbon steel (mild steel), but not in other metallic alloys, such as aluminium alloys or titanium alloys. This difference exists because plastic strain localization is normally suppressed by work hardening, which tends to make plastic flow occur rather uniformly in a metal, particularly in the early stages of plastic flow. However, there has been a lot of experimental evidence that macroscopic shear band localization frequently occurs in the necking phase of some types of metallic materials after the maximum load point is reached, as described above.

1.1.2 Localization of Deformation in Geotechnical Materials

The strain localization in geotechnical materials, such as rocks, soils, and concrete, exhibits different mechanisms from those in metallic materials. Laboratory experiments have shown that narrow bands of localized deformation are observed to form in rocks and concrete during compressive failure [13-16] (Figure 1.5). Also, the geological phenomena, for example, earth faults, provide evidence of localized deformation in rocks during the movement of the earth crust caused by such action as earthquakes (Figure 1.6). In clays and sands, shear bands often form in triaxial and plain strain compression tests (Figure 1.7 (a), (b) and (c)). Slope failure is a typical scenario of shear band localization in geotechnical engineering (Figure 1.7(d)). The occurrence of shear bands in geotechnical materials is often accompanied by the loss of the overall load-carrying capacity of the samples or structures with increased deformation after the maximum load has been reached. This phenomenon is often called "strain softening," to contrast with a phenomenon of "strain hardening" in classical plasticity.
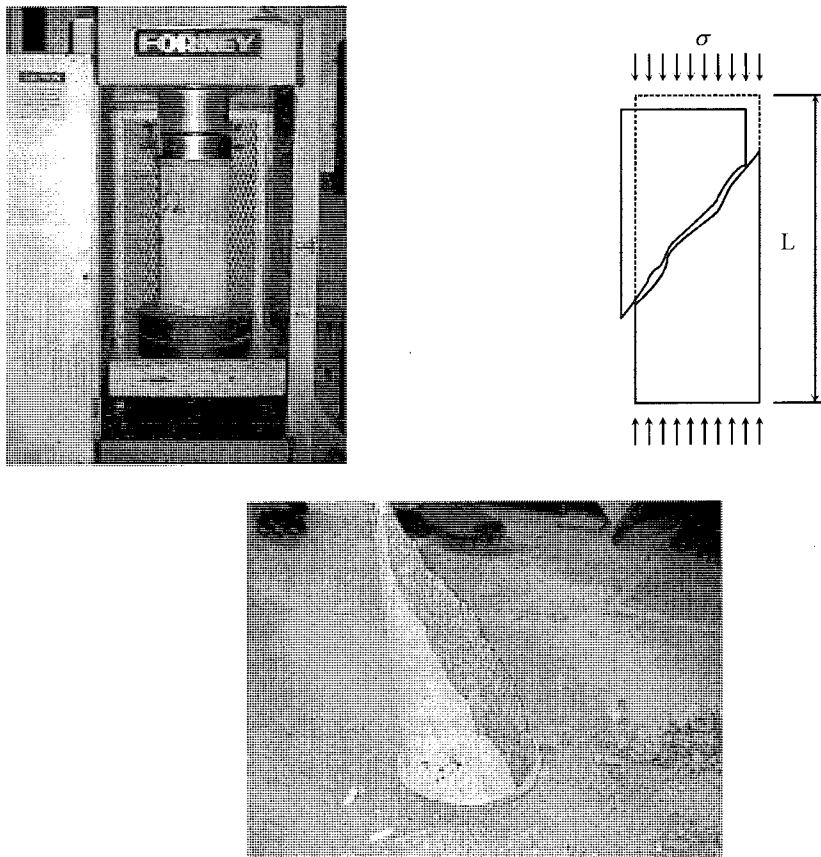
Figure 1.5 Shear bands in concrete: experimental observations.

(a)   (b)
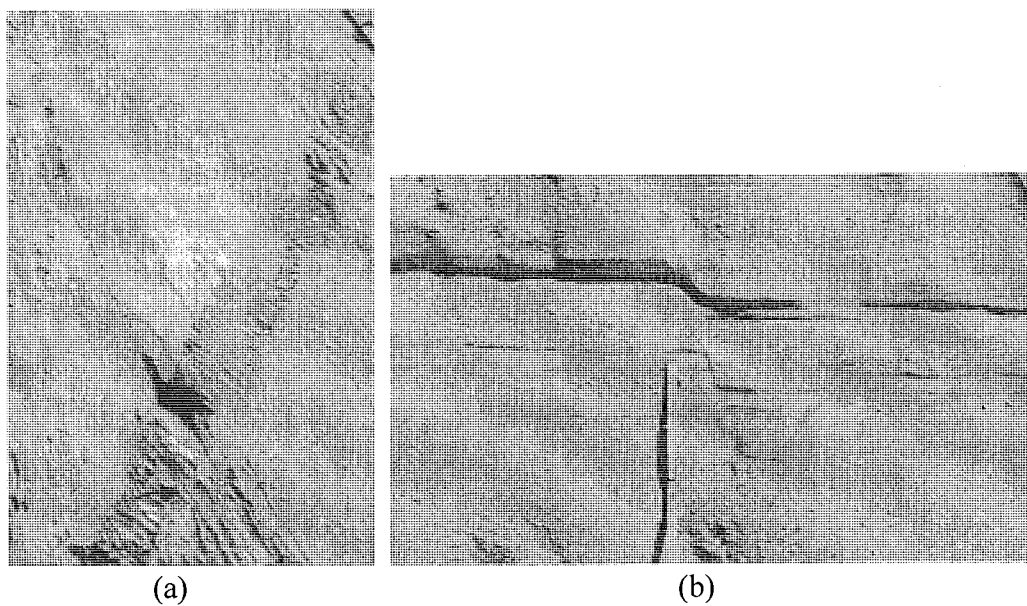
Figure 1.6 Shear bands in rocks: (a) decohesion of rock layers [4]; (b) shear band in perlite (I. Vardoulakis) [4].
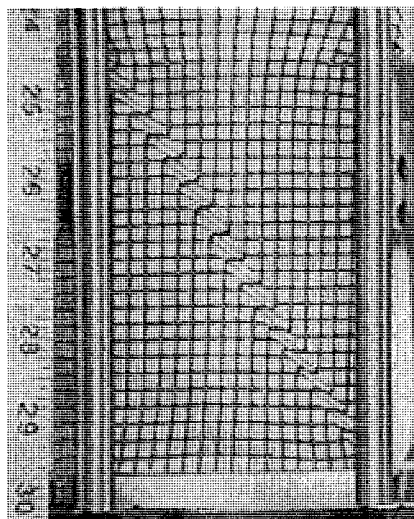
(a)   (b)

(c)   (d)

Figure 1.7 Shear bands in soils: (a) stiff clayey soil [1]; (b) silica (quartz) sand, plane strain test [2]; (c) X-ray negative plate of the shear band in cohesionless sand [10]; (d) slope failure (California 1995) [3].

The initiation and their geometrical characteristics, such as orientation and thickness, of the shear bands in geotechnical materials are strongly affected by the properties, state, and the testing conditions. In cohesive materials (for example, rocks and dense clays), formation of fracture can be observed at the onset of shear bands and the cohesive component of the shear resistance vanishes. In granular, cohesionless materials, shear band localization induces intense inter-granular slip and rotation, which in turn leads to strong dilatancy of the materials inside the localized zone [9]. Figure 1.7(c) shows an X-ray negative plate of a sand specimen (see Vardoulakis [10]). The strong localized material dilatancy due to grain rearrangement and grain rotation are the dominant micro-kinematical features of shear banding in granular materials. The increasing porosity and decreasing density reduces the number of contacts per grain in the granular assembly, resulting progressively in a weaker granular structure.

Figure 1.8 is a typical axial stress-strain curve for rocks subject to triaxial compression testing as described by Jaeger and Cook [13]. The rock material behaves nearly elastically in the first two regions, OA and AB. Loading and unloading in this region does not produce irreversible deformation. Note that from O to A, the intrinsic microcracks of the rock material close during the loading, resulting in the curve OA being slightly convex upwards. In the region from B to C (usually $\sigma_B = \frac{2}{3}\sigma_C$), irreversible deformations develop in the rock, and the slope of the stress-strain curve decreases with increasing strain. At or near the peak point C, macroscopic localization of deformation appears often in the form of a shear band. Further loading from point C leads to a descending branch of the stress-strain curve, a plausible behavior in the rock after deformation localization.
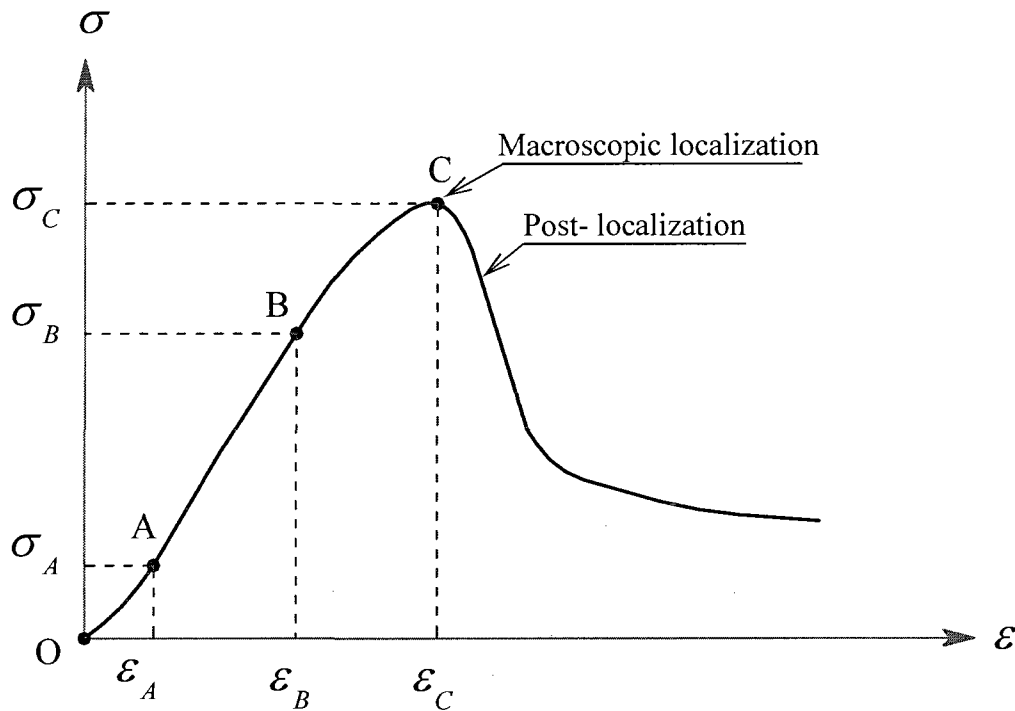
Figure 1.8 Typical axial stress-strain behavior for rock [13,15,16].

Figure 1.9 shows a typical axial stress-volumetric strain curve for the rocks [13], where the regions OA, AB, and BC correspond to the same regions as in Figure 1.8. From O to B, the volume of the rock material decreases with increasing compression, elastically but not necessarily in a linear fashion. When the stress reaches the point B, the slope of the curve begins to decrease with increasing stress, which represents an increase in volume relative to elastic contraction. This phenomenon is known as dilatancy that can be ascribed to the formation and extension of open micro-cracks within the rock specimens. The dilating proceeds from point B to point C, where macroscopic localization develops. After point C the rock continues to dilate until the final collapse or fracture of the specimen.
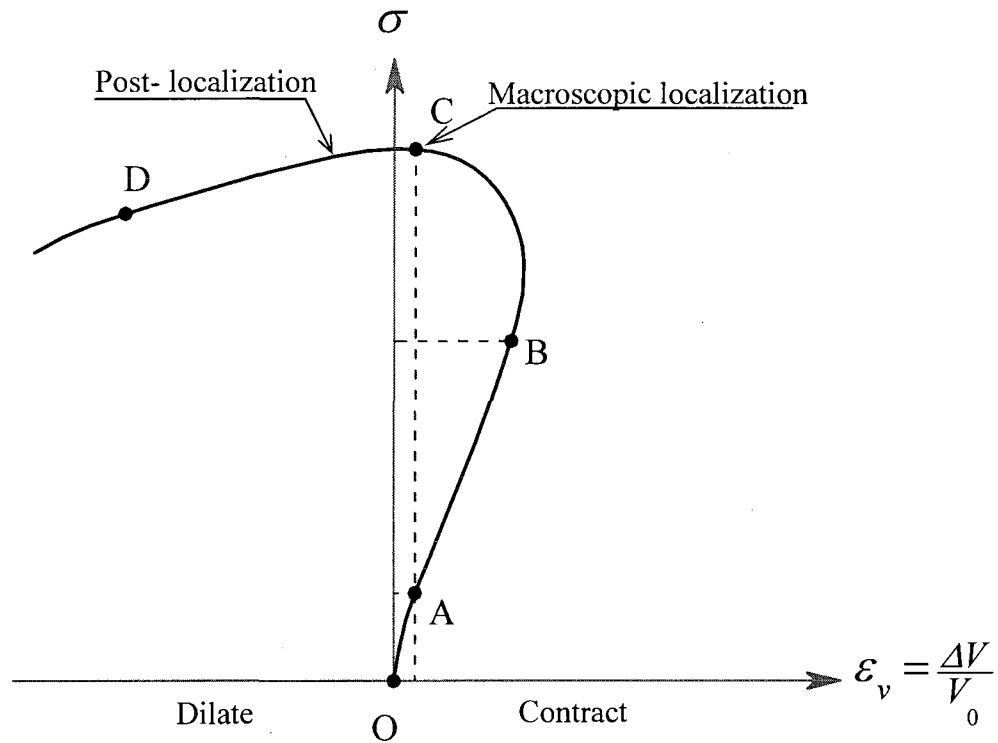
Figure 1.9 Typical axial stress-volumetric strain behavior for rock [13, 15].

Confining pressure has effects on the strength and ductility of the rock specimens [13]. When the confining pressure is increased, the maximum stress corresponding to the macroscopic localization will increase and the permanent deformation remaining in the specimens during the post-localization phase also increases.

Due to the similarities between the constituent materials and structural features of rock and concrete, the deformation mechanisms and mechanical behavior of concrete are much like those of the rock. Figure 1.10 is a typical plot of axial stress versus axial strain for concrete under uniaxial compression as described by Chen [14] and Figure 1.11 shows a typical axial stress − volumetric strain curve [14]. By comparison of Figure 1.10 with Figure 1.8 and Figure 1.11 with Figure 1.9, one can find the similarities between

these two materials. However, there are still some distinctive characteristics in the behavior of the concrete. In the region OA of Figure 1.10, the stress-strain curve is nearly linear-elastic up to about 30 percent of its maximum compressive strength f_c'. Beginning from the point A the curve shows a gradual decrease in the slope up to about $0.75 f_c'$ to $0.90 f_c'$, whereupon its slope decreases sharply and approaches zero at the peak point B. The macroscopic deformation localization forms at or near point B, after which post-localization follows and the material's behavior experiences strain softening until the final fracture. Figure 1.11 shows that the change in volume is almost linear up to about $0.75 f_c'$ to $0.90 f_c'$ (the point C), after which the volumetric change is reversed, resulting in volumetric expansion near or at f_c'. The deformation localization generally accompanies the volumetric expansion and becomes visible at point B.
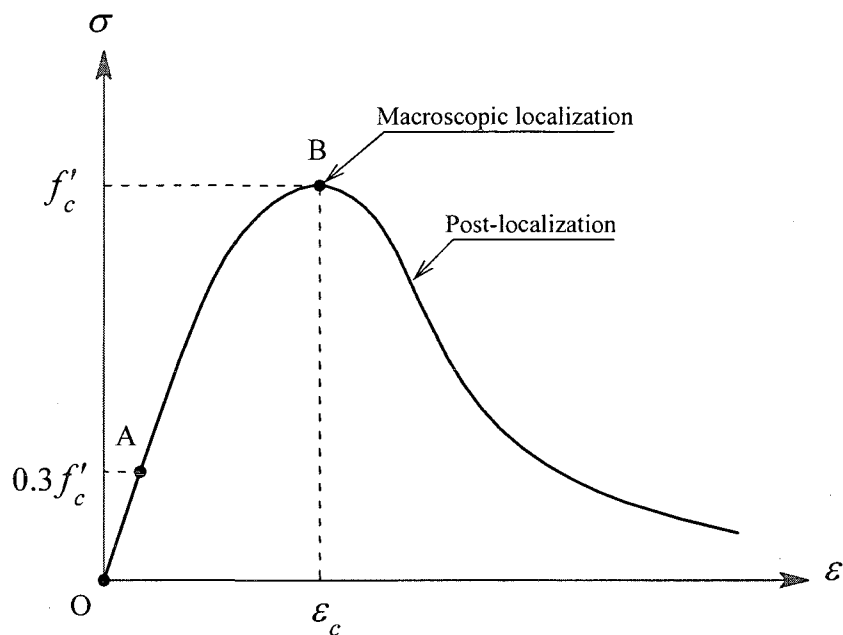
Figure 1.10 Typical axial stress-strain behavior for concrete [14,15].

$$\sigma$$

Post-localization

Macroscopic localization

B

$0.75 \sim 0.9 f_c'$

C

A

$\varepsilon_v = \dfrac{\Delta V}{V_0}$

Dilate   O   Contract
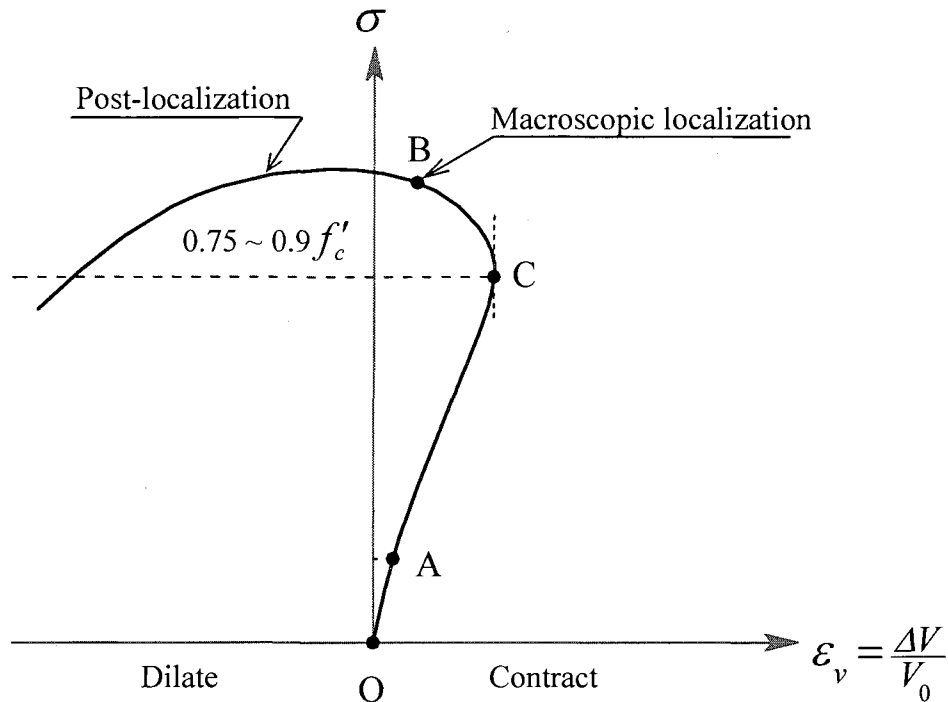
Figure 1.11 Typical axial stress-volumetric strain curve for concrete [14].

The nonlinear behavior of concrete is caused by the microcracks contained in concrete. These microcracks exist at interfaces between coarse aggregates and mortar, even before any load has been applied. Many of these microcracks are caused by segregation, shrinkage, or thermal expansion in the mortar. The propagation of these microcracks during loading contributes to the nonlinear behavior of concrete at low stress level and causes volumetric expansion near failure. Also some microcracks become the triggering factor for the localized failure modes.

The behavior of soil is more complex, depending on its nature (distribution of grain sizes and the mineralogy of the grains), state (specific volume together with the pore pressure, dry or saturated), and loading condition (drained or undrained). Figure 1.12 is a typical stress-strain response for dry soils subject to a triaxial compression test

as described by Atkinson [12]. A 'dry' soil in this context refers to dense sand and overconsolidated clay as described in [12, 16]. The response from point O to B is basically elastic, and plastic deformation is involved from point B to C. In the region BC, the soil experiences dilation as the rock does. At point C, which corresponds to the maximum load, localized deformation develops often in the form of shear bands or slip surfaces. Following the peak point C, is the post-localization region, where strain softening behavior dominates the response, and the soil arrives at its critical state at point D. Regueiro and Borja [16] noticed a difference between the "slip surface" and the "shear band" and define the "slip surface" as "a zone of localized deformation with negligible width" and the "shear band" as "a zone of localized deformation with finite width." Figure 1.13 depicts the volumetric change of the dry soil with increasing axial strain [12, 18]. The mechanism of dilatancy is related to the original arrangement of particles in soils and their movement during loading, and plays an important role in the formation of the shear band pattern.

It is noteworthy that not all soil types exhibit shear banding during the failure process, and, for some soils, other failure modes, for example, barreling and bulging, are also observed in laboratory experiments (see Read and Hegemier [15]). However, the phenomenon of strain softening in the post-peak region is almost always observed to accompany the failure processes of soils.
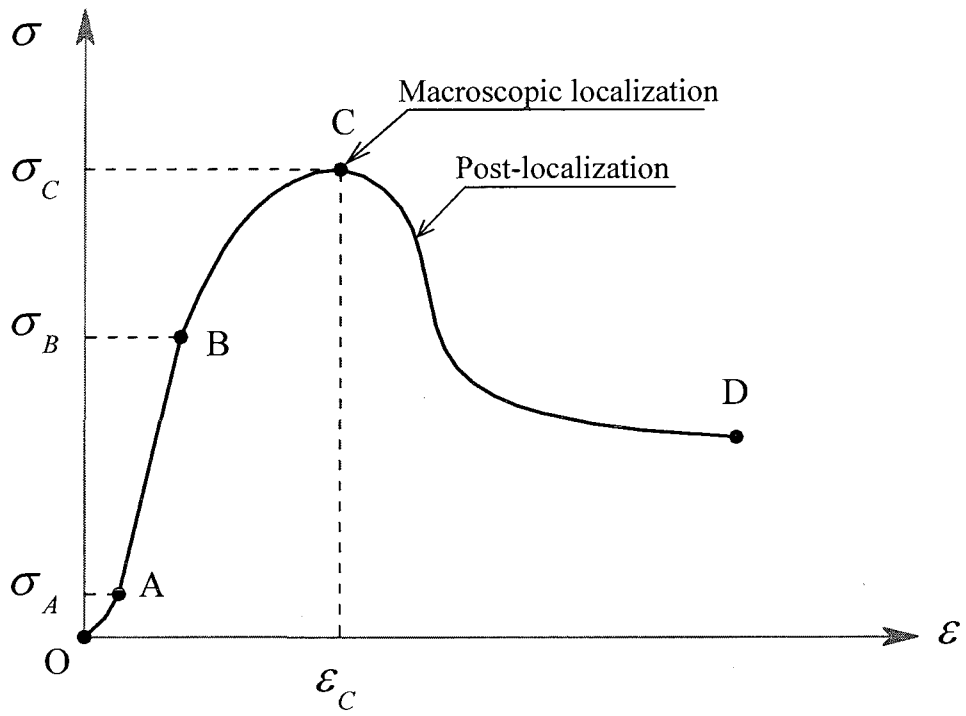
Figure 1.12 Typical axial stress-strain behavior for dry soil [12,16].
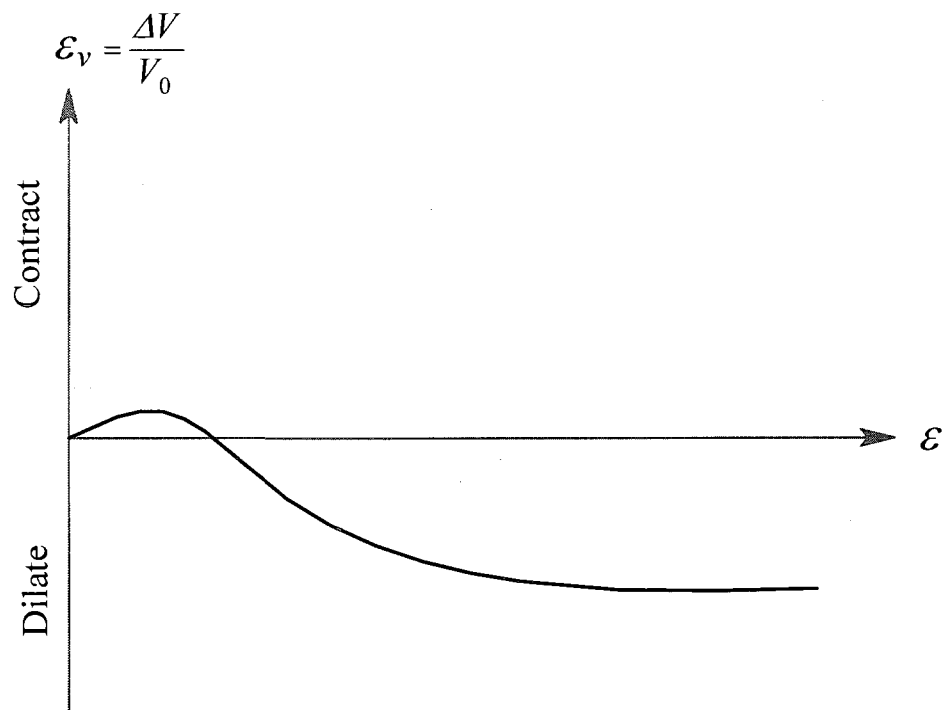
Figure 1.13 Typical volumetric strain-axial strain for dry soil [12, 16].

1.2 Research Significance

Because deformation localization is an important precursor of material failure, computational modeling of the onset (bifurcation point) and growth (post-bifurcation behavior) of the localization is indispensable for understanding the whole deformation process and the final strength of materials and structures. Also, in the simulation of a vehicle crash, lethality and vulnerability of weapons, and extreme events in critical systems such as a nuclear reactor, understanding the material behavior after the formation of localization is of great importance. Simulation results can be used to judge the mechanisms of material and structure failure so that the design of materials and structures can be improved. Good material models that can replicate the localized deformation patterns and final failure modes are in demand.

1.3 Computational Modeling of Strain Localization

1.3.1 Bifurcation and Material Instability

It is widely recognized that the localization of deformation results from material instability and is a bifurcation phenomenon [30-39]. In a nonlinear dynamic system, a bifurcation is generally defined as the change of the number of attractors when some system parameters are changed. This change is accompanied by a change of the stability of an attractor. In a bifurcation point, at least one eigenvalue of the Jacobian gets a zero real part (see Seydel [19]). From a pure mathematical point of view, Hale [20] gave the following definition of bifurcation:

Suppose that $\mathscr{X}$ and $\mathscr{Y}$ are topological spaces, $\mathscr{V} \subset \mathscr{X}$ is open, $\varXi$ is an open set in a topological space, and $f : \mathscr{V} \times \varXi \mapsto \mathscr{Y}$ is a given continuous function. Let

$$\mathscr{S} = \{(x,\xi) \in \mathscr{V} \times \varXi : f(x,\xi) = 0\} \tag{1.1}$$

be the set of solutions of the equation $f(x,\xi) = 0$. For a fixed ξ, define

$$\mathscr{S}_\xi = \{x : (x,\xi) \in \mathscr{S}\} \tag{1.2}$$

as the "cross-section" of the solution set at ξ. In a specific problem, the solution sets $\{\mathscr{S}_\xi, \xi \in \varXi\}$ can be divided into equivalence classes by means of an equivalence relation. Given the function f and an equivalence relation $\sim$, if for any neighborhood $\mathscr{W}$ of ξ_0, there are $\xi_1, \xi_2 \in \mathscr{W}$ such that $\mathscr{S}_{\xi_1} \not\sim \mathscr{S}_{\xi_2}$, the ξ_0 is called a bifurcation point for $(f, \sim)$. An example of an equivalence relation is that $\mathscr{S}_{\xi_1} \sim \mathscr{S}_{\xi_2}$ when $\mathscr{S}_{\xi_1}$ and $\mathscr{S}_{\xi_2}$ are homeomorphic.

Bifurcations occur in all types of equations. For a nonlinear differential equation depending on a set of parameters, a bifurcation point is defined as a point where the number of distinct solutions changes as the parameters change [21]. The concept of bifurcation basically implies that system behavior goes through some fundamental changes, qualitative in nature, and, as a consequence of this change, the number of critical solutions, a quantitative aspect, is changed. Many problems in engineering, such as buckling of structural members (e.g. slender columns and deep beams), or in physics, such as phase transitions, are typical examples of bifurcation phenomena.

The qualitative changes of system behavior at a bifurcation point include the changes from stable to unstable, symmetric to asymmetric, stationary to periodic motion, regular to irregular, order to chaos, etc. [19]. Several of these changes may appear simultaneously.

According to Drucker's stability postulate (see Drucker [25] and Chen [14]), a material is considered to be stable during small deformation if its stress rate and strain rate satisfy the following condition:

$$\dot{\sigma} : \dot{\varepsilon} > 0, \tag{1.3}$$

where σ is the Cauchy stress tensor and ε the strain tensor. The dot over a variable denotes the partial derivertive of that variable with respect to time (the rate of that variable) or increment of that variable, if no real time is involved at all.

The Equation (1.3) is called the stability criterion. If a material's behavior violates the stability criterion, that is

$$\dot{\sigma} : \dot{\varepsilon} < 0, \tag{1.4}$$

the material is considered to be unstable.

Strain softening is a typical unstable behavior of materials. The descending branch of a typical stress-strain curve of a material under a standard compression test represents the strain softening behavior. In the descending branch, the stress decreases with increased strain and the tangent modulus of the curve becomes negative (see Figure 1.14).

Strain softening is only one form of material instability. Compared to the definition of material stability, the material instability involves more aspects of the mathematical characterization of the material's behavior. Belytchko [23] give a general definition of material instability as *"a material is considered unstable when a perturbation applied to an infinite slab of the material in a uniform state of stress grows without bound."* This definition is consistent with the mathematical definition of the instability given by Seydel [19]. Besides the strain softening, experimental and numerical

studies showed that the yield surface vertex and the non-associative flow rule (see Figure 1.15) also cause the material to be unstable (see Tvergarrd *et al.* [22] and Belytschko and Mish [23]). Material instability is also related to such phenomena as crazing of polymers and liquefaction of granular materials.
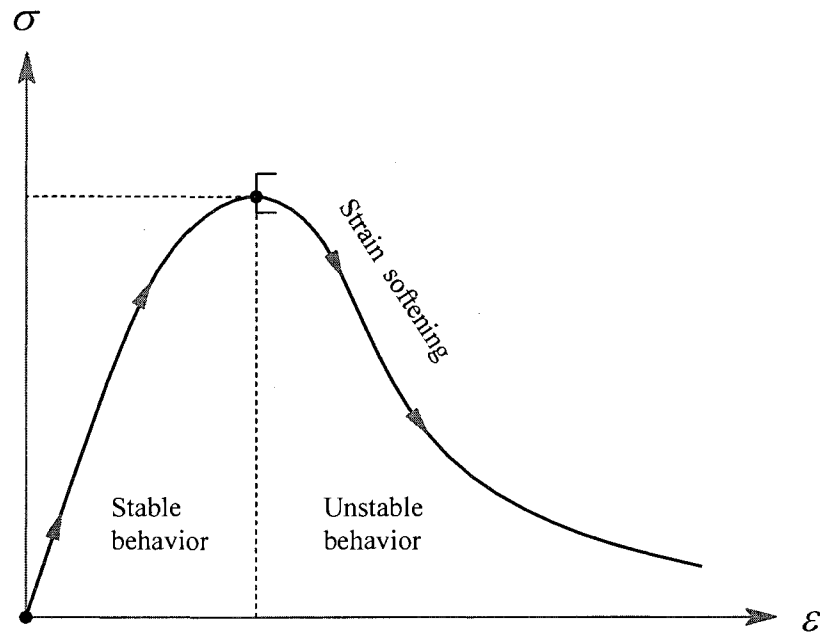
Figure 1.14 Material instability arising from strain softening.

$$\sigma_3, \dot{\varepsilon}_3^p$$

$$\dot{\boldsymbol{\varepsilon}}^p$$

Yield surface

Associative
flow rule

Nonassociative
flow rule

$$\dot{\boldsymbol{\varepsilon}}^p$$

$$\sigma_1, \dot{\varepsilon}_1^p$$

$$\sigma_2, \dot{\varepsilon}_2^p$$
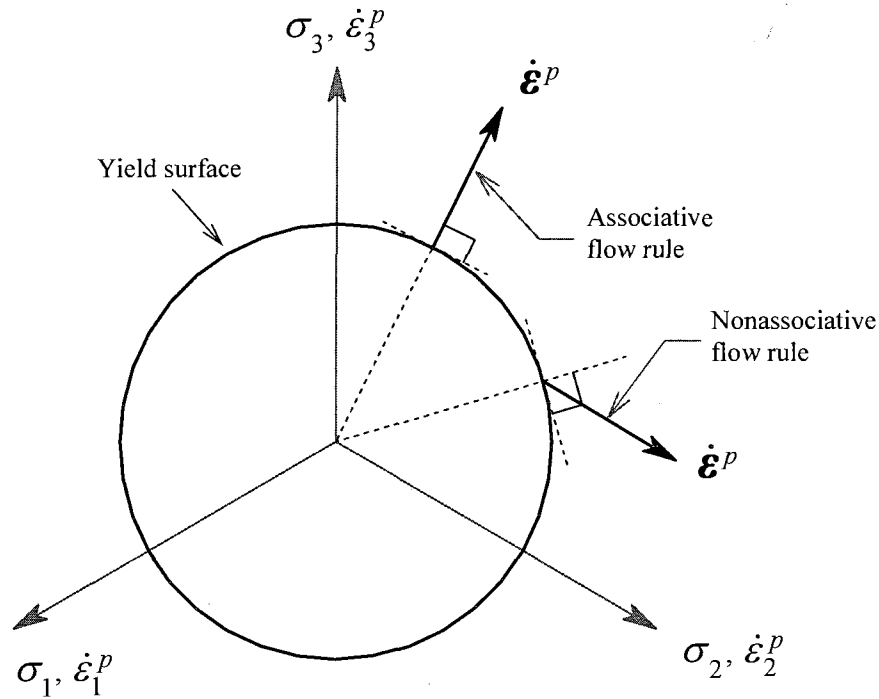
Figure 1.15 Material instability arising from nonassociative flow rule.

It is well agreed that deformation localization appears when the behavior of a material changes from stable to unstable at a bifurcation point where a homogeneous deformation pattern gives way to one of highly localized deformation patterns. Shear banding is one of these localization modes. In addition, necking, slip surface, and bulging are also frequently observed localization modes.

1.3.2 Theories for the Modeling of Strain Localization —A Brief Review

1.3.2.1 General Review

The earliest theoretic work for the modeling of the strain localization should probably be ascribed to Hadamard [24]. A generally accepted theoretical framework that associates the formation of strain localization with a material instability and a bifurcation

phenomenon is developed by Thomas [26], Hill [27], Mandel [28], and Rice [29]. These pioneering works laid the necessary conditions for the onset of strain localization and become the foundation for numerical simulation of stain localization. The fundamental points of this theoretical framework are that the onset of strain localization is associated with the loss of material stability and correspondingly, the governing incremental equilibrium equations lose ellipticity. The early numerical studies employing classical elasto-plastic constitutive equations with a smooth yield surface gave no indication of strain localization and showed that strain localization does not appear until the material behavior loses its stability (see Tvergarrd, Needleman, and Lo [22]). According to Hill's bifurcation theory [30], all forms of material instabilities may lead to deformation localization. The most common forms of material instabilities are strain softening and the non-associative flow rule, although it has been shown that yield surface vertex based on the J_2 corner theory of plasticity does initiate the strain localization in a plane strain loading test of metals [22]. For geotechnical materials, the presence of internal friction renders the plastic flow non-associative and the phenomenological incremental elasto-plastic constitutive equations become unsymmetric. Due to this lack of symmetry, the material may become unstable, and strain localization may appear, both in the strain hardening stage (see Leroy and Ortiz [31]).

1.3.2.2 Classical Discontinuous Bifurcation

Some basic principles underlying the theory of localization was first proposed by Hadamard [24] in the studies of elastic stability. Hill [28] extended Hadamard's theory to the inelastic context and developed a criterion for discontinuous bifurcation in elasto-plastic materials with associated flow rule. Hill's theory was further applied to the

analysis of discontinuous bifurcations in elasto-plastic materials with nonassociated flow rules by Mandel [27], Rice [29], Rudnicki and Rice [32], and Ottosen and Runesson [33]. These theories are reviewed and discussed comprehensively by Leroy and Ortiz et al [31], Bardet [34], Neilsen and Schreyer [35], de Borst *et al.* [36], and Tomita [37]. The following analysis summarizes the bifurcation theory developed by these authors.

Consider a homogeneous solid subjected to quasi-static, monotonic loading. Assume that material behavior is rate-independent and thermally decoupled, and the deformation is small.

Define $\boldsymbol{u}$ as the displacement field. Let $\nabla \dot{\boldsymbol{u}}$ be the displacement rate gradient, which is a second-order tensor. The matrix form of $\nabla \dot{\boldsymbol{u}}$ with respect to Cartesian coordinates is

$$[\nabla \dot{\boldsymbol{u}}] = \begin{bmatrix} \dfrac{\partial \dot{u}_1}{\partial x_1} & \dfrac{\partial \dot{u}_1}{\partial x_2} & \dfrac{\partial \dot{u}_1}{\partial x_3} \\ \dfrac{\partial \dot{u}_2}{\partial x_1} & \dfrac{\partial \dot{u}_2}{\partial x_2} & \dfrac{\partial \dot{u}_2}{\partial x_3} \\ \dfrac{\partial \dot{u}_3}{\partial x_1} & \dfrac{\partial \dot{u}_3}{\partial x_2} & \dfrac{\partial \dot{u}_3}{\partial x_3} \end{bmatrix}. \tag{1.5}$$

When a bifurcation occurs, the continuous displacement rate gradient $\nabla \dot{\boldsymbol{u}}$ becomes discontinuous across the plane of discontinuity. The jump of $\nabla \dot{\boldsymbol{u}}$ can be expressed as

$$[\![\dot{u}_{i,j}]\!] = \dot{u}_{i,j}^+ - \dot{u}_{i,j}^-, \tag{1.6}$$

where $[\![\bullet]\!]$ denotes the jump of a quantity, $(\bullet)$. $(\bullet)_{i,j} = \partial(\bullet)_i / \partial x_j$ denotes the partial derivative of the quantity $(\bullet)_i$, $i = 1, 2, 3$, with respect to variable x_j, $j = 1, 2, 3$. The superscript "$+$" and "$-$" represent the two opposite sides of the plane of discontinuity. Maxwell's compatibility condition requires that the jump $[\![\dot{u}_{i,j}]\!]$ be of the form

$$[\![\dot{u}_{i,j}]\!] = \zeta_i n_j ,\tag{1.7}$$

where ζ is an arbitrary vector and $\boldsymbol{n}$ is the normal to the plane of discontinuity. For the sake of convenience, define the unit vector $\boldsymbol{m}$ along ζ as

$$m_i = \frac{\dot{\zeta}_i}{\dot{\zeta}} ,\tag{1.8}$$

$$\dot{\zeta} = \left| \dot{\zeta} \right| ,\tag{1.9}$$

where $\left| \dot{\zeta} \right| = \sqrt{\dot{\zeta} \cdot \dot{\zeta}}$. Substituting Equation (1.8) and (1.9) into Equation (1.7) results in

$$[\![\dot{u}_{i,j}]\!] = \dot{\zeta} m_i n_j .\tag{1.10}$$

For infinitesimal deformation, the strain rate tensor $\dot{\boldsymbol{\varepsilon}}$ is related to the displacement rate gradient by

$$\dot{\boldsymbol{\varepsilon}} = \frac{1}{2}\left(\nabla \dot{\boldsymbol{u}} + \left(\nabla \dot{\boldsymbol{u}} \right)^T \right).\tag{1.11}$$

Applying Equation (1.5) and (1.10) to (1.11), the strain rate jump across the plane of discontinuity takes the form

$$[\![\dot{\boldsymbol{\varepsilon}}]\!] = \frac{1}{2}\dot{\zeta}\left(\boldsymbol{m} \otimes \boldsymbol{n} + \boldsymbol{n} \otimes \boldsymbol{m} \right),\tag{1.12}$$

where $\otimes$ denotes the tensor product of two vectors.

The strain rate in the localized zone, $\dot{\boldsymbol{\varepsilon}}_{loc}$ can be expressed as the sum of the strain rate outside the localized zone and the strain rate jump across the plane of discontinuity:

$$\dot{\boldsymbol{\varepsilon}}_{loc} = \dot{\boldsymbol{\varepsilon}}_{out} + [\![\dot{\boldsymbol{\varepsilon}}]\!],\tag{1.13}$$

where $\dot{\boldsymbol{\varepsilon}}_{out}$ represents the strain rate outside the localized zone. For continuing equilibrium, the traction rates across the discontinuity are required to be continuous, that is

$$\dot{F}_{loc} - \dot{F}_{out} = n \cdot \left(\dot{\sigma}_{loc} - \dot{\sigma}_{out}\right) = 0. \qquad (1.14)$$

For rate-independent solids the relations between stress rate and strain rate are given by

$$\dot{\sigma}_{loc} = D_{loc} : \dot{\varepsilon}_{loc}, \qquad (1.15)$$

$$\dot{\sigma}_{out} = D_{out} : \dot{\varepsilon}_{out}, \qquad (1.16)$$

where D_{loc} and D_{out} are the tangential modulus tensor for material in the localized zone and outside the localized zone, respectively. Combining equations from (1.14) to (1.16) yields

$$n \cdot \left(D_{loc} - D_{out}\right) \cdot \varepsilon_{out} + A(n) \cdot m = 0, \qquad (1.17)$$

where

$$A(n) = n \cdot D_{loc} \cdot n \qquad (1.18)$$

is the acoustic tensor. At the critical point of the bifurcation, $D_{loc} = D_{out}$, Equation (1.17) reduces to

$$A(n) \cdot m = 0. \qquad (1.19)$$

For any admissible localized deformation mode, $m \neq 0$, the necessary condition for discontinuous bifurcation is

$$\det(A(n)) = 0. \qquad (1.20)$$

The Equation (1.20) implies that the acoustic tensor $A(n)$ has a zero eigenvalue, which is a necessary condition for loss of ellipticity (see Rice [29]). The solutions of Equation (1.20), n, determine the normal to the possible plane of discontinuity and the eigenvector m, corresponding to the zero eigenvalue of $A(n)$, determines the localization mode. A numerical procedure is given by Leroy and Ortiz [31] to solve for n and m.

1.3.2.3 General Bifurcation and Loss of
Strong Ellipticity

During the derivation of the classical bifurcation criterion (1.20), two assumptions are introduced: one is that the discontinuity of the strain field in the localized zone remains kinematically compatible with the strain field outside the localized zone; another one is that the tangential modulus tensors, both inside and outside the localized zone, are identical to each other at the onset of localization [35]. The general bifurcation criterion does not have these assumptions. According to Drucker's stability postulate, Hill [30] has shown that a necessary condition for any types of bifurcations and loss of uniqueness is

$$\dot{\boldsymbol{\sigma}} : \dot{\boldsymbol{\varepsilon}} = 0 \,. \tag{1.21}$$

Equation (1.21) can also written as

$$\dot{\boldsymbol{\varepsilon}} : \dot{\boldsymbol{D}}^{sym} : \dot{\boldsymbol{\varepsilon}} = 0 \,, \tag{1.22}$$

where $\dot{\boldsymbol{D}}^{sym}$ denotes the symmetric part of the tangential modulus tensor $\dot{\boldsymbol{D}}$ and its indical form is expressed as

$$D_{ijkl}^{sym} = \frac{1}{2} \left(D_{ijkl} + D_{klij} \right). \tag{1.23}$$

For a kinematically compatible strain rate field $\dot{\boldsymbol{\varepsilon}}_{loc}$ in the localized zone, Bigoni and Hueckel [38] proposed the following general bifurcation criterion

$$\dot{\boldsymbol{\varepsilon}}_{loc} : \boldsymbol{D}^{sym} : \dot{\boldsymbol{\varepsilon}}_{loc} = 0 \,. \tag{1.24}$$

This criterion corresponds to the loss of strong ellipticity, implying that general bifurcations may appear whenever $\boldsymbol{D}^{sym}$ is not positive definite. Recall the Equation (1.17). Let $\boldsymbol{A}(\boldsymbol{n})$ be decomposed into a symmetric part $\boldsymbol{A}^{sym}(\boldsymbol{n})$ and an anti-symmetric part $\boldsymbol{A}^{uns}(\boldsymbol{n})$:

$$A(n) = A^{sym}(n) + A^{uns}(n).$$ (1.25)

If the continuity requirement on $\dot{\varepsilon}_{out}$ is relaxed, the loss of strong ellipticity will appear when the following condition is satisfied

$$\det\left(A^{sym}(n)\right) = 0.$$ (1.26)

This condition will be met before or at the same time as the Equation (1.20) is satisfied.

During the deformation of solids, when the determinant of the symmetric part of the tangential modulus tensor becomes zero, the general bifurcation criterion is first met, and the strong ellipticity of the differential equation governing the material behavior is lost. The localization may occur prior to the point indicated by the classical discontinuous bifurcation criterion. For material exhibiting associated flow rule, the tangential modulus tensor is symmetric, and any type of bifurcation mode may appear at the general bifurcation point, which coincides with the beginning of strain softening. However, for materials with non-associated flow rule, the elasto-plastic constitutive equations are not symmetric. Because of the unsymmetry of the tangential modulus tensors, the general bifurcation criterion indicates that the bifurcation may even appear in the strain-hardening stage (see Bigoni and Hueckel [38]).

1.4 Objectives

The objectives of the present work are:

1. To formulate a rate-independent, or quasi-static strain softening plasticity model with associated flow rule and isotropic softening. This model is within the framework of classical continuum mechanics.

2. To develop a stress integration algorithm to solve the nonlinear system of equations that comes from the finite element formulation of the incremental boundary value problem for elasto-plasticity.

3. To develop a finite element program to implement the aforementioned model to numerically simulate the strain localization behavior.

4. To demonstrate the mesh-dependence of the simulation results arising from the classical continuum-based model in 1-D and 2-D scenarios.

5. To compare the gradient elasticity with gradient plasticity to justify the correct boundary conditions for the governing differential equations of these two gradient theories. The analytical solutions for two one-dimensional bars under tension are derived to examine the regularizing effects of different boundary conditions on the strain fields. The results provide the prerequisite for the development of the nonlocal plasticity model.

6. To develop a nonlocal plasticity model and a stress integration algorithm to regularize the mesh-dependence of the classical continuum model.

7. To implement the nonlocal plasticity model with C^0 finite elements to simulate the one-dimensional strain localization.

8. To propose future studies, both in theoretical and computational aspects, that would improve the current models, algorithms, and the simulation results.

CHAPTER 2

FINITE ELEMENT FORMULATION OF

CLASSICAL RATE-INDEPENDENT

STRAIN SOFTENING PLASTICITY MODEL

2.1 Introduction

The finite element method is a major numerical method for the computational simulation of strain localization. For the solution of any boundary-value problem (BVP) in continuum mechanics, its finite element formulation is closely related to the following aspects:

(i) The variational statement of the problem;

(ii) Constitutive modeling;

(iii) Finite element discretization and Galerkin's approximation of the variational equation; and

(iv) Computer implementation.

Physical phenomena indicate that the localized deformation occurring in the material failure stage is irrecoverable, plastic deformation. This process implies that the material's behavior exhibits strong nonlinearity. This material nonlinearity is caused by the constitutive equations that relate the stress field to the displacement field, which

includes elastic deformation and plastic deformation. Therefore, the numerical simulation of the strain localization can be carried out within the framework of classical elasto-plasticity. From a computational standpoint, the constitutive model and numerical algorithm play a central role in the finite element simulation of the elasto-plastic behavior. In this chapter, the constitutive equations for strain softening plasticity are developed, and the finite element equations for the simulation of strain localization are formulated. Three assumptions are made for the development of these equations: (i) the strain localization is only caused by the strain softening plasticity, not by the nonassociative flow law; (ii) deformation is infinitesimal; (iii) material behavior is rate-independent.

2.2 Constitutive Equations

2.2.1 Additive Separation of the Total Strain Tensor

Basically, the behavior of the elasto-plastic materials can be divided into two phases: elastic phase and elasto-plastic phase. During the elastic phase the material's behavior is elastic and no irrecoverable deformations remain in the material upon unloading in this phase. When the stress state meets some yield criterion, the material's response enters the elasto-plastic phase. During this phase, the material's behavior is no longer elastic and instead, some irrecoverable deformations are accumulated if the material's deformation continues to increase from the initial yielding state under further loading. The distinct characteristic of the plastic deformation is that it is irrecoverable after the material is unloaded to the zero-stress state. Starting from this point, it is reasonable to assume that the total strain tensor ε can be split into an elastic component ε^e and a plastic component ε^p [14, 39-42] (see Figure 2.1), that is

$$\boldsymbol{\varepsilon} = \boldsymbol{\varepsilon}^e + \boldsymbol{\varepsilon}^p .$$

(2.1)
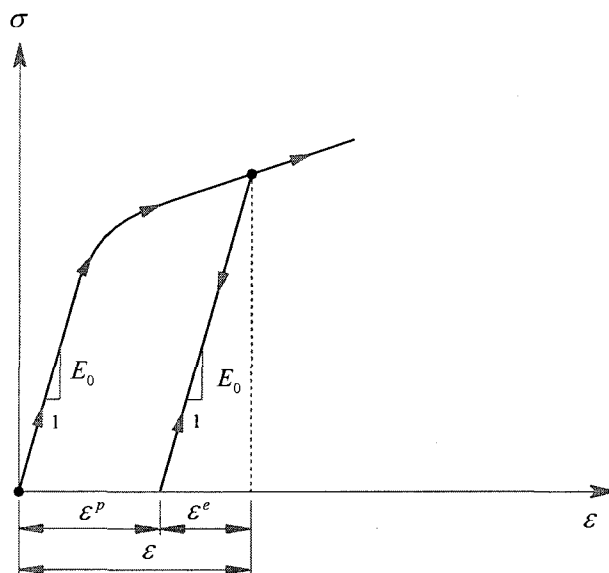
(a)
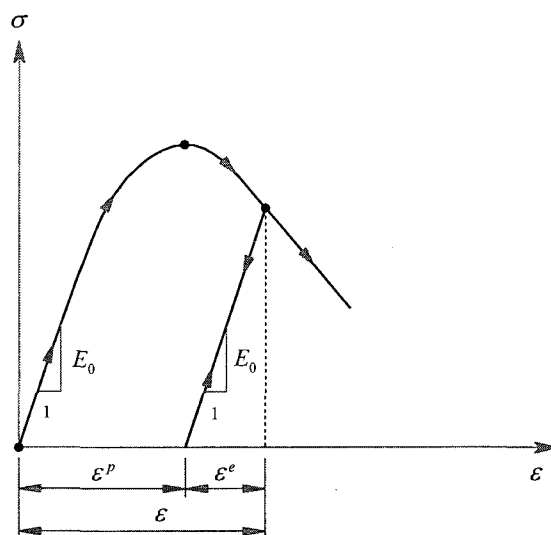
(b)

Figure 2.1 Additive separation of the total strain in the 1-D case: (a) in strain hardening; (b) in strain softening.

The incremental form of Equation (2.1) can be expressed as

$$d\boldsymbol{\varepsilon} = d\boldsymbol{\varepsilon}^e + d\boldsymbol{\varepsilon}^p . \tag{2.2}$$

The significance of Equation (2.2) is that only the elastic strain component is related to the stress by Hooke's law, while the plastic strain component is only related to the yield function and the flow law. Thus, the constitutive relations for the elastic deformation and plastic deformation can be formulated separately.

2.2.2 The Yield Function and Plastic Modulus

For perfect plasticity, isotropic strain hardening, and isotropic strain softening, the stress state at a material point in the elasto-plastic phase is governed by the following yield function:

$$f(\boldsymbol{\sigma},\eta) := \mathscr{F}(\boldsymbol{\sigma}) - \sigma_Y(\eta) = 0 , \tag{2.3}$$

where $\boldsymbol{\sigma}$ is a Cauchy stress tensor, η denotes an internal variable which is a nonnegative scalar, $\mathscr{F}(\boldsymbol{\sigma})$ represents an equivalent stress, and $\sigma_Y(\eta)$ is the yield stress or the flow stress. The evolution law of the yield stress $\sigma_Y(\eta)$ can be expressed as

$$\sigma_Y(\eta) = \sigma_{Y0} + \chi(\eta) , \tag{2.4}$$

where σ_{Y0} is the initial yield stress and $\chi(\eta)$ is the evolution function of the yield stress. The value of $\chi(\eta)$ defines the following plastic deformation process:

$$\left.\begin{array}{l} \chi(\eta) > 0 \ \& \ \dfrac{\partial \chi(\eta)}{\partial \eta} > 0 : \textit{Strain hardening plasticity} \\[2mm] \chi(\eta) \equiv 0 : \textit{Perfect plasticity} \\[2mm] \left(\chi(\eta) > 0 \text{ or } \chi(\eta) < 0\right) \ \& \ \dfrac{\partial \chi(\eta)}{\partial \eta} < 0 : \textit{Strain Softening plasticity} \end{array}\right\} \ \forall : \eta > 0 , \tag{2.5}$$

Figure 2.2 illustrates the evolution of $\chi(\eta)$ with η for linear strain hardening, perfect plasticity and linear strain softening.

Without loss of generality, the internal variable η can be taken to be equal to the equivalent plastic strain, ε_{eq}^{p}, that is

$$\eta = \varepsilon_{eq}^{p}, \tag{2.6}$$

in which ε_{eq}^{p} is defined by [40,41]

$$d\varepsilon_{eq}^{p} = \sqrt{\tfrac{2}{3} d\varepsilon_{ij}^{p} d\varepsilon_{ij}^{p}}, \tag{2.7}$$

$$\varepsilon_{eq}^{p} = \int d\varepsilon_{eq}^{p}. \tag{2.8}$$

Since the plastic deformation is irrecoverable, the total equivalent plastic strain is closely dependent on the strain history or loading path.

Differentiation of Equation (2.4) leads to the incremental yield stress–equivalent plastic strain relation

$$d\sigma_{Y} = E_{p} d\varepsilon_{eq}^{p}, \tag{2.9}$$

where E_{p} is a plastic modulus, which is defined as

$$E_{p} = \frac{d\sigma_{Y}(\eta)}{d\eta} = \frac{d\sigma_{Y}(\varepsilon_{eq}^{p})}{d\varepsilon_{eq}^{p}}. \tag{2.10}$$

Substituting Equation (2.5) into Equation (2.10) and noticing that σ_{Y0} is irrelative to η, E_{p} can also be expressed as

$$E_{p} = \frac{d\chi(\eta)}{d\eta} = \frac{d\chi(\varepsilon_{eq}^{p})}{d\varepsilon_{eq}^{p}}. \tag{2.11}$$
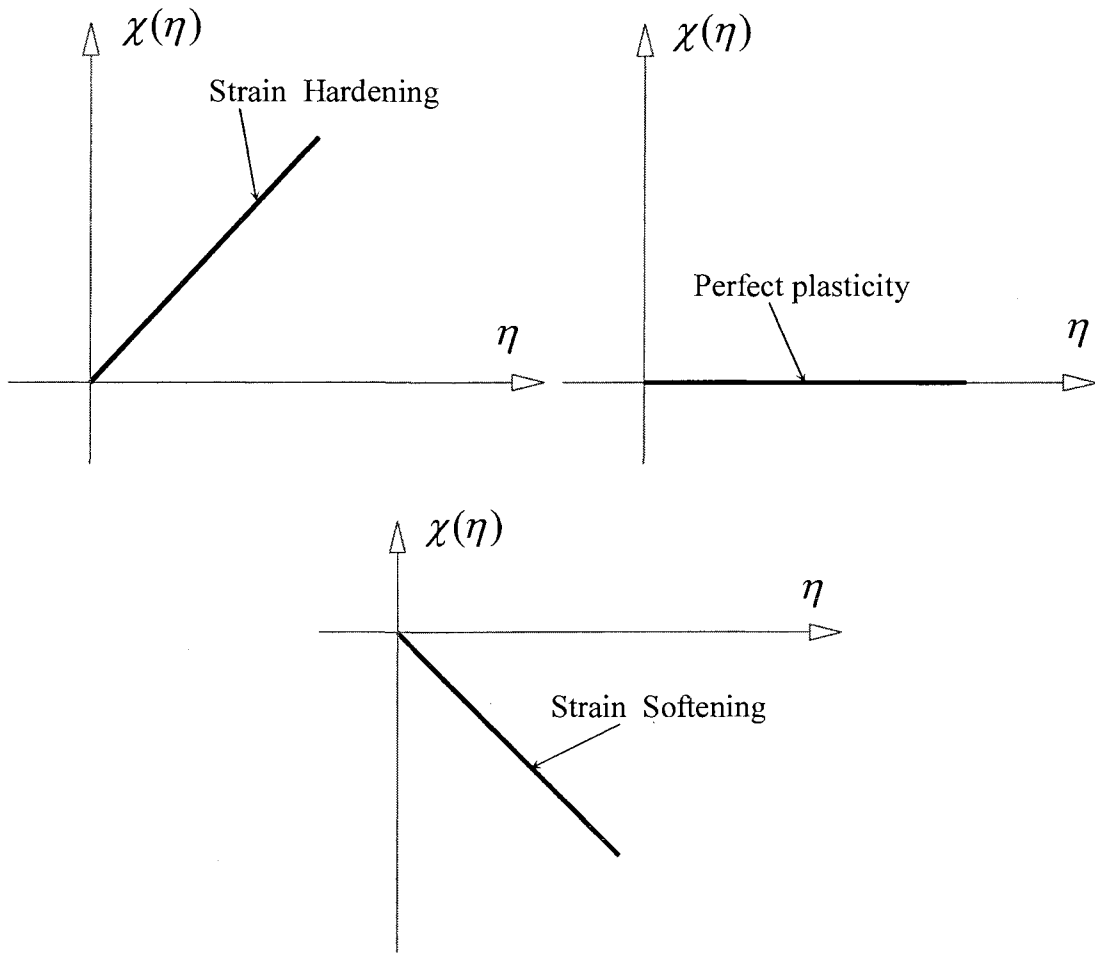
Figure 2.2 The evolution function of the yield stress

According to Equation (2.5), the sign of E_p is related the following plastic deformation

processes

$$
\left.
\begin{array}{l}
Strain\ hardening\ plasticity : E_p > 0 \\
Perfect\ plasticity : E_p = 0 \\
Strain\ Softening\ plasticity : E_p < 0 :
\end{array}
\right\} \quad \forall : \eta > 0, \tag{2.12}
$$

For the one-dimensional (1-D) case, we define the tangent modulus E_T as

$$
E_T = \frac{d\sigma_1}{d\varepsilon_1}. \tag{2.13}
$$

After initial yielding, we have

$$\sigma_1 = \sigma_Y, \quad d\varepsilon_1^p = d\varepsilon_{eq}^p. \tag{2.14}$$

Also, in the 1-D case, the additive separation relation of strain tensor, Equation (2.2), becomes

$$d\varepsilon_1 = d\varepsilon_1^e + d\varepsilon_1^p. \tag{2.15}$$

By substituting Equation (2.14) and (2.15) into Equation (2.13), we arrive at

$$E_T = \frac{d\sigma_Y}{d\varepsilon_1^e + d\varepsilon_{eq}^p} = \frac{1}{\dfrac{1}{\dfrac{d\sigma_Y}{d\varepsilon_1^e}} + \dfrac{1}{\dfrac{d\sigma_Y}{d\varepsilon_{eq}^p}}}. \tag{2.16}$$

By Hooke's law, it follows that

$$E_0 = \frac{d\sigma_Y}{d\varepsilon_1^e}, \tag{2.17}$$

where E_0 is Young's modulus. Using Equation (2.13) and (2.17), then Equation (2.16) reduces to

$$E_T = \frac{E_0 E_p}{E_0 + E_p}, \tag{2.18}$$

or, in another form

$$E_p = \frac{E_0 E_T}{E_0 - E_T}, \tag{2.19}$$

Figure 2.3 illustrates the plastic modulus for strain hardening, perfect plasticity and strain softening in the 1-D case.
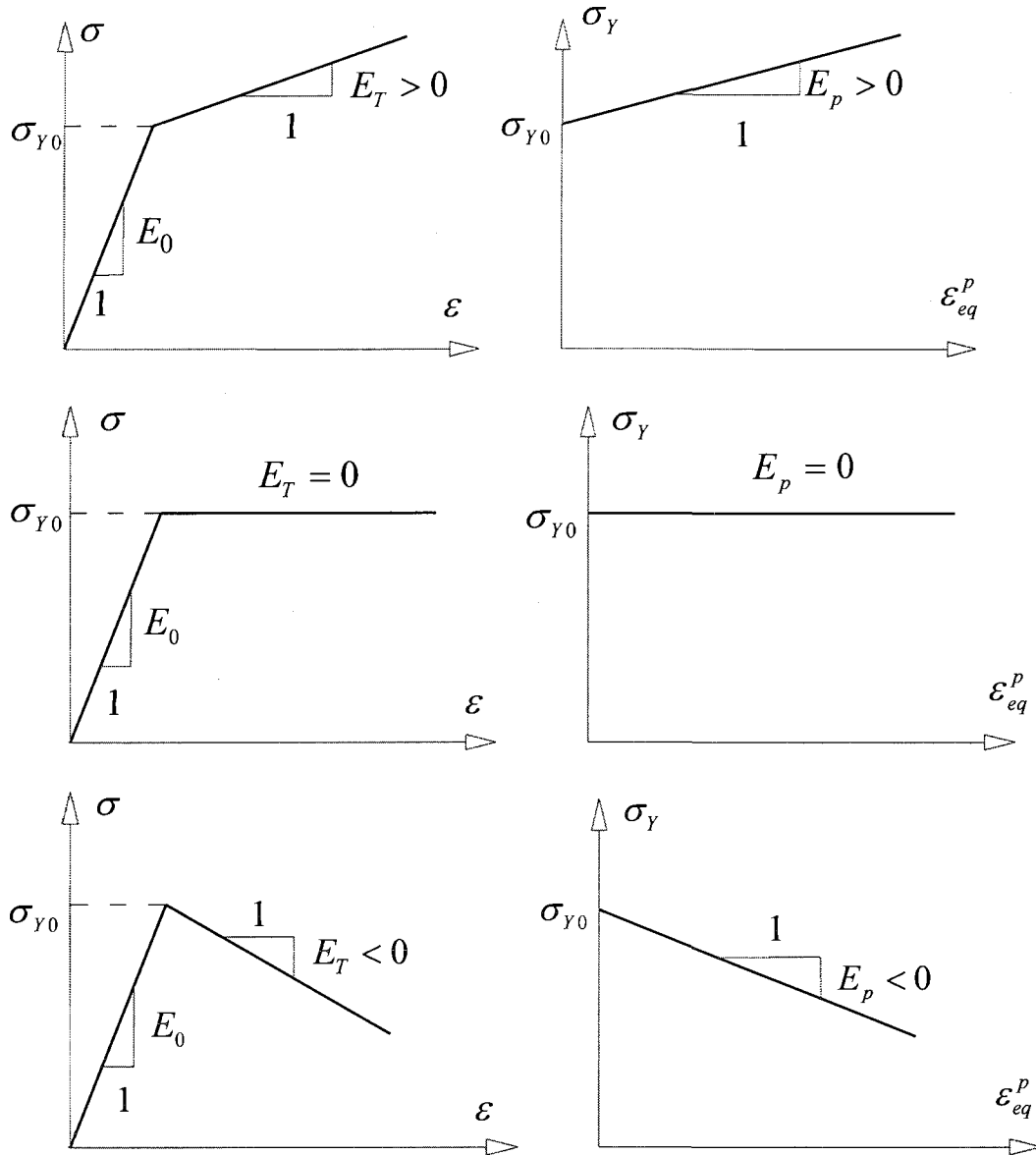
Figure 2.3 The plastic moduli for linear strain hardening, perfect plasticity, and linear strain softening.

According to Drucker's stability postulate [14, 39], we can find that the material behavior is stable only if $E_T > 0$ in the context of the 1-D case. If $E_T < 0$ the material behavior is unstable and strain localization occurs. Observing Equation (2.18) and (2.19), we obtain

$$E_T < 0 \Leftrightarrow E_p < 0, \qquad (2.20)$$

$$E_T > 0 \Leftrightarrow E_p > 0. \qquad (2.21)$$

From the above relations, we can conclude that a necessary condition for the occurrence of localized plastic deformation caused by strain softening is: $E_p < 0$.

2.2.3 Loading/Unloading Criteria in the Stress Space

Generally, the yield function $f(\boldsymbol{\sigma}, \eta) = 0$ represents a hypersurface in stress space. This hypersurface can be called a yield surface. Once the stress state meets the yield criterion, it implies that the stress state is located in the yield surface and plastic flow takes place. For the plastic flow to continue, the state of stress must remain on the yield surface. Thus, it follows that

$$f(\boldsymbol{\sigma}, \eta) = 0, \ df(\boldsymbol{\sigma}, \eta) = \frac{\partial f}{\partial \boldsymbol{\sigma}} : d\boldsymbol{\sigma} + \frac{\partial f}{\partial \eta} d\eta = 0, \ d\eta \geq 0. \qquad (2.22)$$

Equation (2.22) is the plastic loading criterion. If the stress state drops inside the yield surface, plastic deformation stops, and elastic unloading happens, which means

$$f(\boldsymbol{\sigma}, \eta) < 0, \ df(\boldsymbol{\sigma}, \eta) = \frac{\partial f}{\partial \boldsymbol{\sigma}} : d\boldsymbol{\sigma} + \frac{\partial f}{\partial \eta} d\eta < 0, \ d\eta = 0. \qquad (2.23)$$

Equation (2.23) is the unloading criterion. The loading/unloading criteria can be also expressed as the following Kuhn-Tucker complementarity condition [43]

$$d\eta \geq 0, \ f(\boldsymbol{\sigma}, \eta) \leq 0, \ d\eta f(\boldsymbol{\sigma}, \eta) = 0, \qquad (2.24)$$

and the consistency condition

$$d\eta df(\boldsymbol{\sigma}, \eta) = 0. \qquad (2.25)$$

In plastic loading, $d\eta > 0$, then the consistency condition reduces to

$$df(\boldsymbol{\sigma}, \eta) = 0. \qquad (2.26)$$

The consistency condition (2.26) enables us to relate the rate of the internal variable η to the current stress rate and provides the foundation for the development of the tangent elasto-plastic modulus.

2.2.4 Associative Flow Rule

In accordance with Drucker's stability postulate [14, 39], an assumption is made to relate the plastic strain increments to the plastic potential function $\mathscr{G}$. This assumption states that the plastic strain increments are proportional to the gradient of the plastic potential function $\mathscr{G}$ via the following equation

$$d\varepsilon_{ij}^{p} = d\lambda \frac{\partial \mathscr{G}}{\partial \sigma_{ij}}, \tag{2.27}$$

where $d\lambda$ is a non-negative scalar, called the plastic multiplier. If the plastic potential function and the yield function coincide, that is

$$\mathscr{G} = f, \tag{2.28}$$

then Equation (2.27) becomes

$$d\varepsilon_{ij}^{p} = d\lambda \frac{\partial f}{\partial \sigma_{ij}}. \tag{2.29}$$

The Equation (2.29) is called the associative flow rule because that the plastic flow is associated with the yield function (see Figure 1.15). Also, because the plastic strain increment vector $\dot{\varepsilon}^{p}$ is normal to the yield surface, relation (2.29) is also called normality condition or normal flow rule. Hill [39] provides the theoretical basis for the associative flow rule. Experimental observation indicates that the normality condition is an acceptable assumption for metals, but still questionable for rocks, concrete, and soils [40]. In the present strain softening plasticity model, only the associative flow rule is considered.

2.2.5 Tangent Elasto-Plastic Moduli

For both the elastic and elasto-plastic behavior, the stress tensor can always be related to the elastic component of the strain tensor through generalized Hooke's law

$$d\boldsymbol{\sigma} = \boldsymbol{D}^e : d\boldsymbol{\varepsilon}^e ,$$
(2.30)

where $\boldsymbol{D}$ is the elasticity tensor. Using relation (2.2), Equation (2.30) can be rewritten as

$$d\boldsymbol{\sigma} = \boldsymbol{D}^e : \left(d\boldsymbol{\varepsilon} - d\boldsymbol{\varepsilon}^p \right).$$
(2.31)

Substituting flow rule (2.29) into Equation (2.31) gives

$$d\boldsymbol{\sigma} = \boldsymbol{D}^e : \left(d\boldsymbol{\varepsilon} - d\lambda \frac{\partial f}{\partial \boldsymbol{\sigma}} \right).$$
(2.32)

For convenience, we rewrite the consistency condition (2.26) as

$$df(\boldsymbol{\sigma}, \eta) = \frac{\partial f}{\partial \boldsymbol{\sigma}} : d\boldsymbol{\sigma} + \frac{\partial f}{\partial \eta} d\eta = 0,$$
(2.33)

Introducing Equation (2.32) into Equation (2.33) and taking $\eta = \varepsilon_{eq}^p$ for strain hardening and strain softening plasticity, we get

$$df(\boldsymbol{\sigma}, \eta) = \frac{\partial f}{\partial \boldsymbol{\sigma}} : \boldsymbol{D}^e : \left(d\boldsymbol{\varepsilon} - d\lambda \frac{\partial f}{\partial \boldsymbol{\sigma}} \right) + \frac{\partial f}{\partial \varepsilon_{eq}^p} d\varepsilon_{eq}^p = 0 .$$
(2.34)

Using Equation (2.7), then Equation (2.34) becomes

$$df(\boldsymbol{\sigma}, \eta) = \frac{\partial f}{\partial \boldsymbol{\sigma}} : \boldsymbol{D}^e : \left(d\boldsymbol{\varepsilon} - d\lambda \frac{\partial f}{\partial \boldsymbol{\sigma}} \right) + \frac{\partial f}{\partial \varepsilon_{eq}^p} \sqrt{\tfrac{2}{3} d\varepsilon_{ij}^p d\varepsilon_{ij}^p} = 0 .$$
(2.35)

Substitution of flow rule (2.29) into Equation (2.35) leads to

$$df(\boldsymbol{\sigma}, \eta) = \frac{\partial f}{\partial \boldsymbol{\sigma}} : \boldsymbol{D}^e : \left(d\boldsymbol{\varepsilon} - d\lambda \frac{\partial f}{\partial \boldsymbol{\sigma}} \right) + d\lambda \frac{\partial f}{\partial \varepsilon_{eq}^p} \sqrt{\frac{2}{3} \frac{\partial f}{\partial \boldsymbol{\sigma}} : \frac{\partial f}{\partial \boldsymbol{\sigma}}} = 0 .$$
(2.36)

Rearranging the Equation (2.36), we have

$$dλ = \frac{\dfrac{\partial f}{\partial \boldsymbol{\sigma}} : \boldsymbol{D}^e : d\boldsymbol{\varepsilon}}{\dfrac{\partial f}{\partial \boldsymbol{\sigma}} : \boldsymbol{D}^e : \dfrac{\partial f}{\partial \boldsymbol{\sigma}} - \dfrac{\partial f}{\partial \varepsilon_{eq}^p} \sqrt{\dfrac{2}{3} \dfrac{\partial f}{\partial \boldsymbol{\sigma}} : \dfrac{\partial f}{\partial \boldsymbol{\sigma}}}} . \qquad (2.37)$$

Letting

$$A_p = -\frac{\partial f}{\partial \varepsilon_{eq}^p} \sqrt{\frac{2}{3} \frac{\partial f}{\partial \boldsymbol{\sigma}} : \frac{\partial f}{\partial \boldsymbol{\sigma}}} . \qquad (2.37)$$

Equation (2.36) can be written as

$$dλ = \frac{\dfrac{\partial f}{\partial \boldsymbol{\sigma}} : \boldsymbol{D}^e : d\boldsymbol{\varepsilon}}{\dfrac{\partial f}{\partial \boldsymbol{\sigma}} : \boldsymbol{D}^e : \dfrac{\partial f}{\partial \boldsymbol{\sigma}} + A_p} . \qquad (2.38)$$

For the von Mises yield function, it can be proved that (see Appendix A for a proof)

$$A_p = E_p , \qquad (2.39)$$

$$dλ = d\varepsilon_{eq}^p . \qquad (2.40)$$

But for other yield functions, Equation (2.39) and (2.40) may not hold.

Substituting Equation (2.38) into (2.32) yields

$$d\boldsymbol{\sigma} = \boldsymbol{D}^{ep} : d\boldsymbol{\varepsilon} , \qquad (2.41)$$

$$\boldsymbol{D}^{ep} = \boldsymbol{D}^e - \frac{\left(\boldsymbol{D}^e : \dfrac{\partial f}{\partial \boldsymbol{\sigma}} \right) \otimes \left(\boldsymbol{D}^e : \dfrac{\partial f}{\partial \boldsymbol{\sigma}} \right)}{\dfrac{\partial f}{\partial \boldsymbol{\sigma}} : \boldsymbol{D}^e : \dfrac{\partial f}{\partial \boldsymbol{\sigma}} + A_p} , \qquad (2.42)$$

where $\boldsymbol{D}^{ep}$ is the tangent elasto-plastic modulus tensor. In the 1-D case, Equation (2.42) reduces to Equation (2.18).

2.3 Governing Differential Equations for the Incremental Elasto-Plastic Boundary Problem

It is well established that, in the plastic region, the strain depends not only on the final state of stress, but also on the loading history. Therefore the incremental stress-strain relations have to be used to characterize the constitutive behaviors of materials during plastic deformation. The following statement of a boundary value problems is under two assumptions: the increments are infinitesimal and the governing equations may be linearized [44]. According to the flow theory of plasticity, the incremental form of a boundary value problems of elasto-plasticity is posed as follows.

Suppose that at a given instant of time t, a domain Ω is in a state of static equilibrium and the state of stress $\boldsymbol{\sigma}$ and its loading history is known throughout the domain. The external force increment $d\hat{\boldsymbol{F}}$ is prescribed on $\partial_g\Omega$, and the displacement $d\hat{\boldsymbol{u}}$ is prescribed on $\partial_u\Omega$, where ∂_g and ∂_u denote the boundary associated with the given force and displacement (Figure 2.4). The boundary value problem of incremental elasto-plasticity is to find the incremental displacement field $d\boldsymbol{u}$ that satisfies, in Ω,

the equation of equilibrium

$$\operatorname{div} d\boldsymbol{\sigma} + d\boldsymbol{b} = 0, \tag{2.43}$$

the Strain–displacement relation

$$d\boldsymbol{\varepsilon} = \frac{1}{2}\left(\nabla d\boldsymbol{u} + \left(\nabla d\boldsymbol{u}\right)^T\right), \tag{2.44}$$

the constitutive relation

$$d\boldsymbol{\sigma} = \boldsymbol{D}_T : d\boldsymbol{\varepsilon}, \tag{2.45}$$

$$\boldsymbol{D}_T = \begin{cases} \boldsymbol{D}^e & \text{if } d\varepsilon_{eq}^p = 0, \\ \boldsymbol{D}^{ep} & \text{if } d\varepsilon_{eq}^p > 0, \end{cases} \tag{2.46}$$

and *the boundary condition*

$$d\boldsymbol{\sigma} \cdot \boldsymbol{n} = d\hat{\boldsymbol{F}} \quad \text{on} \quad \partial_g \Omega \; , \qquad (2.47)$$

$$d\boldsymbol{u} = d\hat{\boldsymbol{u}} \quad \text{on} \quad \partial_u \Omega \; , \qquad (2.48)$$

where $\partial_g \Omega \bigcup \partial_u \Omega = \partial \Omega , \partial_g \Omega \bigcap \partial_u \Omega = \emptyset$. If the domain is in the elastic state, we have

$d\boldsymbol{\varepsilon}^p = 0$. If it experiences plastic loading, we have $d\varepsilon_{eq}^p > 0$.
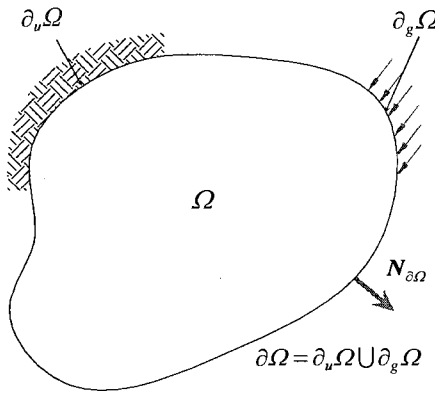
Figure 2.4 The elasto-plastic domain

2.4 Variational Formulation

To solve the governing differential equation numerically using the finite element approximation, variational formulae of the governing equations have to be constructed [45-48].

If $d\boldsymbol{u}$ is the solution of field Equations (2.43)-(2.48) and $\delta d\boldsymbol{u}$ is the variation of $d\boldsymbol{u}$, the weak form of the equilibrium Equation (2.43) can be expressed as

$$\int_\Omega \delta d\boldsymbol{u} \cdot (\text{div } d\boldsymbol{\sigma} + d\boldsymbol{b}) = 0 . \qquad (2.49)$$

Integrating Equation (36) by parts and applying the divergence theorem to it leads to

$$\int_{\Omega} \delta\mathbf{\varepsilon} : d\mathbf{\sigma}\, dV = \int_{\Omega} d\mathbf{b} \cdot \delta d\mathbf{u}\, dV + \int_{\partial\Omega_g} d\hat{\mathbf{F}} \cdot \delta d\mathbf{u}\, dS . \qquad (2.50)$$

Substitution of Equations (2.44)–(2.47) into the above equation results in

$$\int_{\Omega} \delta\mathbf{\varepsilon} : \mathbf{D}_T : d\mathbf{\varepsilon}\, dV = \int_{\Omega} d\mathbf{b} \cdot \delta d\mathbf{u}\, dV + \int_{\partial\Omega_g} d\hat{\mathbf{F}} \cdot \delta d\mathbf{u}\, dS . \qquad (2.51)$$

The variational statement of the incremental boundary value problem of elasto-plasticity is: find $d\mathbf{u}$ such that

$$\left.\begin{array}{l} \displaystyle\int_{\Omega} \delta\mathbf{\varepsilon} : \mathbf{D}_T : d\mathbf{\varepsilon}\, dV = \int_{\Omega} d\mathbf{b} \cdot \delta d\mathbf{u}\, dV + \int_{\partial\Omega_g} d\hat{\mathbf{F}} \cdot \delta d\mathbf{u}\, dS \\[12pt] d\mathbf{u} = d\hat{\mathbf{u}} \qquad \text{on } \partial_u\Omega \end{array}\right\}. \qquad (2.52)$$

The implication of Equation (2.52) is that the solution $d\mathbf{u}$ satisfies the equilibrium Equation (2.43) in the sense of weighted averages [46].

2.5 Finite Element Formulation (Galerkin's Approximation)

From this point on we will use $\lfloor\ \rfloor$ to denote a row matrix and $\{\ \}$ to denote a column matrix, and $[\ ]$ to denote the other matrices that are neither row matrices nor column matrices.

Let us discretize the domain Ω into element domains $\Omega^e, 1 \le e \le n_{el}$, where n_{el} is the total number of elements. The displacement field $d\mathbf{u}$ within Ω^e can be approximated by

$$\{d\mathbf{u}\} = [\mathbf{N}]\{d\mathbf{u}_h^e\}, \qquad (2.53)$$

where $[\mathbf{N}]$ is the matrix of shape functions for displacements and $\{d\mathbf{u}_h^e\}$ represents the displacements at element nodal points. The strain-displacement relations can be expressed in the matrix form

$$\{\mathbf{\varepsilon}\} = [\mathbf{B}]\{d\mathbf{u}_h^e\}, \qquad (2.54)$$

where $[B]$ is the strain-displacement matrix, which is defined as:

$$[B] = [B_1, B_2, \cdots, B_{n_{en}}],$$ (2.55)

in which n_{en} denotes the number of element nodes. If $\{\varepsilon\}$ is defined as:

$$\{\varepsilon\} = \lfloor \varepsilon_1 \quad \varepsilon_2 \quad \varepsilon_{12} \rfloor^T, \text{ for } n_{sd} = 2,$$ (2.56)

$$\{\varepsilon\} = \lfloor \varepsilon_1 \quad \varepsilon_2 \quad \varepsilon_3 \quad 2\varepsilon_{23} \quad 2\varepsilon_{13} \quad 2\varepsilon_{12} \rfloor^T, \text{ for } n_{sd} = 3,$$ (2.57)

where n_{sd} is the space dimension of the problem in hand, then the sub-matrix $[B_j]$

($j = 1, \cdots, n_{en}$) is defined by

$$[B_j] = \begin{bmatrix} N_{j,1} & 0 \\ 0 & N_{j,2} \\ N_{j,2} & N_{j,1} \end{bmatrix}, \quad (j = 1, \cdots, n_{en}), \quad \text{for } n_{sd} = 2,$$ (2.58)

$$[B_j] = \begin{bmatrix} N_{j,1} & 0 & 0 \\ 0 & N_{j,2} & 0 \\ 0 & 0 & N_{j,3} \\ 0 & N_{j,3} & N_{j,2} \\ N_{j,3} & 0 & N_{j,1} \\ N_{j,2} & N_{j,1} & 0 \end{bmatrix}, \quad (j = 1, \cdots, n_{en}) \quad \text{for } n_{sd} = 3.$$ (2.59)

Substituting Equation (2.53) and (2.54) into Equation (2.52) yields

$$\{\delta d u_h^e\}^T \int_{\Omega^e} [B]^T [D_T][B]\{d u_h^e\} dV = \{\delta d u_h^e\}^T \int_{\Omega^e} [N]^T \{db\} dV + \{\delta d u_h^e\}^T \int_{\partial\Omega_g^e} [N]^T \{d\hat{F}\} dS,$$ (2.60)

Because Equation (2.60) holds for arbitrary $\{\delta d u_h^e\}$, it follows that

$$\int_{\Omega^e} [B]^T [D_T][B]\{d u_h^e\} dV = \int_{\Omega^e} [N]^T \{db\} dV + \int_{\partial\Omega_g^e} [N]^T \{d\hat{F}\} dS.$$ (2.61)

Equation (2.61) can be rewritten in the more compact form

$$[K^e]\{du_h^e\} = \{d\hat{F}_h^e\}.$$ (2.62)

in which

$$[K^e] = \int_{\Omega^e} [B]^T [D_T][B] dV ,$$ (2.63)

$$\{d\hat{F}_h^e\} = \int_{\Omega^e} [N]^T \{db\} dV + \int_{\partial\Omega_g^e} [N]^T \{d\hat{F}\} dS .$$ (2.64)

The matrix $[K^e]$ is the tangent element stiffness matrix. With $[K^e]$ in hand, standard finite element stiffness assemblage procedures can be used to obtain the global stiffness matrix, and the standard equation solver can be employed to solve the linearized algebraic system of equations to obtain the solution of incremental displacement field du. With du solved, $d\varepsilon$ and $d\sigma$ can be found using Equation (2.54) and (2.45).

2.6 Solution Method for Nonlinear System of Equations

Matrix Equation (2.62) comes from the weak forms of the incremental governing Equations (2.43)–(2.48). However, a material' response to plastic deformation is generally nonlinear. The source of this nonlinearity arises from the constitutive equations that relate the stress field to the displacement field. Therefore Equation (2.62) is actually the linearized form of a nonlinear system of operator equations [49]:

$$\mathcal{F}_h^e X_h^e = 0,$$ (2.65)

where $\mathcal{F}_h^e$ is a nonlinear mapping defined as $\mathcal{F}_h^e : R^{n_e} \mapsto R^{n_e}$ and X_h^e is the solution of Equation (2.65) and defined as

$$X_h^e = \{u_h^e\}.$$ (2.66)

Strictly, the solutions of the displacement field, u must satisfy the following equilibrium equation (for convenience we take the body force $b = 0$):

$$\operatorname{div} \boldsymbol{\sigma} + \boldsymbol{b} = 0, \quad \text{in } \Omega, \tag{2.67}$$

and

$$\boldsymbol{\sigma} = \boldsymbol{D}^e : \left(\boldsymbol{\varepsilon} - \boldsymbol{\varepsilon}^p \right). \tag{2.68}$$

Let $\delta\boldsymbol{u}$ be the variation of $\boldsymbol{u}$. The weak form of Equation (2.67) can be written as:

$$\int_{\Omega} \delta\boldsymbol{u} \cdot \left(\operatorname{div} \boldsymbol{\sigma} + \boldsymbol{b} \right) = 0. \tag{2.69}$$

Following the same approach as the derivation of the weak form of the incremental equilibrium equation, we obtain

$$\int_{\Omega} \delta\boldsymbol{\varepsilon} : \boldsymbol{\sigma}\, dV = \int_{\Omega} \boldsymbol{b} \cdot \delta\boldsymbol{u}\, dV + \int_{\partial\Omega_g} d\hat{\boldsymbol{F}} \cdot \delta\boldsymbol{u}\, dS, \tag{2.70}$$

where the boundary conditions $\boldsymbol{\sigma} \cdot \boldsymbol{n} = \hat{\boldsymbol{F}}$ on $\partial_g\Omega$ and $\boldsymbol{u} = \hat{\boldsymbol{u}}$ on $\partial_u\Omega$ are applied. Upon discretizing the domain, Ω, and applying the interpolation relations

$$\{\boldsymbol{u}\} = [\boldsymbol{N}]\{\boldsymbol{u}_h^e\}, \tag{2.71}$$

and

$$\{\boldsymbol{\varepsilon}\} = [\boldsymbol{B}]\{\boldsymbol{u}_h^e\}, \tag{2.72}$$

to Equation (2.70), we obtain:

$$\{\delta\boldsymbol{u}_h^e\}^T \int_{\Omega^e} [\boldsymbol{B}]^T [\boldsymbol{\sigma}]\, dV = \{\delta\boldsymbol{u}_h^e\}^T \int_{\Omega^e} [\boldsymbol{N}]^T \{\boldsymbol{b}\}\, dV + \{\delta\boldsymbol{u}_h^e\}^T \int_{\partial\Omega_g^e} [\boldsymbol{N}]^T \{\hat{\boldsymbol{F}}\}\, dS. \tag{2.73}$$

Considering the arbitrariness of $\{\delta\boldsymbol{u}_h^e\}$, we have

$$\int_{\Omega^e} [\boldsymbol{B}]^T [\boldsymbol{\sigma}]\, dV = \int_{\Omega^e} [\boldsymbol{N}]^T \{\boldsymbol{b}\}\, dV + \int_{\partial\Omega_g^e} [\boldsymbol{N}]^T \{\hat{\boldsymbol{F}}\}\, dS, \tag{2.74}$$

or

$$\int_{\Omega^e} [\boldsymbol{B}]^T [\boldsymbol{\sigma}]\, dV - \{\boldsymbol{F}\} = 0, \tag{2.74a}$$

where

$$\{F\} = \int_{\Omega^e} [N]^T \{b\} dV + \int_{\partial\Omega_g^e} [N]^T \{\hat{F}\} dS , \qquad (2.75)$$

$$[\sigma] = [D^e](\{\varepsilon\} - \{\varepsilon^p\}). \qquad (2.76)$$

Due to the nonlinearity of the relationship between $[\sigma]$ and $\{x_h^e\}$, we define

$$[\sigma] = [\mathscr{A}(x_h^e)], \qquad (2.77)$$

and

$$[\mathscr{A}(x_h^e)] = [D^e]([B]\{u_h^e\} - [\mathscr{P}([\sigma],\{u_h^e\})]), \qquad (2.78)$$

where $[\mathscr{P}([\sigma],\{u_h^e\})]$ denotes the total plastic strains matrix, which is the function of total stresses and total displacements. Substitution of Equation (2.77) into Equation (2.74a) gives

$$\int_{\Omega^e} [B]^T [\mathscr{A}(x_h^e)] dV - \{F\} = 0. \qquad (2.79)$$

Comparing Equation (2.79) with Equation (2.65), the nonlinear mapping $\mathfrak{I}_h^e : R^{n_e} \mapsto R^{n_e}$ is defined by

$$\mathfrak{I}_h^e x_h^e = \int_{\Omega^e} [B]^T [\mathscr{A}(x_h^e)] dV - \{F\} = 0. \qquad (2.80)$$

Because of the nonlinearity of the problem, the solution x_h^e resulting from the incremental-iterative solution procedure will not generally satisfy Equation (2.80). For the kth iteration the solution will generally result in

$$\left(\mathfrak{I}_h^e x_h^e\right)_k = \int_{\Omega^e} [B]^T [\mathscr{A}(x_h^e)]_k dV - \{F\}_k \neq 0. \qquad (2.81)$$

During the $(k+1)^{th}$ iteration, we require

$$\left(\mathcal{I}_h^e x_h^e\right)_{k+1} = \int_{\Omega^e}[\boldsymbol{B}]^T[\mathscr{A}(x_h^e)]_{k+1}dV - \{\boldsymbol{F}\}_{k+1} = 0. \qquad (2.82)$$

If $[\boldsymbol{\sigma}]$, $\{\hat{\boldsymbol{F}}\}$ and $\{\boldsymbol{b}\}$ are linearly additive, i.e.

$$[\boldsymbol{\sigma}]_{k+1} = [\boldsymbol{\sigma}]_k + [\Delta\boldsymbol{\sigma}], \qquad (2.83)$$

$$\{\hat{\boldsymbol{F}}\}_{k+1} = \{\hat{\boldsymbol{F}}\}_k + \{\Delta\hat{\boldsymbol{F}}\}, \qquad (2.84)$$

$$\{\boldsymbol{b}\}_{k+1} = \{\boldsymbol{b}\}_k + \{\Delta\boldsymbol{b}\}, \qquad (2.85)$$

Equation (2.82) can be rewritten as

$$\left(\mathcal{I}_h^e x_h^e\right)_{k+1} = \int_{\Omega^e}[\boldsymbol{B}]^T([\boldsymbol{\sigma}]_k + [\Delta\boldsymbol{\sigma}])dV - \left(\int_{\Omega^e}[\boldsymbol{N}]^T\{\boldsymbol{b}\}_k + \{\Delta\boldsymbol{b}\}dV + \int_{\partial\Omega_g^e}[\boldsymbol{N}]^T(\{\hat{\boldsymbol{F}}\}_k + \{\Delta\hat{\boldsymbol{F}}\})dS\right) = 0,$$

$$(2.86)$$

Letting

$$\{\hat{\boldsymbol{F}}_h^e\}_k = \int_{\Omega^e}[\boldsymbol{N}]^T\{\boldsymbol{b}\}_k dV + \int_{\partial\Omega_g^e}[\boldsymbol{N}]^T\{\hat{\boldsymbol{F}}\}_k dS, \qquad (2.87)$$

$$\{\Delta\boldsymbol{F}_h^e\}_k^{unb} = \{\hat{\boldsymbol{F}}_h^e\}_k - \int_{\Omega^e}[\boldsymbol{B}]^T[\boldsymbol{\sigma}]_k dV, \qquad (2.88)$$

$$\{\Delta\hat{\boldsymbol{F}}_h^e\} = \int_{\Omega^e}[\boldsymbol{N}]^T\{\Delta\boldsymbol{b}\}dV + \int_{\partial\Omega_g^e}[\boldsymbol{N}]^T\{\Delta\hat{\boldsymbol{F}}\}dS, \qquad (2.89)$$

and rearranging the terms of Equation (2.86), we have

$$\int_{\Omega^e}[\boldsymbol{B}]^T[\Delta\boldsymbol{\sigma}]dV = \{\Delta\hat{\boldsymbol{F}}_h^e\} + \{\Delta\hat{\boldsymbol{F}}_h^e\}_k^{unb}. \qquad (2.90)$$

If $[\Delta\boldsymbol{\sigma}]$ is taken as *the linear term* of the Taylor expansion of $[\boldsymbol{\sigma}]$ at the time-discretized k^{th} iteration and the incremental constitutive relationships (2.45) are adopted, Equation (2.90) can be linearized as

$$[\boldsymbol{K}^e]\{\Delta \boldsymbol{u}_h^e\} = \{\Delta \hat{\boldsymbol{F}}_h^e\} + \{\Delta \hat{\boldsymbol{F}}_h^e\}_k^{unb} ,$$
(2.91)

where

$$[\boldsymbol{K}^e] = \int_{\Omega^e} [\boldsymbol{B}]^T [\boldsymbol{D}_T][\boldsymbol{B}] dV .$$
(2.92)

Solutions of total displacements at the $(k+1)^{\text{th}}$ iteration can be obtained by

$$\{\boldsymbol{u}_h^e\}_{k+1} = \{\boldsymbol{u}_h^e\}_k + \{\Delta \boldsymbol{u}_h^e\}.$$
(2.93)

Mathematically, the linearization process from Equation (2.74) to (2.93) is called method of Newton's form. In each load increment, this linearization method is applied iteratively to find the displacement $\{\boldsymbol{u}_h^e\}$ until $\{\Delta \hat{\boldsymbol{F}}_h^e\}_k^{unb}$ becomes sufficiently small.

2.7 Stress Integration Algorithm

According to the flow theory of plasticity, the stress–plastic strain relation is expressed as an incremental form through flow rule (2.29) after the stress state satisfies the yield criterion and the plastic deformation takes place. The incremental nature of the flow rule results in the stress-strain relation (2.41) to be incremental for the plastic deformation. To find the total stresses and plastic strains, we have to integrate the flow rules or the incremental stress–strain equations along the stress path. From the computational standpoint, for each iteration, e.g., k^{th} iteration, we need to find the unbalanced nodal forces $\{\Delta \boldsymbol{F}_h^e\}_k^{unb}$. According to Equation (2.88), we need to know the total stresses $[\boldsymbol{\sigma}]_k$ at first to obtain $\{\Delta \boldsymbol{F}_h^e\}_k^{unb}$.

2.7.1 Intersection Point on the Yield Surface for Initial Yielding

To formulate the numerical algorithm, we have to distinguish between the iteration and the load increment. Unless otherwise specified, k denotes the iteration number, and n denotes the load increment number, regardless of whether they are superscripts or subscripts.

In the computation of the elasto-plastic response, if the stress state meets the yield criterion the first time, it is impossible that the geometrical point representing the stress state in the stress space is just located on the yield surface, and instead, it is generally located outside the yield surface (see Figure 2.5), that is

$$f(\boldsymbol{\sigma}_{k+1}) = f(\boldsymbol{\sigma}_k + \Delta\boldsymbol{\sigma}^e) > 0 . \tag{2.94}$$

To find the intersection of the stress path with the yield surface, we require

$$f(\boldsymbol{\sigma}_k + \alpha\Delta\boldsymbol{\sigma}^e) = 0 , \tag{2.95}$$

where $\boldsymbol{\sigma}_k$, representing the stress at k^{th} iteration, are such that

$$f(\boldsymbol{\sigma}_k) = 0 , \tag{2.96}$$

and α is a factor. An initial value of α can be estimated by [40, 50, 51]

$$\alpha_1 = \frac{-f(\boldsymbol{\sigma}_k)}{f(\boldsymbol{\sigma}_{k+1}) - f(\boldsymbol{\sigma}_k)}, \tag{2.97}$$

then $\boldsymbol{\sigma}_{k+1}$ is updated as

$$\boldsymbol{\sigma}_{k+1}^{(1)} = \boldsymbol{\sigma}_k + \alpha_1\Delta\boldsymbol{\sigma}^e . \tag{2.98}$$

Expanding the yield function into a truncated Taylor series at point B (corresponding to $\boldsymbol{\sigma}_{k+1}^{(1)}$) with respect to α leads to

$$f\left(\boldsymbol{\sigma}_k^{(1)} + \delta\alpha\Delta\boldsymbol{\sigma}_e\right) = f\left(\boldsymbol{\sigma}_k^{(1)}\right) + \frac{\partial f}{\partial\boldsymbol{\sigma}} : \Delta\boldsymbol{\sigma}^e\delta\alpha = 0, \qquad (2.99)$$

$$\delta\alpha = \frac{-f\left(\boldsymbol{\sigma}_k^{(1)}\right)}{\dfrac{\partial f}{\partial\boldsymbol{\sigma}} : \Delta\boldsymbol{\sigma}^e}, \qquad (2.100)$$

and the $\boldsymbol{\sigma}_{k+1}$ is updated the second time as

$$\boldsymbol{\sigma}_{k+1}^{(2)} = \boldsymbol{\sigma}_k^{(1)} + \delta\alpha\Delta\boldsymbol{\sigma}^e, \qquad (2.101)$$

$$\alpha_2 = \alpha_1 + \delta\alpha, \qquad (2.101\text{a})$$
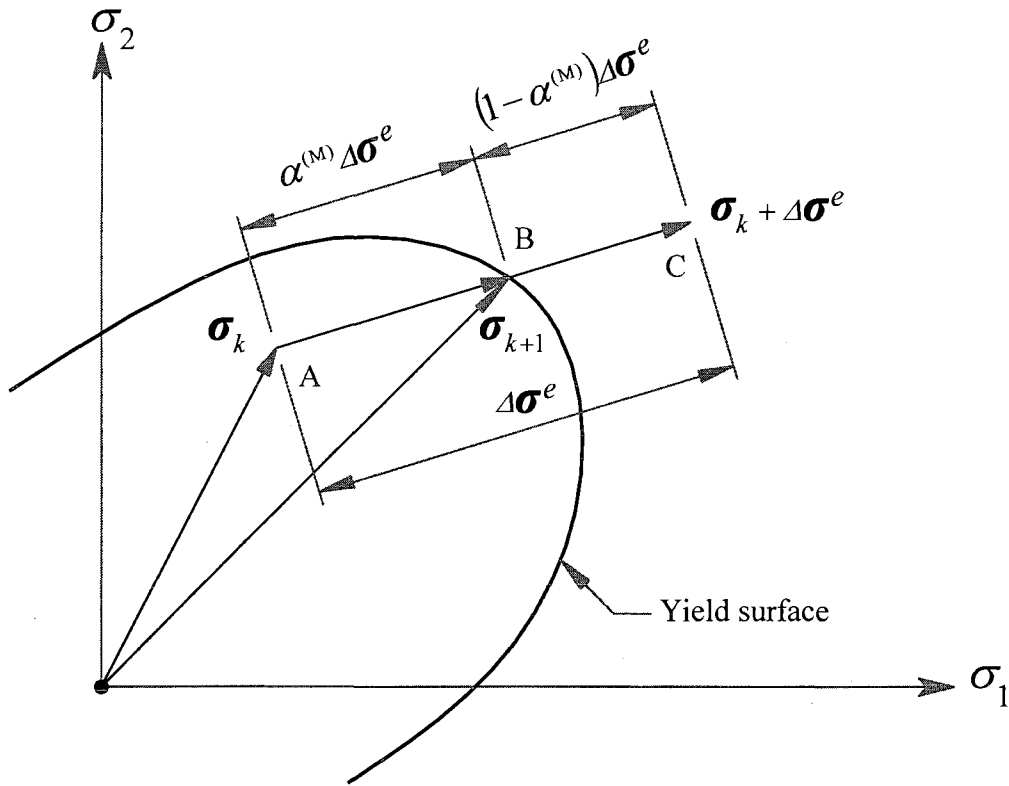
Figure 2.5 Determination of the intersection point on the yield surface.

At this point, $\boldsymbol{\sigma}_{k+1}^{(2)}$ is very close to the yield surface, but not right on the surface, i.e.

$$f\left(\boldsymbol{\sigma}_{k+1}^{(2)}\right) \neq 0 .$$

However, continuing to apply the Taylor expansion to correct the $\boldsymbol{\sigma}_{k+1}^{(2)}$ will lead to the oscillation of $\boldsymbol{\sigma}_{k+1}^{(2)}$ and result in the non-convergent results. More accurate $\boldsymbol{\sigma}_{k+1}$ can be obtained using the bisection method (see Conte and Boor [52]). This algorithm is summarized in Table 2.1.

After the stress state at the intersection point has been computed, the remaining portion of the stress increment, which is equal to $\left(\boldsymbol{\sigma}_k + \Delta\boldsymbol{\sigma}^e - \boldsymbol{\sigma}_{k+1}^{(2)}\right)$, can be treated by an elasto-plastic rate integration method.

Table 2.1 Algorithm for computing the intersection point on the yield surface

1. LET $\sigma_{k+1}^{(I)} = \sigma_{k+1}^{(2)}$, $\alpha^{(I)} = \alpha_2$

2. IF $f\left(\sigma_{k+1}^{(I)}\right) > 0$ THEN :

3. $\alpha^{(B)} = \alpha^{(I)}$

4. $\sigma_{k+1}^{(I)} = \sigma_{k+1}^{(I)} - \delta\alpha\Delta\sigma_e$; $\alpha^{(I)} = \alpha^{(I)} - \delta\alpha$

5.   IF $f\left(\sigma_{k+1}^{(I)}\right) > 0$ THEN : GO TO 4

        ELSE : $\alpha^{(A)} = \alpha^{(I)}$

        END IF

6. ELSE IF $f\left(\sigma_{k+1}^{(I)}\right) < 0$ THEN :

7. $\alpha^{(A)} = \alpha^{(I)}$

8. $\sigma_{k+1}^{(I)} = \sigma_{k+1}^{(I)} + \delta\alpha\Delta\sigma_e$; $\alpha^{(I)} = \alpha^{(I)} + \delta\alpha$

9.   IF $f\left(\sigma_{k+1}^{(I)}\right) < 0$ THEN : GO TO 8

        ELSE : $\alpha^{(B)} = \alpha^{(I)}$

        END IF

        END IF

10. $\alpha^{(M)} = 0.5\left(\alpha^{(A)} + \alpha^{(B)}\right)$, $\sigma_{k+1}^{(M)} = \sigma_{k+1}^{(2)} + \alpha^{(M)}\Delta\sigma_e$

11. IF $\left|f\left(\sigma_{k+1}^{(M)}\right)\right| < $ TOL THEN : $\sigma_{k+1}^{(2)} = \sigma_{k+1}^{(M)}$ GOTO 12

     ELSE

        IF $f\left(\sigma_{k+1}^{(M)}\right) < 0$ THEN : $\alpha^{(A)} = \alpha^{(M)}$ GOTO 10

        ELSE IF $f\left(\sigma_{k+1}^{(M)}\right) > 0$ THEN $\alpha^{(B)} = \alpha^{(M)}$ GOTO 10

        END IF

     END IF

12. OUTPUT $\sigma_{k+1} = \sigma_{k+1}^{(2)}$ as the final stress state on the yield surface.

2.7.2 Subsequent Yielding

After reaching the yield surface, if the deformation continues to increase, the plastic loading condition will constrain the stress state to be maintained in the current (neutral loading) or subsequent yield surface (strain hardening or softening). For the

finite-sized load or strain increments, the incremental constitutive equation (2.41) becomes

$$\Delta\boldsymbol{\sigma} = \boldsymbol{D}^{ep} : \Delta\boldsymbol{\varepsilon} = \boldsymbol{D}^{e} : \left(\Delta\boldsymbol{\varepsilon} - \Delta\boldsymbol{\varepsilon}^{p}\right),$$ (2.102)

or

$$\Delta\boldsymbol{\sigma} = \Delta\boldsymbol{\sigma}^{e} - \Delta\lambda\boldsymbol{D}^{e} : \frac{\partial f}{\partial\boldsymbol{\sigma}}.$$ (2.103)

Applying the forward-Euler integration scheme [50, 51], for the $(n+1)^{th}$ iteration the above equations can be written as

$$\Delta\boldsymbol{\sigma}_{(n+1)} = \boldsymbol{D}^{ep}_{(n)} : \Delta\boldsymbol{\varepsilon}_{(n+1)},$$ (2.104)

$$\Delta\boldsymbol{\sigma}_{(n+1)} = \Delta\boldsymbol{\sigma}^{e}_{(n+1)} - \Delta\lambda_{(n+1)}\boldsymbol{D}^{e} : \frac{\partial f}{\partial\boldsymbol{\sigma}}\bigg|_{(n)}.$$ (2.105)

The plastic multiplier at the $(n+1)^{th}$ load step $\Delta\lambda_{(n+1)}$ can be found using the forward-difference form of the differential Equation (2.37)

$$\Delta\lambda_{(n+1)} = \frac{\dfrac{\partial f}{\partial\boldsymbol{\sigma}}\bigg|_{(n)} : \boldsymbol{D}^{e} : \Delta\boldsymbol{\varepsilon}_{(n+1)}}{\dfrac{\partial f}{\partial\boldsymbol{\sigma}}\bigg|_{(n)} : \boldsymbol{D}^{e} : \dfrac{\partial f}{\partial\boldsymbol{\sigma}}\bigg|_{(n)} + A_{p}}.$$ (2.106)

The total stress $\boldsymbol{\sigma}_{(n+1)}$ at the $(n+1)^{th}$ step can be obtained by

$$\boldsymbol{\sigma}_{(n+1)} = \boldsymbol{\sigma}_{(n)} + \Delta\boldsymbol{\sigma}_{(n+1)}.$$ (2.107)

Notice that in Equation (2.105) and (2.106), $\partial f/\partial\boldsymbol{\sigma}$ represents the gradient of the yield function at a stress point on the yield surface and is a function of the total Cauchy stresses. Because its value at the nth load step is used in the solution of $\Delta\lambda_{(n+1)}$ and $\Delta\boldsymbol{\sigma}_{(n+1)}$, this integration scheme is also called explicit integration scheme.

Generally in the elasto-plastic response the changes of the stress components during the loading process are not proportional and also the loading is monotonic due to the plastic flow. Thus $(\partial f / \partial \boldsymbol{\sigma})$ will continuously vary with increasing strain. Employing $(\partial f / \partial \boldsymbol{\sigma})$ at the nth load step to compute $\Delta \lambda_{(n+1)}$ and $\Delta \boldsymbol{\sigma}_{(n+1)}$ will introduce numerical integration errors, especially when the load increment size is inappropriately large or/and the stress point is near a region of large curvature of the yield. To reduce this integration error, the strain increment $\Delta \boldsymbol{\varepsilon}_{(n+1)}$ is divided into m sub-increments (see Figure 2.6), i.e.

$$\Delta \boldsymbol{\varepsilon}_{(n+1,i)} = \frac{\Delta \boldsymbol{\varepsilon}_{(n+1,i)}}{m}, \quad i = 1, 2 \ldots, m . \tag{2.108}$$

For each sub-increment, the above forward-Euler integration scheme is used to find the $\Delta \lambda_{(n+1,i)}$, $\Delta \boldsymbol{\sigma}_{(n+1,i)}$ and thus

$$\Delta \boldsymbol{\sigma}_{(n+1)} = \sum_{i=1}^{m} \Delta \boldsymbol{\sigma}_{(n+1,i)} . \tag{2.109}$$

This method is described by Owen and Hinton [40] and Crisfield [50].

After obtaining $\boldsymbol{\sigma}_{(n+1)}$, we need to check if the yield criterion is satisfied. Generally it is outside the yield surface. If so, we use the following radial return method to correct the $\boldsymbol{\sigma}_{(n+1)}$ in order to return the stress state to the yield surface.
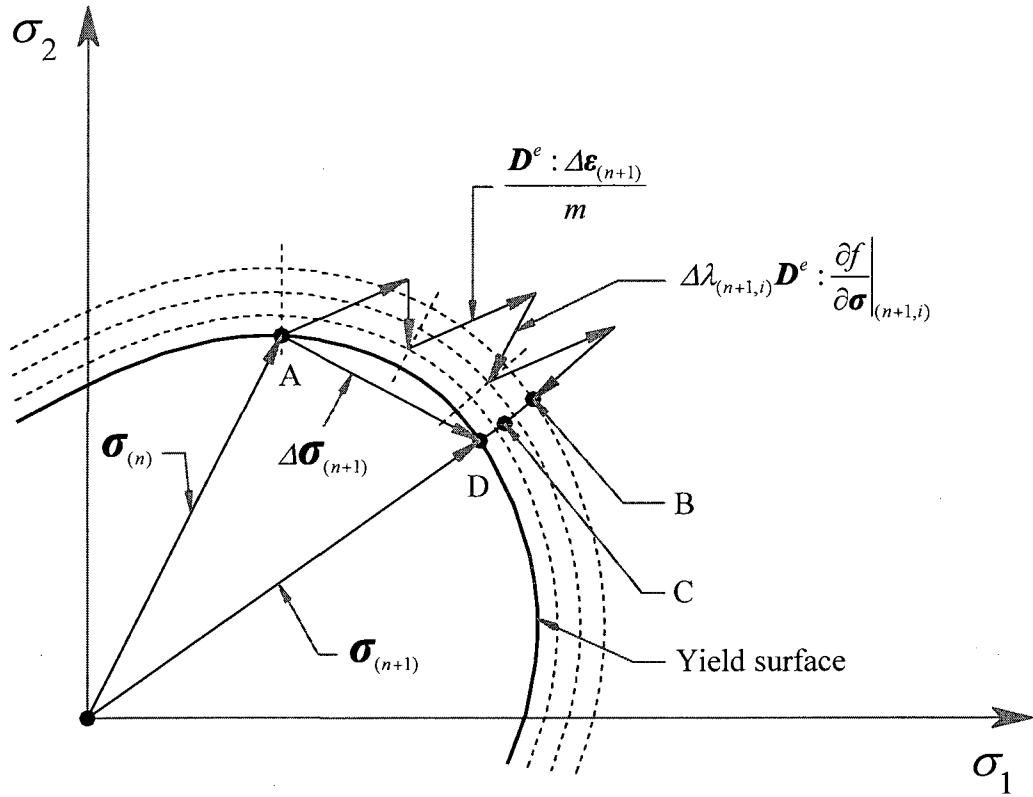
Figure 2.6 Geometrical illustration of the forward-Euler stress integration.

In this approach, the total strains are kept unchanged while additional plastic strains are introduced to reduce the stresses to the yield surface. The truncated Taylor expansion of the yield function at the $(n+1)^{th}$ step is given by

$$f\left(\boldsymbol{\sigma}_{(n+1)}^{(1)}\right) = f\left(\boldsymbol{\sigma}_{(n+1)}\right) + \left.\frac{\partial f}{\partial \boldsymbol{\sigma}}\right|_{(n+1)} : \Delta\boldsymbol{\sigma}^p + \left.\frac{\partial f}{\partial \varepsilon_{eq}^p}\right|_{(n+1)} : \Delta\varepsilon_{eq}^p = 0, \tag{2.110}$$

where $\boldsymbol{\sigma}_{(n+1)}^{(1)}$ denotes the updated stress after $\boldsymbol{\sigma}_{(n+1)}$ is corrected; $\Delta\boldsymbol{\sigma}^p$ represents stress decrement (corresponding to the distance from point B to C in Figure 2.6) due to the additional plastic strain through the relation

$$\Delta\boldsymbol{\sigma}^{p} = \boldsymbol{D}^{e}\Delta\boldsymbol{\varepsilon}^{p} = \Delta\lambda_{(n+1)}^{(1)}\boldsymbol{D}^{e} : \left.\frac{\partial f}{\partial\boldsymbol{\sigma}}\right|_{(n+1)}. \tag{2.111}$$

Substituting Equation (2.37) and (2.111) into (2.110) and rearranging the terms results in

$$\Delta\lambda_{(n+1)}^{(1)} = \frac{f\left(\boldsymbol{\sigma}_{(n+1)}\right)}{\left.\frac{\partial f}{\partial\boldsymbol{\sigma}}\right|_{(n+1)} : \boldsymbol{D}^{e} : \left.\frac{\partial f}{\partial\boldsymbol{\sigma}}\right|_{(n+1)} + A_{p}}. \tag{2.112}$$

The updated total stress is

$$\boldsymbol{\sigma}_{(n+1)}^{(1)} = \boldsymbol{\sigma}_{(n+1)} - \Delta\lambda_{(n+1)}^{(1)}\boldsymbol{D}^{e} : \left.\frac{\partial f}{\partial\boldsymbol{\sigma}}\right|_{(n+1)}, \tag{2.113}$$

which corresponds to the point C in Figure 2.6.

If $f\left(\boldsymbol{\sigma}_{(n+1)}^{(1)}\right) > 0$, $\boldsymbol{\sigma}_{(n+1)}^{(1)}$ can be scaled back to the yield surface by

$$\boldsymbol{\sigma}_{(n+1)}^{(2)} = \boldsymbol{\sigma}_{(n+1)}^{(1)}\left(\frac{\sigma_{Y}(\eta)}{\mathscr{F}(\boldsymbol{\sigma})}\right), \tag{2.114}$$

which corresponds to the point D in Figure 2.6. Using Equation (2.113) will generally introduce elastic components into $\boldsymbol{\sigma}_{(n+1)}^{(1)}$, which is different from the radial return method. Considering that the stress state $\boldsymbol{\sigma}_{(n+1)}^{(1)}$ is very close to the yield surface at this point, application of Equation (2.113) at the last step of stress updating algorithm will generally lead to good convergence properties of the numerical procedure.

Table 2.2 summarizes the whole stress integration algorithm.

Table 2.2 Stress integration algorithm

0.	Given $\boldsymbol{\varepsilon}_{(n)}$, $\boldsymbol{\sigma}_{(n)}$ for n^{th} load step and $\Delta\boldsymbol{\varepsilon}_{(n+1)}$ for $(n+1)^{th}$ load step
1.	Compute elastic trial stresses

$$\Delta\boldsymbol{\sigma}^e_{(n+1)} = \boldsymbol{D}^e : \Delta\boldsymbol{\varepsilon}_{(n+1)}$$

$$\boldsymbol{\sigma}^{trial}_{(n+1)} = \boldsymbol{\sigma}_{(n)} + \Delta\boldsymbol{\sigma}^e_{(n+1)}$$

2. IF $f\left(\boldsymbol{\sigma}^{trial}_{(n+1)}\right) > 0$ THEN :

    IF (Initial yielding is true) THEN :

        Find intersecton point : solve $\alpha^{(M)}$.

    ELSE : $\alpha^{(M)} = 0$

    END IF

$$\Delta\boldsymbol{\sigma}_{(n+1,0)} = \alpha^{(M)}\boldsymbol{D}^e : \Delta\boldsymbol{\varepsilon}_{(n+1)}$$

$$\Delta\boldsymbol{\varepsilon}_{(n+1)} = \left(1 - \alpha^{(M)}\right)\Delta\boldsymbol{\varepsilon}_{(n+1)}$$

    GO TO 3

    ELSE IF $f\left(\boldsymbol{\sigma}^{trial}_{(n+1)}\right) < 0$ THEN :

    GO TO 7

    END IF

3. $\Delta\boldsymbol{\varepsilon}_{(n+1,i)} = \dfrac{\Delta\boldsymbol{\varepsilon}_{(n+1)}}{m}, \quad i = 1, 2\ldots, m.$

    Find : $\Delta\lambda_{(n+1,i)}$ and $\Delta\boldsymbol{\sigma}_{(n+1,i)}$ uisng Eq.(2.104) - (2.106)

$$\Delta\boldsymbol{\sigma}_{(n+1)} = \sum_{i=0}^{m}\Delta\boldsymbol{\sigma}_{(n+1,i)}; \quad \boldsymbol{\sigma}_{(n+1)} = \boldsymbol{\sigma}_{(n)} + \Delta\boldsymbol{\sigma}_{(n+1)}$$

4. IF $f\left(\boldsymbol{\sigma}_{(n+1)}\right) > 0$ THEN :

    Compute $\Delta\lambda^{(1)}_{(n+1)}$ and $\boldsymbol{\sigma}^{(1)}_{(n+1)}$ according to Eq.(2.112) - (2.113).

    ENDIF

5. IF $f\left(\boldsymbol{\sigma}^{(1)}_{(n+1)}\right) > 0$ THEN :

    Compute $\boldsymbol{\sigma}^{(2)}_{(n+1)}$ according to Eq.(2.114).

    ENDIF

6. Output : $\boldsymbol{\sigma}_{(n+1)} = \boldsymbol{\sigma}^{(2)}_{(n+1)}$

7. EXIT stress intergration.

2.8 Summary

For elasto-plastic deformation, the total strain tensor can be additively separated into an elastic component and a plastic component. The elastic component is related to the stress tensor by Hooke's law, while the plastic component is connected with yield functions and flow laws. Combining the associative flow rule, consistency condition and Hooke's law, the elasto-plastic tangent modulus tensor and incremental constitutive equation is derived. A necessary condition for the occurrence of localized plastic deformation is $E_p < 0$. Based on the incremntal constitutive equation, the variational equation of the incremental elasto-plastic boundary value problem is developed and the finite element approximation of this variational equation is formulated through Galerkin's method. The solution method for the resulting nonlinear system of equations is described, which is of Newton's form. The forward-Euler integration procedure is developed to integrate the incremental constitutive equation and the stress integration algorithm is shown.

CHAPTER 3

COMPUTER IMPLEMENTATION AND

NUMERICAL EXAMPLES

3.1 Introduction

To provide the solution to the elasto-plastic boundary-value problem with the strain softening plasticity model and implement its finite element approximation, two computer programs, one named EP1D for one-dimensional problems and the other named EPLAS for two-dimensional problems, are developed. In this chapter, the program structures and the main functions of EP1D and EPLAS are outlined. To verify the strain softening plasticity model developed in Chapter 2, 1-D and 2-D numerical examples are given to demonstrate the formation of strain localization arising from the strain softening. Also a detailed analysis of the mesh-dependency is given based on a 1-D model problem.

3.2 Outline of the Computer Programs

The computer programs EP1D and EPLAS are based on the framework provided by Owen and Hinton [40], Hughes [47], and Zienkiewicz [53]. An outline of the program structure is shown in Figure 3.1.

EP1D is mainly designed for the 1-D plastic strain softening analysis. The element type in EP1D is a two-noded constant stress element with linear shape functions (Figure 3.2). Gaussian direct elimination is used in the equation solver.

EPLAS is mainly designed for the 2-D plastic strain softening analysis. The element types in EPLAS include the 4-node isoparametric quadrilateral element, the 8-node Serendipity quadrilateral element, and the 9-node Lagrangian quadrilateral element (see Figure 3.3). Only the 8-node Serendipity quadrilateral element is employed in the numerical simulation of the strain localization. The frontal method is used in the assembly of the element stiffness matrices and the solution of unknown displacements.

Both EP1D and EPLAS employ the Newton-Raphson method for the solution of the nonlinear equilibrium equations (see Bathe [48] and Zienkiewicz [53]) and use the same stress integration algorithm, that is, the forward-Euler integration algorithm. EPLAS incorporates the following yield criteria with isotropic strain hardening and strain softening: von Mises criterion, Tresca criterion, Mohr-Coulomb criterion, and Drucker-Prager criterion [14, 40, 41]. To focus on the simulation of the strain localization phenomenon, only the von Mises criterion with isotropic strain softening is used in the present research.

The main objectives of EP1D and EPLAS are to numerically simulate the strain localization caused by strain softening plasticity. However these two programs can also be used for the finite element analysis of linear elastic problems, perfect plasticity, and strain hardening plasticity problems.

The programs are coded using the standard FORTRAN 90 programming language and dynamic allocation of memory is used in the storage of the global stiffness matrix.
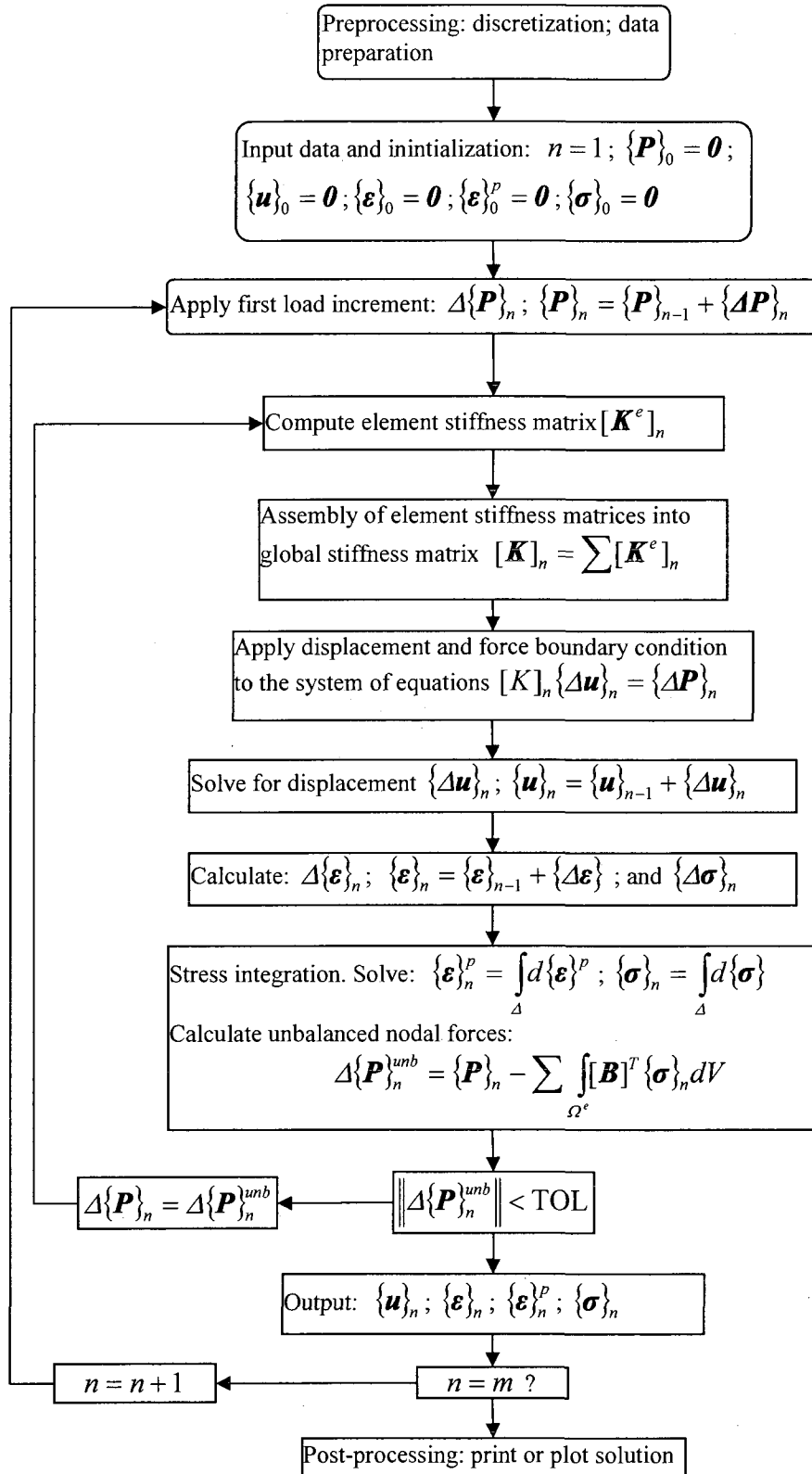
Figure 3.1 The outline of the finite element program for elasto-plastic problems.
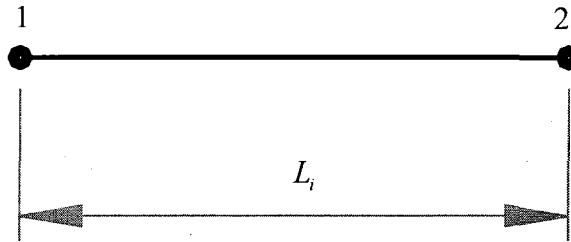
Figure 3.2 The 1-D constant stress elements

4-node element   8-node element   9-node element
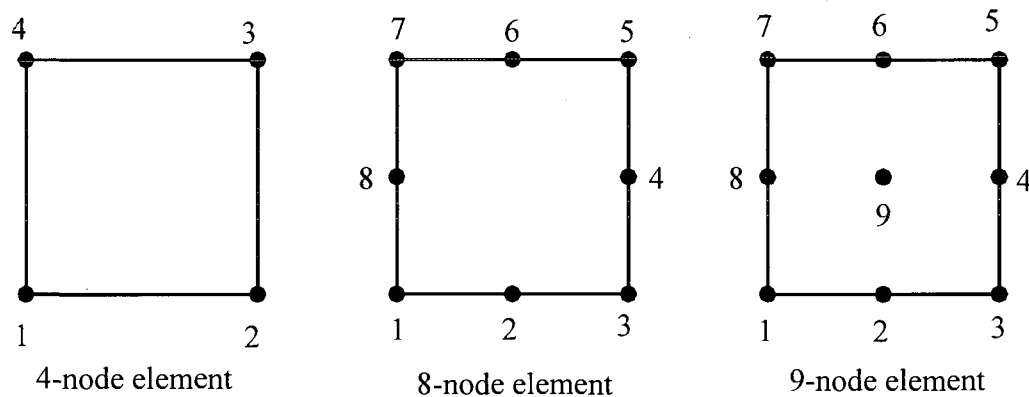
Figure 3.3 The 2-D isoparametric elements.

3.3 Analysis of a 1-D Model Problem

3.3.1 Statement of the Problem

Let us consider a 1-D bar under uniaxial tension (Figure 3.4). The bar has a length of L and a unit cross-sectional area $A = 1$. Its one end is fixed and the other end is applied with a tensile force $\hat{F}$ or a displacement $\hat{u}$. It is assumed that the material behaviors elastically until its stress reaches the yield stress σ_{Y0}, and then linear strain softening behavior follows, with $E_p < 0$. The corresponding tangential modulus for the elasto-plastic curve is $E_s^{ep} < 0$. A weak zone of length L_s is also assumed to be in the

middle part of the bar such that the material in this zone enters the strain softening stage

earlier than the other part of the bar.

As soon as the material in the weak zone enters the strain softening stage, the

remaining part of the bar will experience elastic unloading, and the elongation of the bar

will continue to increase with force decreased. In the following section, we use the finite

element method to analyze this process.

3.3.2 Analysis of the Tangential Stiffness Matrix

The bar is discretized into 3 1-D elements: two elastic elements with equal length

L_0 and one softening element with length L_s. The geometry and the boundary conditions

are shown in Figure 3.5. For elements 1 and 3 (elastic elements), the incremental

equilibrium equations are

$$\left(\frac{E_0 A_0}{l_0} \right) \begin{bmatrix} 1 & -1 \\ -1 & 1 \end{bmatrix} \begin{Bmatrix} du_1^{(1)} \\ du_2^{(1)} \end{Bmatrix} = \begin{Bmatrix} dF_1^{(1)} \\ dF_2^{(1)} \end{Bmatrix}, \tag{3.1}$$

$$\left(\frac{E_0 A_0}{l_0} \right) \begin{bmatrix} 1 & -1 \\ -1 & 1 \end{bmatrix} \begin{Bmatrix} du_3^{(3)} \\ du_4^{(3)} \end{Bmatrix} = \begin{Bmatrix} dF_3^{(3)} \\ dF_4^{(3)} \end{Bmatrix}. \tag{3.2}$$

For element 2 (softening element), the incremental equilibrium equation is

$$\left(\frac{E_s A_s}{l_s} \right) \begin{bmatrix} 1 & -1 \\ -1 & 1 \end{bmatrix} \begin{Bmatrix} du_2^{(2)} \\ du_3^{(2)} \end{Bmatrix} = \begin{Bmatrix} dF_2^{(2)} \\ dF_3^{(2)} \end{Bmatrix}, \tag{3.3}$$

where the superscripts inside the round brackets, ($\bullet$), denote the element numbers and

the subscripts represent the node numbers. The equilibrium condition at each nodal point

leads to

$$\left. \begin{aligned} dF_1 &= dF_1^{(1)} \\ dF_2 &= dF_2^{(1)} + dF_2^{(2)} = 0 \\ dF_3 &= dF_3^{(2)} + dF_3^{(3)} = 0 \\ dF_4 &= dF_4^{(3)} \end{aligned} \right\} .$$

(3.4)
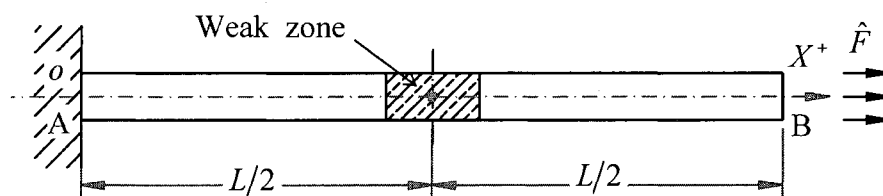
Figure 3.4 A 1-D model problem.
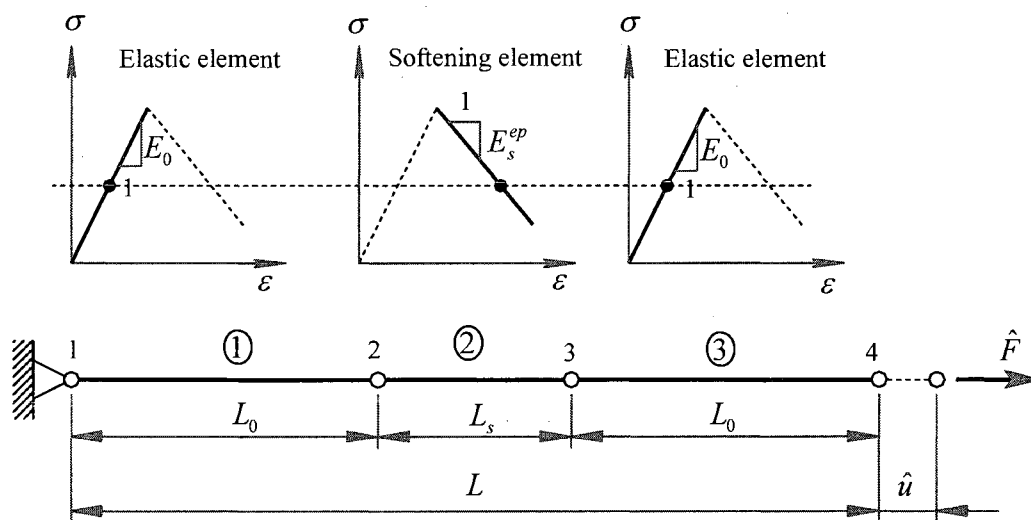
Figure 3.5 The finite element discretization of the 1-D model problem.

Substitution of Equations (3.1)-(3.3) into Equation (3.4) results in

$$
\begin{bmatrix}
\dfrac{E_0 A_0}{l_0} & \dfrac{E_0 A_0}{l_0} & 0 & 0 \\[2mm]
-\dfrac{E_0 A_0}{l_0} & \dfrac{E_0 A_0}{l_0}+\dfrac{E_s A_s}{l_s} & -\dfrac{E_s A_s}{l_s} & 0 \\[2mm]
0 & -\dfrac{E_s A_s}{l_s} & \dfrac{E_0 A_0}{l_0}+\dfrac{E_s A_s}{l_s} & -\dfrac{E_0 A_0}{l_0} \\[2mm]
0 & 0 & -\dfrac{E_0 A_0}{l_0} & \dfrac{E_0 A_0}{l_0}
\end{bmatrix}
\begin{Bmatrix} du_1 \\ du_2 \\ du_3 \\ du_4 \end{Bmatrix}
=
\begin{Bmatrix} dF_1 \\ 0 \\ 0 \\ dF_4 \end{Bmatrix}.
\tag{3.5}
$$

Introducing the displacement boundary condition

$$
du_1 = 0
\tag{3.6}
$$

into Equation (3.5), we have

$$
\begin{bmatrix}
\dfrac{E_0 A_0}{l_0}+\dfrac{E_s A_s}{l_s} & -\dfrac{E_s A_s}{l_s} & 0 \\[2mm]
-\dfrac{E_s A_s}{l_s} & \dfrac{E_0 A_0}{l_0}+\dfrac{E_s A_s}{l_s} & -\dfrac{E_0 A_0}{l_0} \\[2mm]
0 & -\dfrac{E_0 A_0}{l_0} & \dfrac{E_0 A_0}{l_0}
\end{bmatrix}
\begin{Bmatrix} du_2 \\ du_3 \\ du_4 \end{Bmatrix}
=
\begin{Bmatrix} 0 \\ 0 \\ dF_4 \end{Bmatrix}.
\tag{3.7}
$$

Equation (3.7) is a linear system of equations with regard to du_2, du_3, du_4, and dF_4. If

dF_4 is known (under force-controlled loading), one finds that

$$
du_2 = \left(\frac{E_0 A_0}{L_0}\right)^{-1} dF_4,
\tag{3.8}
$$

$$
du_3 = \left(\frac{E_s A_s}{L_s}\right)^{-1} dF_4 + du_2 = \left(\left(\frac{E_0 A_0}{L_0}\right)^{-1}+\left(\frac{E_s^{ep} A_s}{L_s}\right)^{-1}\right) dF_4,
\tag{3.9}
$$

$$
du_4 = \left(\frac{E_0 A_0}{L_0}\right)^{-1} dF_4 + du_3 = \left(2\left(\frac{E_0 A_0}{L_0}\right)^{-1}+\left(\frac{E_s^{ep} A_s}{L_s}\right)^{-1}\right) dF_4.
\tag{3.10}
$$

With equilibrium equation (3.1), the reaction dF_1 at node 1 can be found to be

$$dF_1 = \frac{E_0 A_0}{L_0}\left(du_1 - du_2\right) = -\frac{E_0 A_0}{L_0} du_2. \tag{3.11}$$

The condition for the strain softening behavior of this model problem is

$$E_s^{ep} < 0, \ dF_4 < 0 \ \text{and} \ du_4 > 0. \tag{3.12}$$

From Equation (3.10) and the above condition, we arrive at

$$2\left(\frac{E_0 A_0}{L_0}\right)^{-1} + \left(\frac{E_s^{ep} A_s}{L_s}\right)^{-1} < 0, \tag{3.13}$$

$$\frac{2L_0}{E_0 A_0} + \frac{L_s}{E_s^{ep} A_s} < 0. \tag{3.14}$$

Because $E_s^{ep} < 0$, for convenience, we rewrite the inequality (3.14) as

$$\frac{2L_0}{E_0 A_0} + \frac{L_s}{-\left|E_s^{ep}\right| A_s} < 0, \tag{3.15}$$

$$\frac{L_s}{2L_0} > \frac{\left|E_s^{ep}\right| A_s}{E_0 A_0}. \tag{3.16}$$

Letting

$$L_e = 2L_0, \ r_s = L_s/L_e, \ r_E = \left|E_s^{ep}\right|/E_0 \tag{3.17}$$

and noticing that $A_0 = A_s$, inequality (3.16) can take the final form

$$r_s > r_E, \tag{3.18}$$

where r_s is the length ratio of the softening element with respect to the elastic element and r_E is the tangential modulus ratio. In Equation (3.17), L_e represents the sum of total lengths of the elastic elements. In sum, the condition for the strain softening behavior to occur is

$$\boxed{E_s^{ep} < 0, \ dF_4 < 0, \ du_4 > 0, \ \text{and} \ r_s > r_E.} \tag{3.19}$$

If the loading is controlled by the forced displacement u_4 at nodal point 4, the same results and conclusion as above can be obtained. In the finite element simulation of the strain localization, only the displacement-controlled loading scheme is used.

If the condition (3.18) is violated, the load-displacement path will follow a "snap-back" path ($r_s < r_E$) or the steepest-drop path ($r_s = r_E$) (see Figure 3.6).

From Equation (3.10), the slope of the load-displacement can be expressed as

$$\frac{dF_4}{du_4} = \frac{E_0 A_0}{L_0}(du_4 - du_3) = \left(2\left(\frac{E_s A_s}{L_s}\right)^{-1} + \left(\frac{E_0 A_0}{L_0}\right)^{-1}\right)^{-1}. \tag{3.20}$$

It can be seen that the slope is related to the length of the softening element even if the condition for the strain softening is satisfied. This fact is reflected in the numerical simulation results, which is called mesh-dependency. The fundamental reason for the mesh-dependency is that the governing equations for the strain softening behavior are ill-posed.

3.3.3 Numerical Results

The length of the bar is taken to be $L = 100\,\text{mm}$. The element located in the center of the bar is treated as a weak element, whose yield stress is 10% off compared to the yield stress of the normal elements. Material parameters are listed in Table 3.1. The finite element discretization is shown in Figure 3.7, and the discretization data for all meshes are listed in Table 3.2. Eight different meshes with 1, 3, 5, 7, 9, 11, 21, and 101 elements, respectively, are used to analyze the problem. The load is displacement-controlled and the forced displacement u is applied at the end B until the final displacement of $u = 0.019\,\text{mm}$ is achieved.
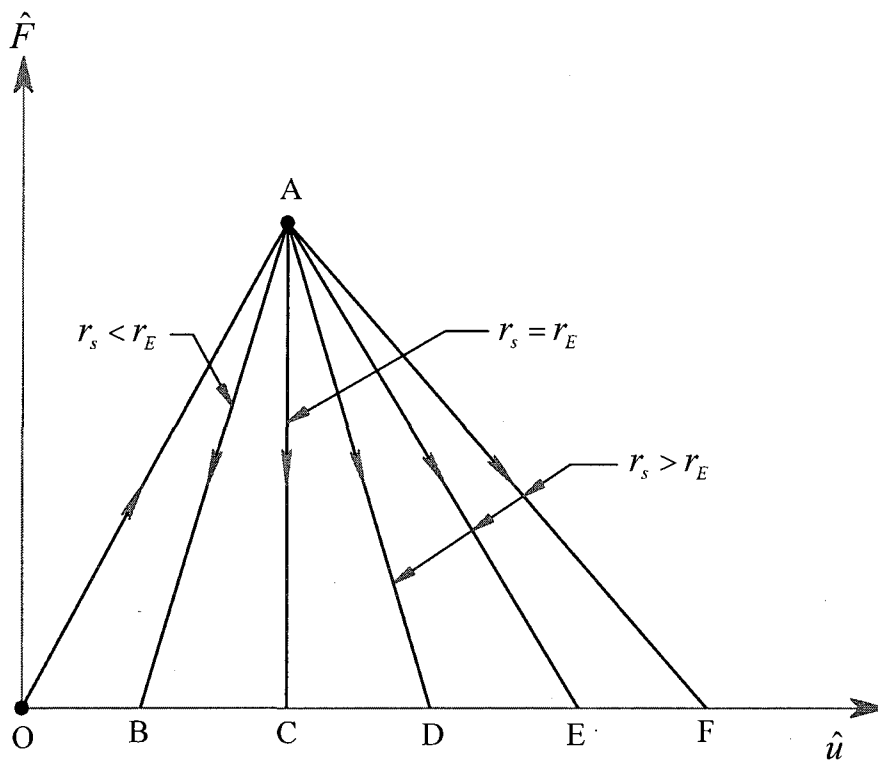
Figure 3.6 Load-displacement paths for 1-D strain softening behavior.

Table 3.1 Material parameters for the 1-D problem

Parameters	Units	Normal elements	Weak element
E_0	MPa	20000.00	20000.00
E_p	MPa	-2000.00	-2000.00
$E_s^{ep\dagger}$	MPa	-2222.22	-2222.22
$\sigma_{Y0}^{\S}$	MPa	2.00	1.80
† $E_s^{ep} = \dfrac{E_0 E_p}{E_0 + E_p}$; § σ_{Y0}: Initial yield strength				
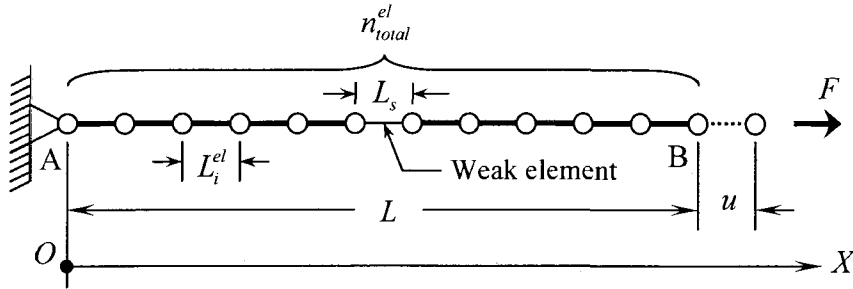
Figure 3.7 The 1-D finite element discretization and the coordinate system for computer implementation.

Table 3.2 The finite element discretization data for the 1-D problem

n_{total}^{el}	L_i^{el} † (mm)	L_s (mm)	L_e (mm)	$r_s = L_s/L_e$	$r_E = \left|E_s^{ep}\right|/E_0$
1	100	100	0	∞	0.111
3	33	34	66	0.515	0.111
5	20	20	80	0.250	0.111
7	14	16	84	0.190	0.111
9	11	12	88	0.136	0.111
11	10	10	90	0.111	0.111
21	5	5	95	0.053	0.111
101	1	1	99	0.010	0.111
† L_i^{el} is the typical length of most elements. Some elements may have length more or less than the typical length to fit the bar length.					

Figure 3.8 shows the effective plastic strain distribution for seven meshes. Notice that for all of the meshes, the plastic strains are concentrated into the weak elements located in the center of the bar. With mesh refinement, the size of weak element decreases, and the magnitude of the plastic strain in the weak element increases.
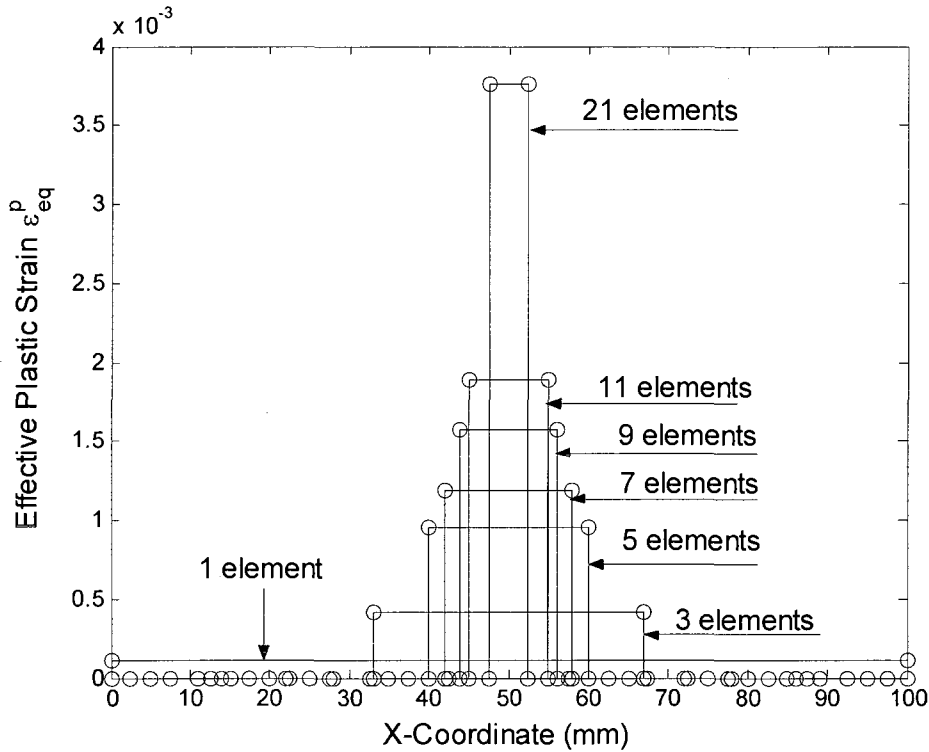
Figure 3.8 The 1-D problem: the effective plastic strain distribution. The results are mesh-dependent.

Figure 3.9 shows the load-displacement plots for six meshes. The descending branches of the load-displacement curves for different meshes follow different paths. From Table 3.2, we can see that the critical modulus ratio is $r_E = 0.111$. Because the length ratios for 1-element, 3-element, 5-element, 7-element, and 9-element meshes are greater than r_E, the descending branches for these meshes follow the softening branch. For 11-element mesh, because of $r_s = 0.111 = r_E$, the descending branch for this mesh follows the steepest-drop path. For 21-element and 101-element meshes, because their length ratios of the softening elements are less than the critical ratio, their descending branch should follow the snap-back path according to the foregoing conclusions. However, the numerical results show that their descending branches still follow the

steepest-drop path. One of the reasons for this inconsistency is that the load is displacement-controlled, and the displacement at the end B is monotonically increased. Another reason is that, to maintain the positive-definiteness of the stiffness matrices, for every load step, small positive plastic modulus is employed to form the tangential stiffness matrices, and the softening branch is simulated by reducing the unbalanced nodal forces to zero by iteration within each load step. This algorithmic process will constrain the load-displacement curve to follow the snap-back path and instead, for the meshes with $r_s < r_E$, it always follow the steepest-drop path. This phenomenon is also observed in the 2-D strain softening problems, which will be shown in the following Section 3.4.
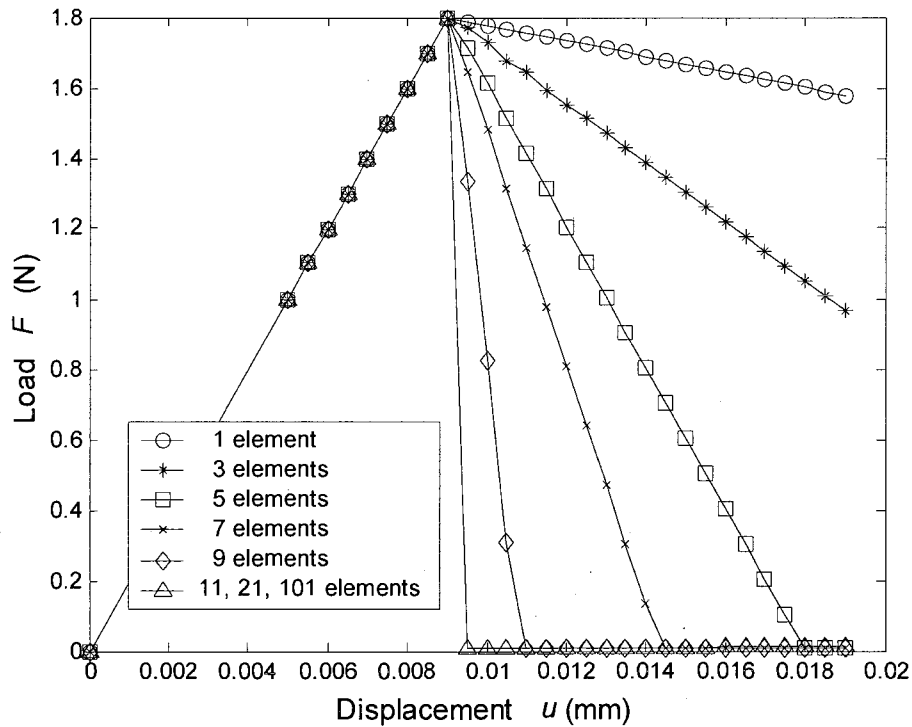
Figure 3.9 The 1-D problem: load-displacement plots. The results are mesh-dependent.

3.4 2-D Numerical Examples

3.4.1 Statement of the Problem

A 2-D problem is considered to demonstrate the shear band formation due to strain localization. Figure 3.10 shows the geometry, loading conditions, and coordinate system of a specimen under the plan strain test. Figure 3.11 shows the schematic description of the material parameters used in the computation. To prevent unrealistic response, a residual stress, σ_u , and the corresponding plastic strain ε_u^p is set to indicate that if the equivalent plastic strain $\varepsilon_{eq}^p > \varepsilon_u^p$, the yield stress will remain at σ_u .
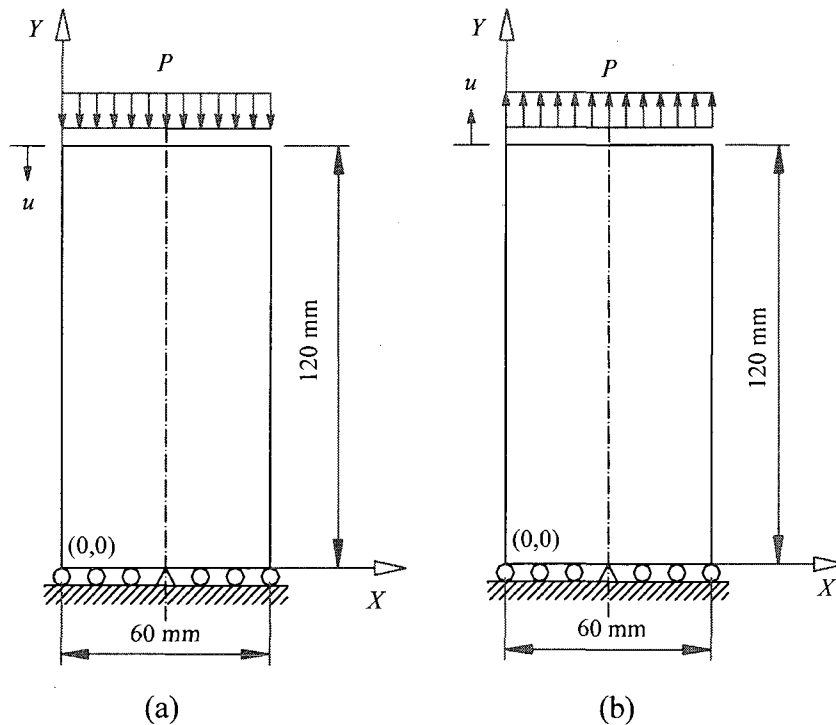
Figure 3.10 Geometry, loading conditions, and coordinate system of a specimen under plane strain test: (a) compressive test; (b) tensile test.
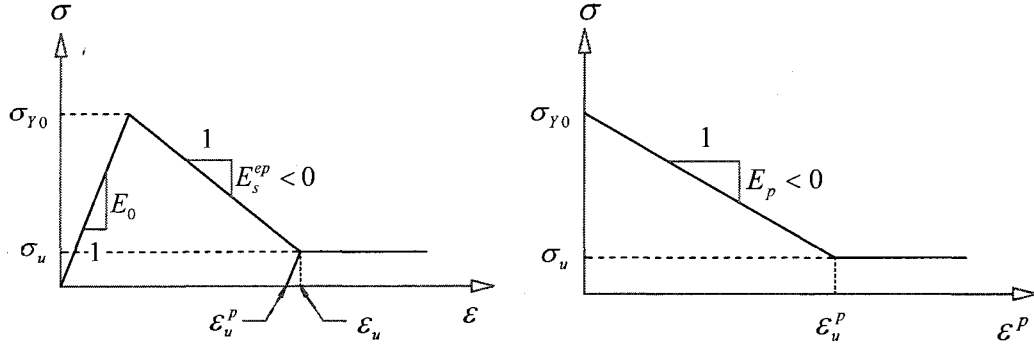
Figure 3.11. The schematic description of the material constitutive model for the 2-D problem.

The von Mises yield criterion is employed in the analysis. The yield function reads

$$f(\boldsymbol{\sigma},\eta) := \sqrt{3J_2} - \sigma_Y(\varepsilon_{eq}^p) = 0, \tag{3.21}$$

where J_2 is the second deviatoric stress invariant, which is defined as

$$J_2 = \frac{1}{2}S_{ij}S_{ij} = \frac{1}{2}\left[S_x^2 + S_y^2 + S_z^2 + 2\left(\tau_{xy}^2 + \tau_{yz}^2 + \tau_{zx}^2\right)\right]$$

$$= \frac{1}{6}\left[\left(\sigma_x - \sigma_y\right)^2 + \left(\sigma_y - \sigma_z\right)^2 + \left(\sigma_z - \sigma_x\right)^2 + 6\left(\tau_{xy}^2 + \tau_{yz}^2 + \tau_{zx}^2\right)\right] \tag{3.22}$$

$$= \frac{1}{6}\left[\left(\sigma_1 - \sigma_2\right)^2 + \left(\sigma_2 - \sigma_3\right)^2 + \left(\sigma_3 - \sigma_1\right)^2\right],$$

where S_{ij}, $i,j = 1,2,3$ or x,y,z is termed the deviatoric stress tensor and its components are defined as

$$S_{ij} = \sigma_{ij} - \delta_{ij}\sigma_m, \tag{3.23}$$

$$\sigma_m = \frac{1}{3}\left(\sigma_x + \sigma_y + \sigma_z\right) = \frac{1}{3}\left(\sigma_1 + \sigma_2 + \sigma_3\right), \tag{3.24}$$

$$\delta_{ij} = \begin{cases} 1, & i = j \\ 0, & i \neq j \end{cases}; \quad i = 1,2,3 \text{ or } x,y,z. \tag{3.25}$$

The 8-node elements are used in the computation. To trigger the initiation of the strain localization, a weak zone with lower initial yield stress has to be specified at some location and correspondingly, a weak element is specified in the finite element mesh. Also, the weak element is specified at different locations to examine the effect of the weak zone location on the pattern of the shear band localization. The loading is displacement-controlled, that is, a forced displacement, u, which is uniform along the top edge of the specimen, is incrementally specified. This loading method is necessary for simulating strain softening plasticity and the descending branch of load-displacement response.

Drucker's stability postulate [14, 25] indicates that material's behavior is stable under the condition $\dot{\sigma} : \dot{\varepsilon} > 0$. If this condition is violated, that is, $\dot{\sigma} : \dot{\varepsilon} \leq 0$, the material's behavior becomes unstable. According to Hill's theory [30], a necessary condition for any type of bifurcation and loss of uniqueness is $\dot{\sigma} : \dot{\varepsilon} = 0$. If the yielding of the material follows the von Mises yield criterion, and the associative flow rule is assumed, the conditions $\dot{\sigma} : \dot{\varepsilon} = 0$ and $\dot{\sigma} : \dot{\varepsilon} < 0$ correspond to $E_p = 0$ and $E_p < 0$, respectively. The former condition is related to perfect plasticity, and the later condition related to strain softening plasticity. From a mathematical point of view, the perfect plasticity can be viewed as an extreme case of the strain softening plasticity. Theoretically both conditions can cause the material instability and lead to strain localization. In the following numerical examples, both of these conditions are considered to demonstrate the strain localization.

3.4.2 Numerical Results

3.4.2.1 Strain Softening Plasticity:
$$E_p < 0$$

Table 3.2 lists the material parameters used in the strain softening plasticity. Three different locations of the weak zones are considered: lowerleft corner, the center of the left side, and the center of the specimen. Figure 3.12 shows the lower-left-corner weak zone. The simulation results for three different meshes, 128-element, 512-element and 2048-element meshes, with lower-left weak element are shown in Figure 3.13 through Figure 3.18.

Table 3.2. Material parameters for the 2-D strain softening problem

Parameters	Units	Normal elements	Weak element
E_0	MPa	11920.00	11920.00
v		0.20	0.20
E_p	MPa	-1192.00	-1192.00
E_s^{ep} †	MPa	-1322.22	-1322.22
σ_{Y0} §	MPa	100.00	90.00
σ_u	MPa	10.00	10.00
ε_u^p		0.0755	0.0671
ε_u		0.0763	0.0679
† $E_s^{ep} = \dfrac{E_0 E_p}{E_0 + E_p}$; § σ_{Y0}: Initial yield strength				
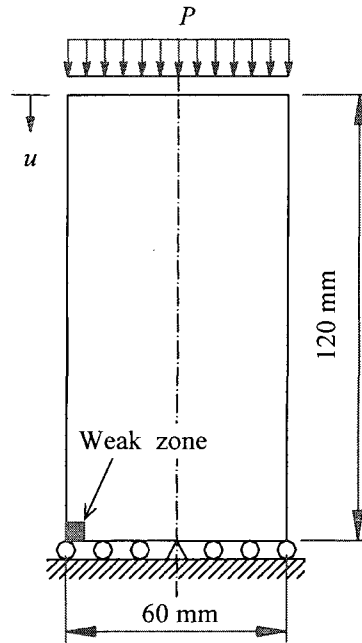
Figure 3.12 The plain strain compression test with weak zone located at the lower left corner.

(a)   (b)

(c)

Figure 3.13   Computational results of the plain strain compression test at $u = 1.3$ mm based on strain softening plasticity: (a) deformed mesh (scaling factor =3); (b) contour plot of the effective plastic strain; (c) 3-D plot of the effective plastic strain. The weak element is located at the lower left corner (see Figure 3.12). The mesh includes 128 elements and 433 nodal points.

Figure 3.14 Computational results of the plain strain compression test based on strain softening plasticity: plot of the load-displacement response. The weak element position: lower left corner. The mesh includes 128 elements and 433 nodal points.

(a)

(b)

(c)

Figure 3.15   Computational results of the plain strain compression test at $u = 1.3$ mm based on strain softening plasticity: (a) deformed mesh (scaling factor =3). (b) contour plot of the effective plastic strain. (c) 3-D plot of the effective plastic strain. The weak element is located at the lower left corner (see Figure 3.12). The mesh includes 512 elements and 1633 nodal points.

Figure 3.16 Computational results of the plain strain compression test based on strain softening plasticity: plot of the load-displacement response. The weak element position: lower left corner. The mesh includes 512 elements and 1633 nodal points.

(a)

(b)

(c)

Figure 3.17 Computational results of the plain strain compression test at $u = 1.3$ mm based on strain softening plasticity: (a) deformed mesh (scaling factor =3); (b) contour plot of the effective plastic strain; (c) 3-D plot of the effective plastic strain. The weak element is located at the lower left corner (see Figure 3.12). The mesh includes 2048 elements and 6337 nodal points.

Figure 3.18 Computational results of the plain strain compression test based on strain softening plasticity: plot of the load-displacement response. The weak element position: lower left corner. The mesh includes 512 elements and 1633 nodal points.

The shear bands form due to the localized deformation for all the three meshes. The shear bands initiate at the weak elements and propagate at about 37° with respect to the horizontal axis, separating the specimen into two blocks. It is noted that the thickness of the shear band decreases with the refinement of the mesh and become vanishingly small when the mesh grid is very fine. This result is consistent with the 1-D numerical result. The load-displacement responses, shown in Figure 3.14, Figure 3.16, and Figure 3.18, follow the steepest-drop path and the shear bands form when the load drops from the peak value down to the lowest value. The deformed meshes and the contour plots of the effective plastic strains all together show that the magnitude of the shear band width is equivalent to the size of the element employed. These results provide the evidence of the mesh-dependency of the simulation results based on classical continuum mechanics. The contour plots of the effective plastic strains show that the deformation is concentrated in the shear bands, and the plastic strains outside the shear bands are zero.

Figure 3.19 shows a weak zone located at the center of the left side of the specimen and Figure 3.20 shows the simulation results of the shear band development. We can see that the shear band still initiates at the weak element and propagates at the same angle as in the case with the weak element at the lower left corner. Also, the researchers noticed that only one shear band forms. Figure 3.21 shows a weak zone located at the center of the specimen, and Figure 3.22 shows the simulation results. Similarly, only one shear band forms and its location is different from that in other scenarios. Figure 3.19 through Figure 3.22 indicate that the location of the shear band is related to the location of the weak element.
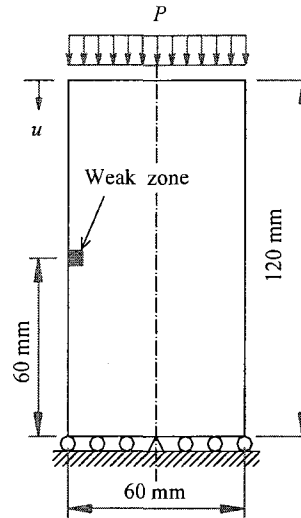
Figure 3.19. The geometry and loading condition of the plain strain compression test with weak zone located at the center of the left edge.

(a)   (b)
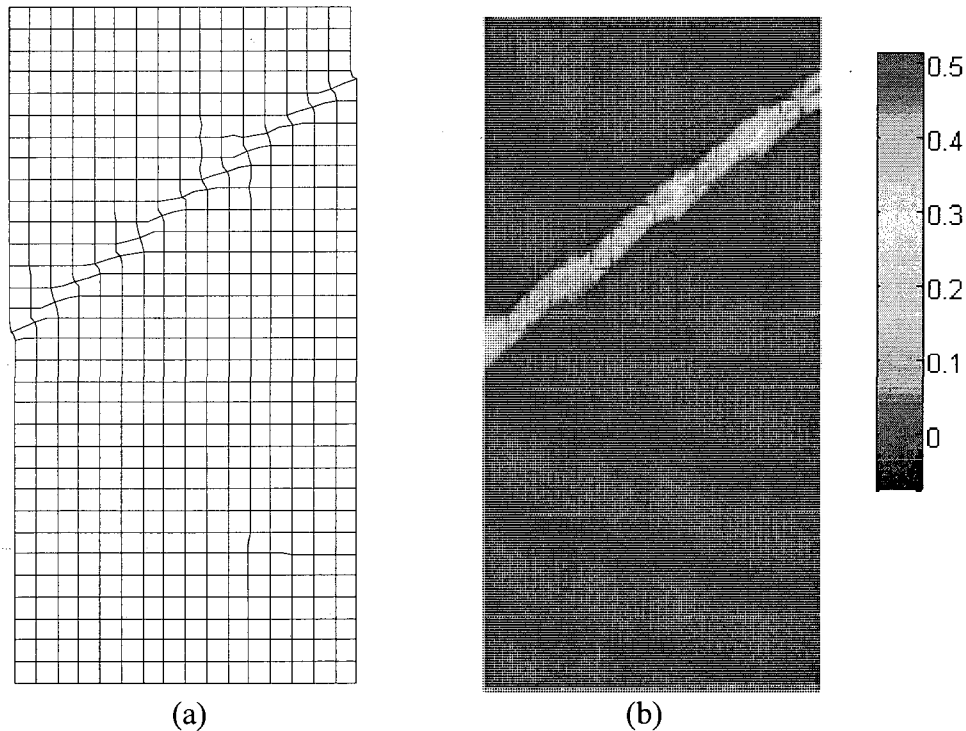
Figure 3.20. Computational results of the plain strain compression test at $u = 1.3$ mm based on strain softening plasticity: (a) deformed mesh (scaling factor $=2$). (b) contour plot of the effective plastic strain. The weak element is located at the center of the left edge (see Figure 3.19). The mesh includes 512 elements and 1633 nodal points.
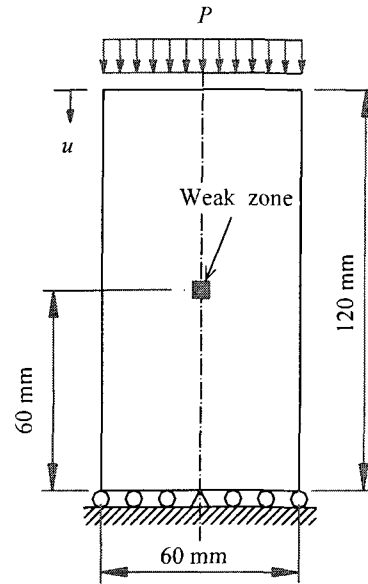
Figure 3.21. The geometry and loading condition of the plain strain compression test with weak zone located at the center of the specimen.

(a)   (b)
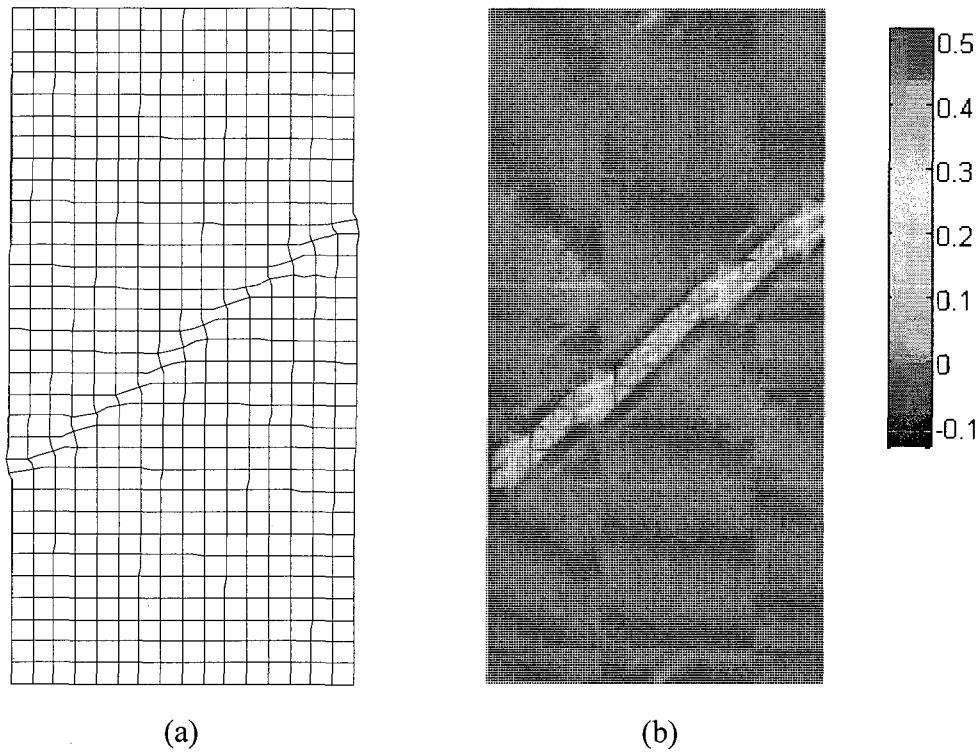
Figure 3.22. Computational results of the plain strain compression test at $u = 1.3$ mm based on strain softening plasticity: (a) deformed mesh (scaling factor =2); (b) contour plot of the effective plastic strain. The weak element is located at the center of specimen (see Figure 3.21). The mesh includes 512 elements and 1633 nodal points.

3.4.2.2 <u>Perfect Plasticity:</u> $E_p = 0$

Table 3.4 lists the material parameters used in the perfect plasticity. Figure 3.23 through Figure 3.31 show the simulation results for different weak zone locations and different loading conditions. The shear band patterns caused by perfect plasticity are different from those caused by the strain softening plasticity. If the weak zone is at the lower left corner, only one shear band forms (see Figure 3.23). However, if the weak zone is at the center of the left side of the specimen, The two shear bands are formed in different directions (see Figure 3.25). If the weak zone is at the center of the specimen, the two groups of shear bands are formed each developing in different directions but with symmetry with respect to the center axis of the specimen. The results are the same no matter if the loading is compressive or tensile (see Figure 3.27 and Figure 3.30).

Table 3.4. Material parameters for the 2-D perfect plasticity

Parameters	Units	Normal elements	Weak element
E_0	MPa	200000.00	100000.00
v		0.30	0.30
E_p	MPa	0	0
E_s^{ep} †	MPa	0	0
σ_{Y0} §	MPa	300.00	150.00
† $E_s^{ep} = \dfrac{E_0 E_p}{E_0 + E_p}$; § σ_{Y0} : Initial yield strength			

The load-displacement plots resulting from the perfect plasticity model are substantially different from those from the strain softening plasticity model. Figure 3.24, Figure 3.26, Figure 3.28, and Figure 3.31 show that the shear band formation initiates and develops in the plastic flow phase. The load level is maintained unchanged with the

displacement increasing during the shear band development, which is completely different from the load-displacement response from the strain softening plasticity model (see Figure 3.14, 3.16, 3.18). Also, the magnitude of the thickness of the shear bands resulting from the perfect plasticity model is about 2 ~ 3 times the size of the element, which is obviously different from the results of the strain softening plasticity model. These results indicate that the governing differential equations for the perfect plasticity are different from that for the strain softening plasticity even though both the models exhibit the material instability and the strain localization.
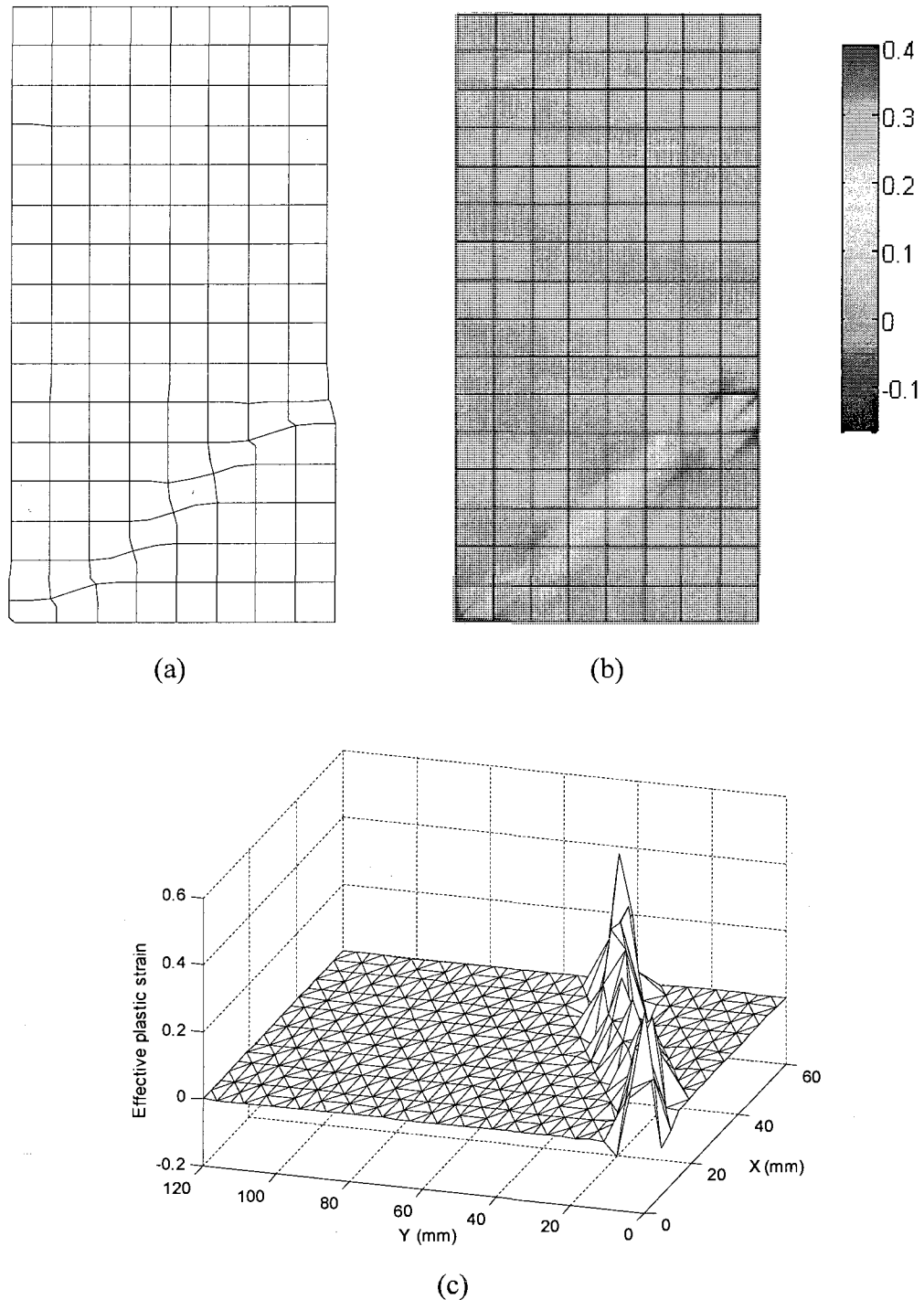
(a)

(b)

(c)
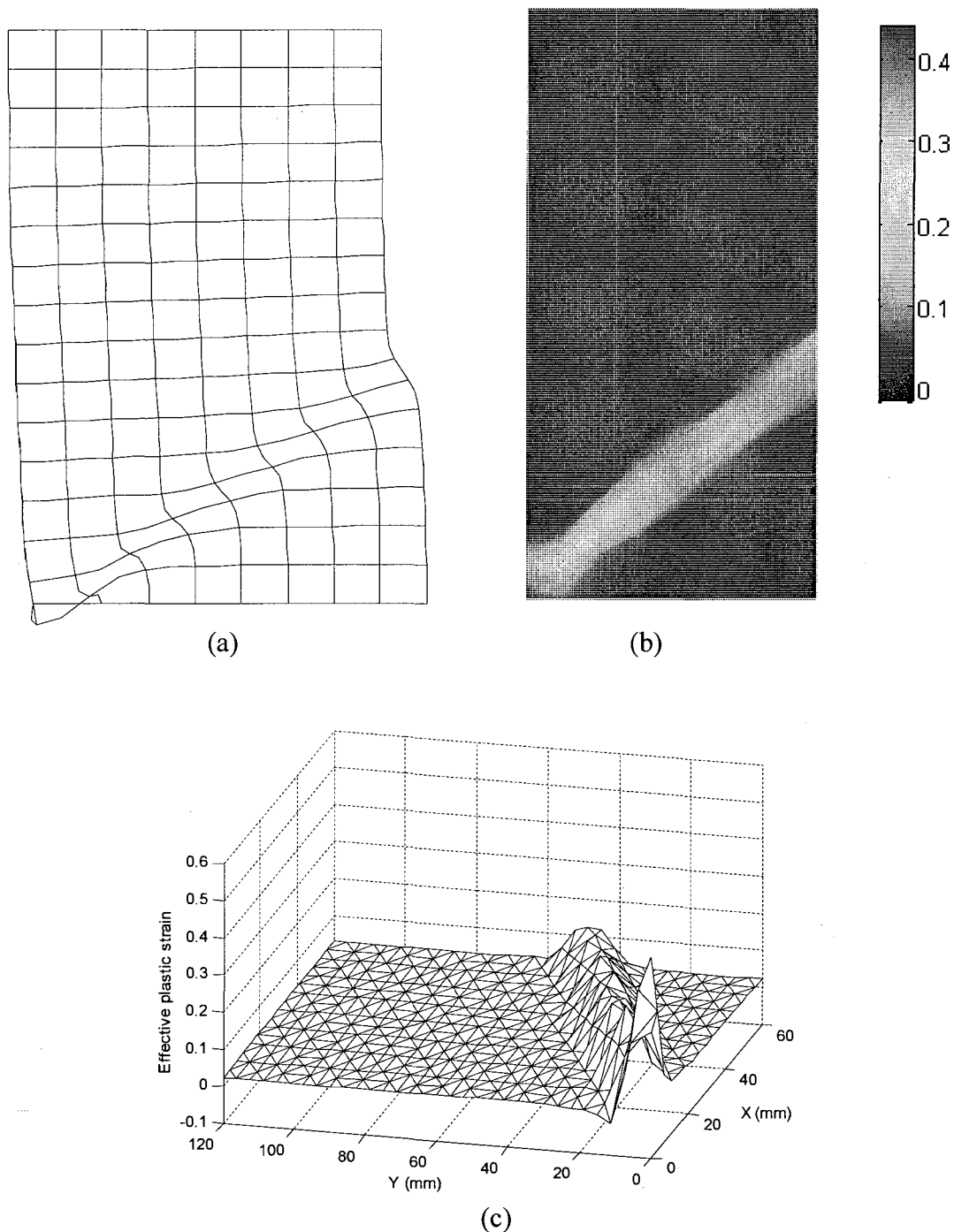
Figure 3.23. Computational results of the plain strain compression test at
u = 4.5 mm based on perfect plasticity: (a) deformed mesh (scaling factor =5); (b)
contour plot of the effective plastic strain; (c) 3-D plot of the effective plastic strain. The
weak element is located at the lower left corner of the specimen (See Figure 3.12). The
mesh includes 128 elements and 433 nodal points.
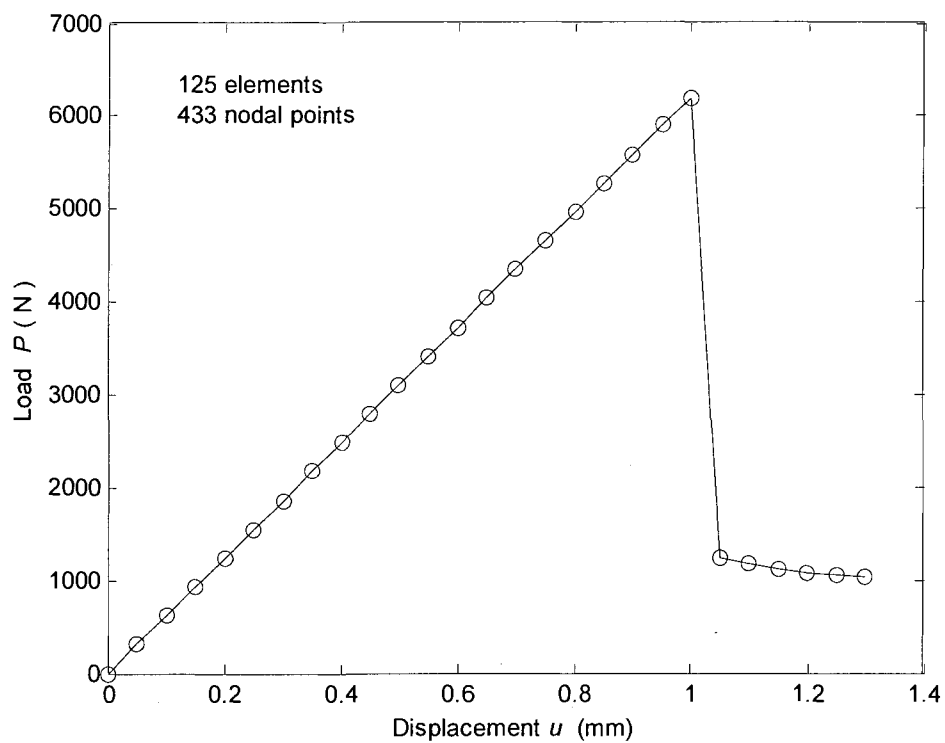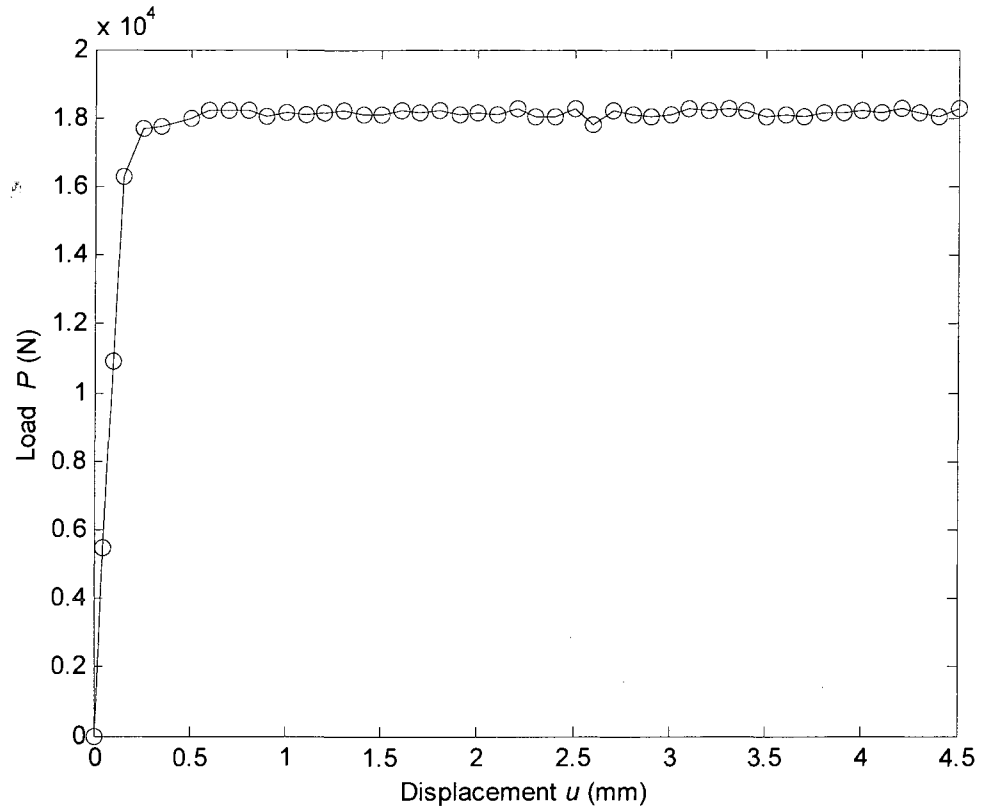
Figure 3.24 Computational results of the plain strain compression test based on perfect plasticity: plot of the load-displacement response. The weak element position: lower left corner. The mesh includes 128 elements and 433 nodal points.
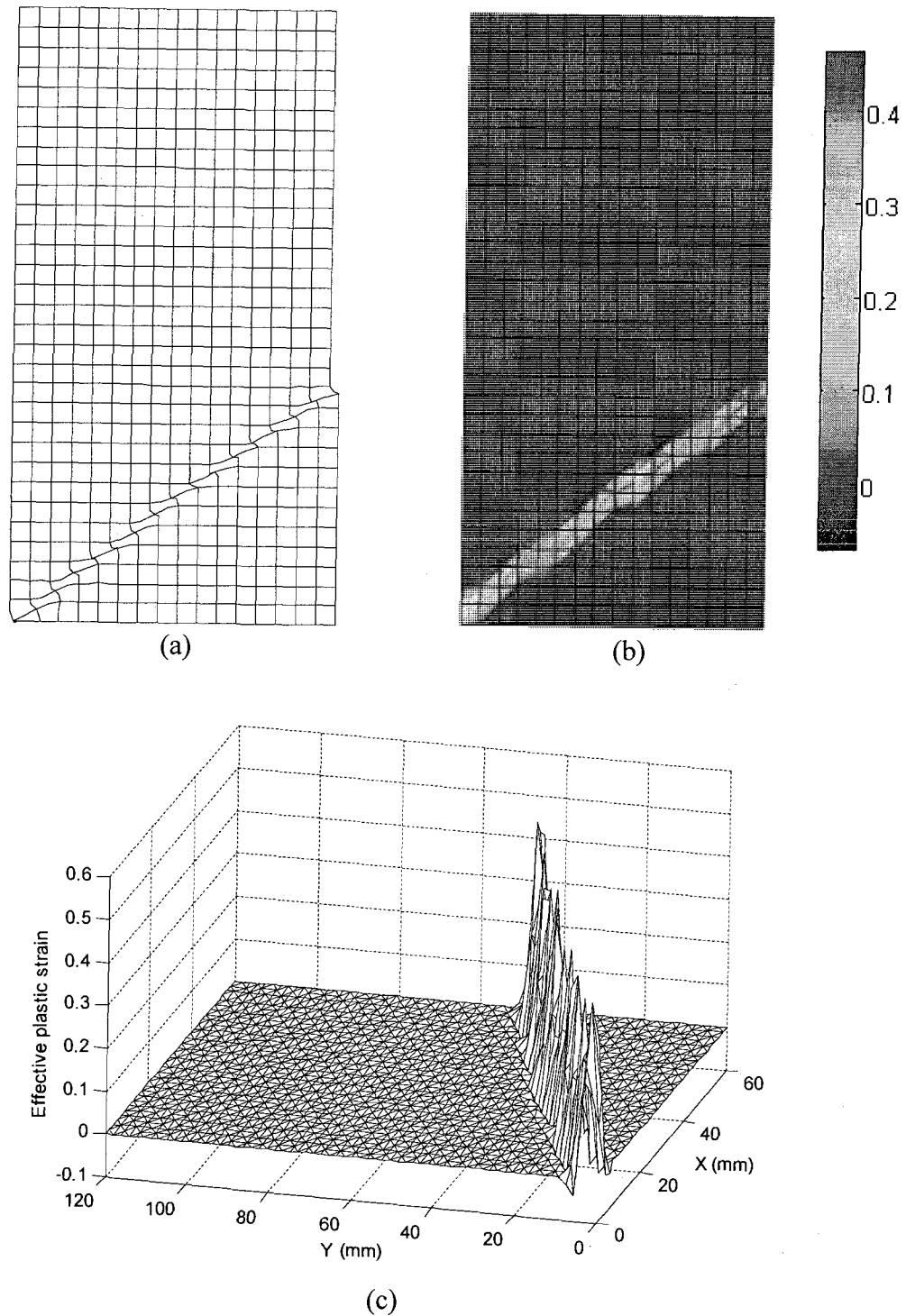
(a)   (b)

(c)
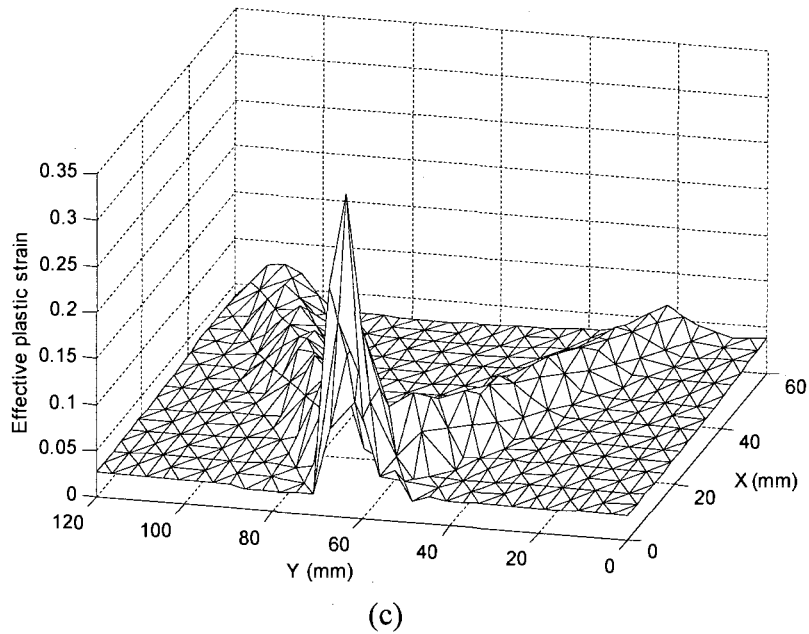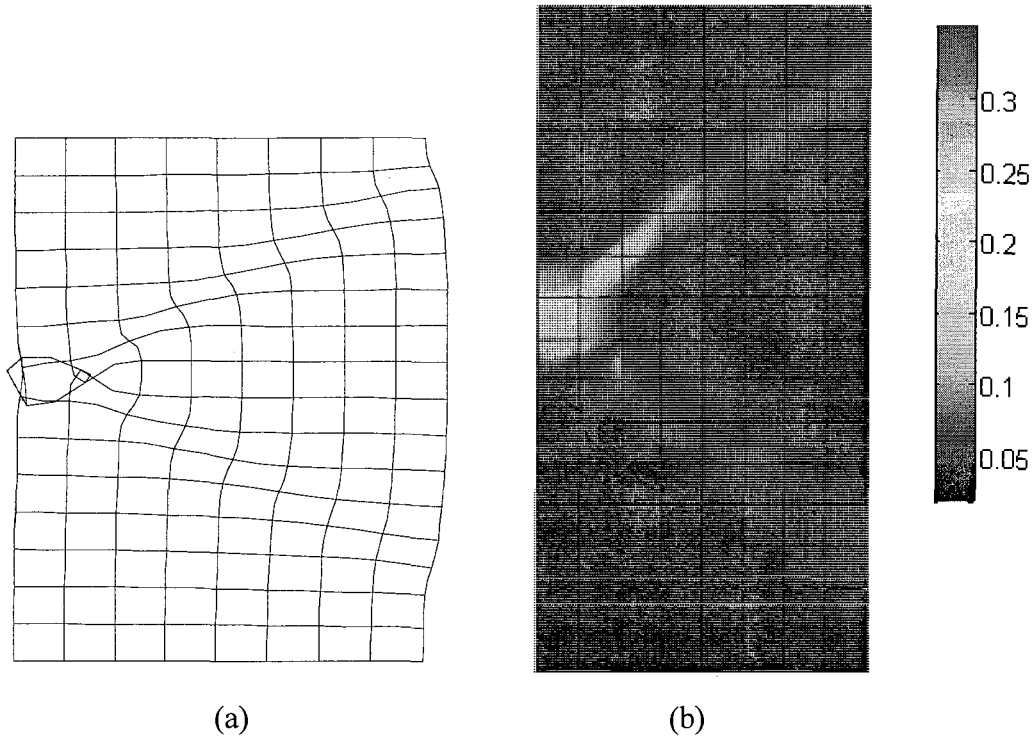
Figure 3.25 Computational results of the plain strain compression test at
u = 4.5 mm based on perfect plasticity: (a) deformed mesh (scaling factor =8); (b)
Contour plot of the effective plastic strain; (c) 3-D plot of the effective plastic strain. The
weak element is located at the lower left corner of the specimen (See Figure 3.12). The
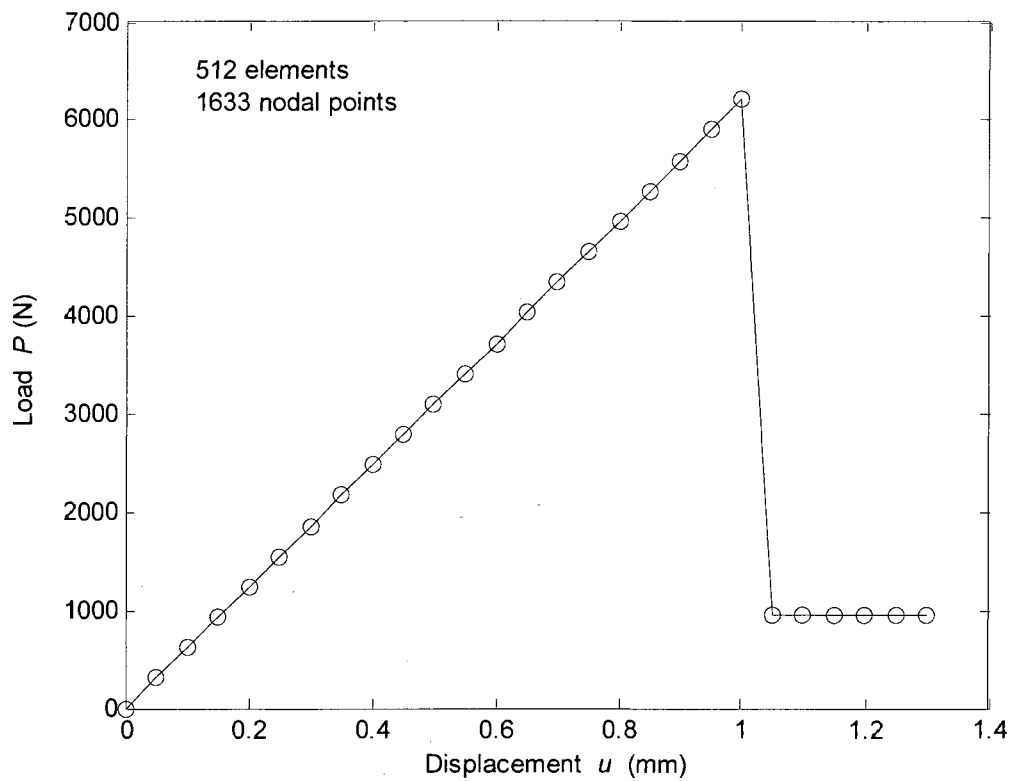mesh includes 128 elements and 433 nodal points.
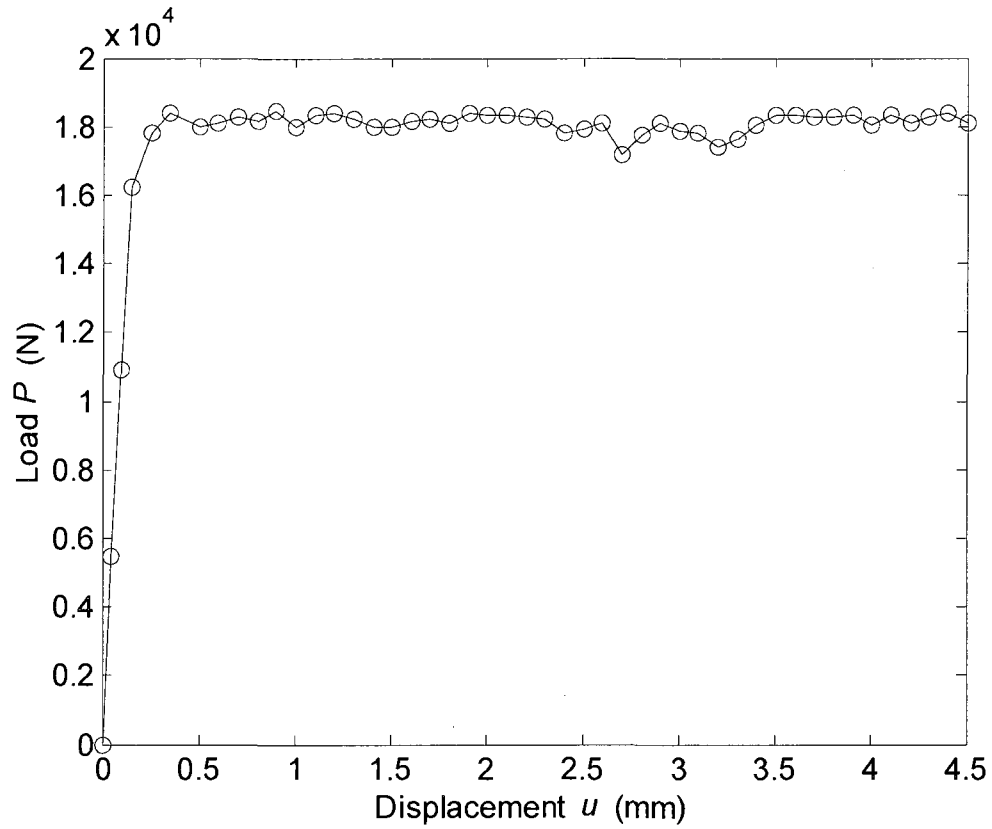
Figure 3.26 Computational results of the plain strain compression test based on perfect plasticity: plot of the load-displacement response. The weak element position: lower left corner. The mesh includes 128 elements and 433 nodal points.
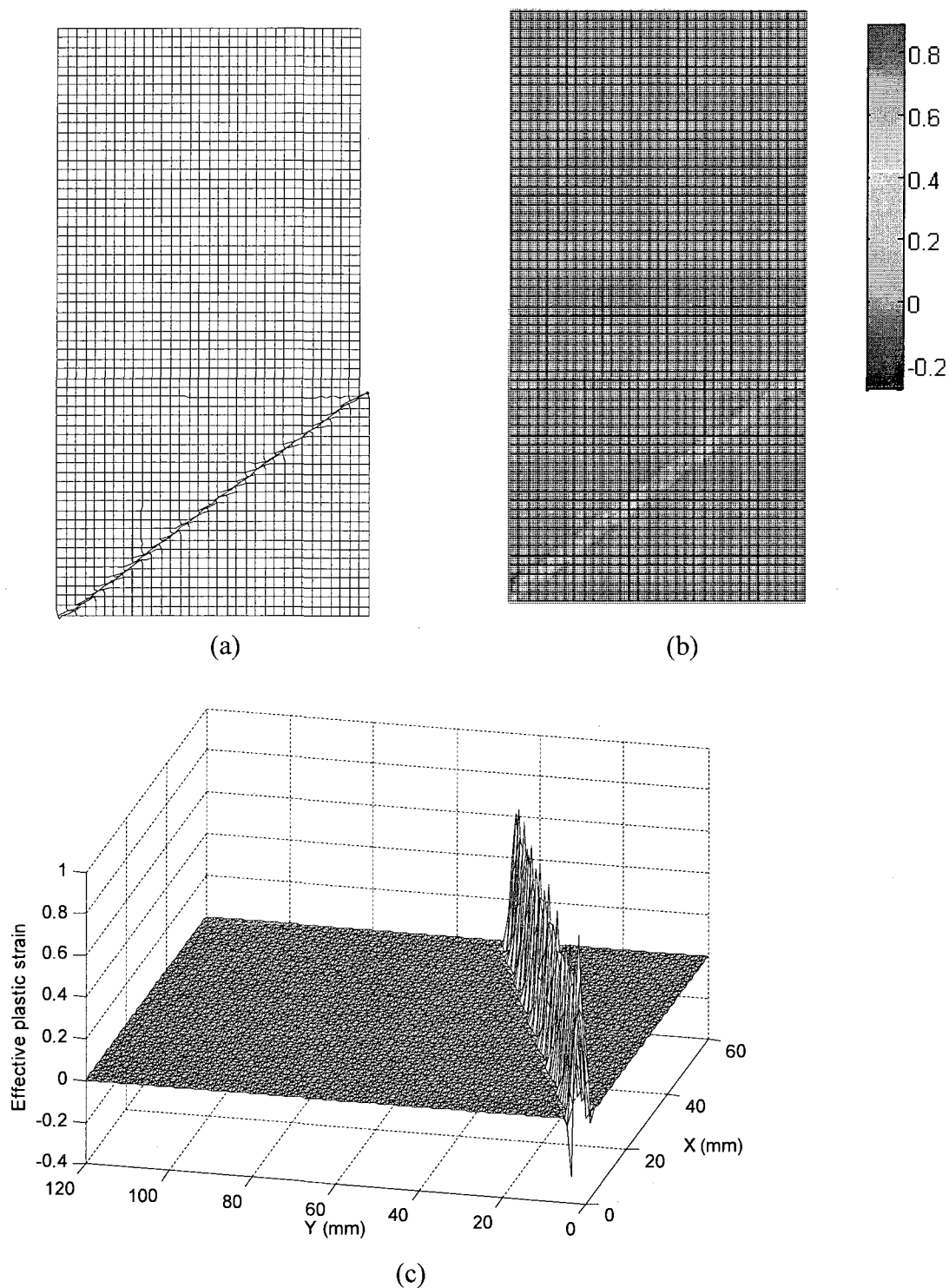
(a)

(b)

(c)
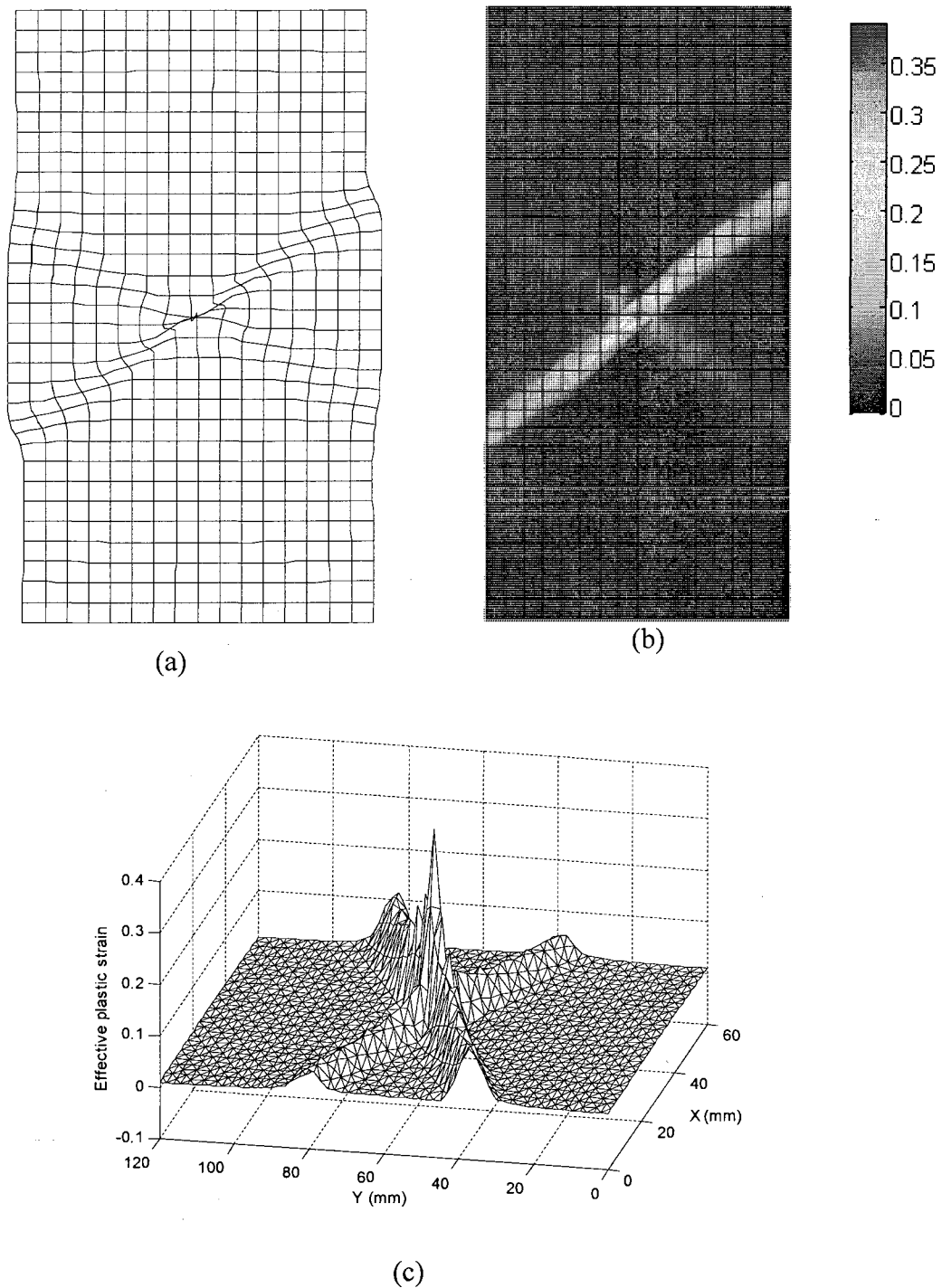
Figure 3.27 Computational results of the plain strain compression test at
$u = 2.6$ mm based on perfect plasticity: (a) deformed mesh (scaling factor =5); (b)
contour plot of the effective plastic strain; (c) 3-D plot of the effective plastic strain. The
weak element is located at the center of the specimen (See Figure 3.21). The mesh
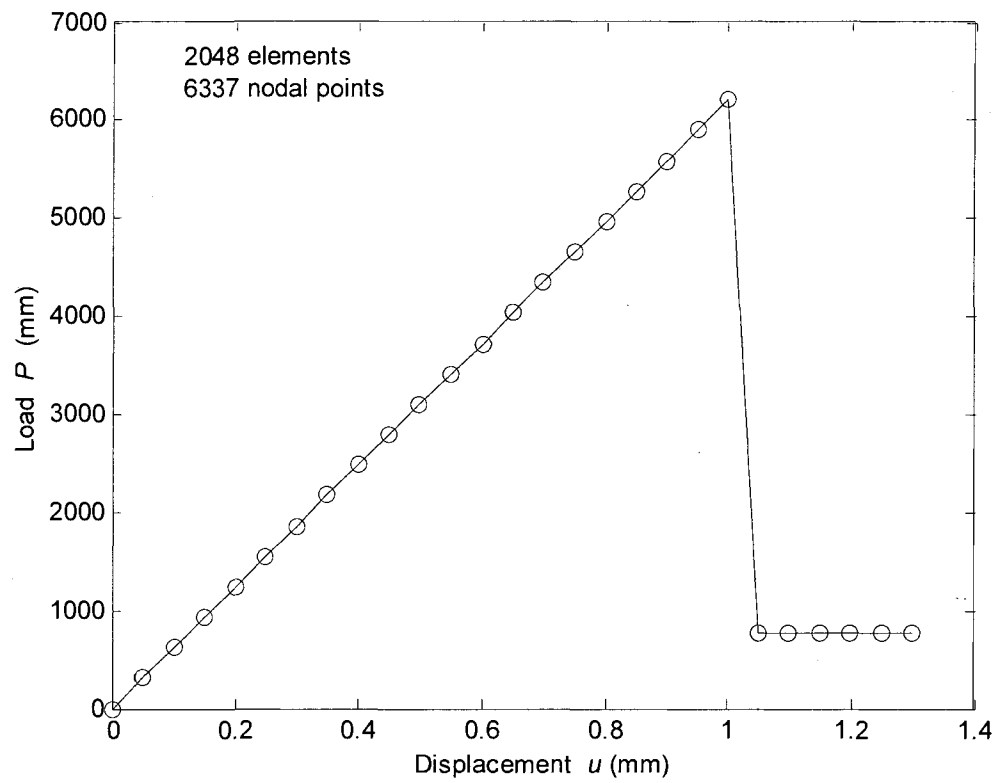includes 512 elements and 1633 nodal points.
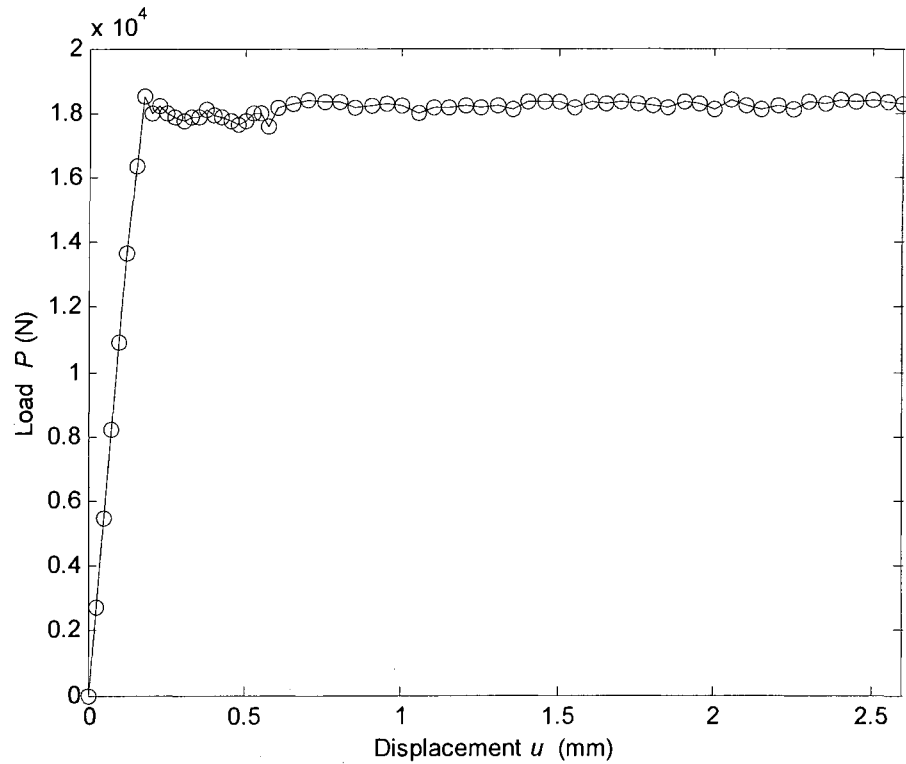
Figure 3.28 Computational results of the plain strain compression test based on perfect plasticity: plot of the load-displacement response. The weak element position: the center of the specimen. The mesh includes 512 elements and 1633 nodal points.
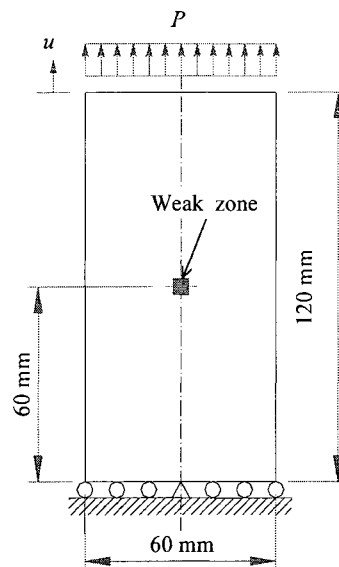
Figure 3.29 The geometry and loading condition of the plain strain tensile test with the weak zone located at the center of the specimen.

(a)

(b)

(c)
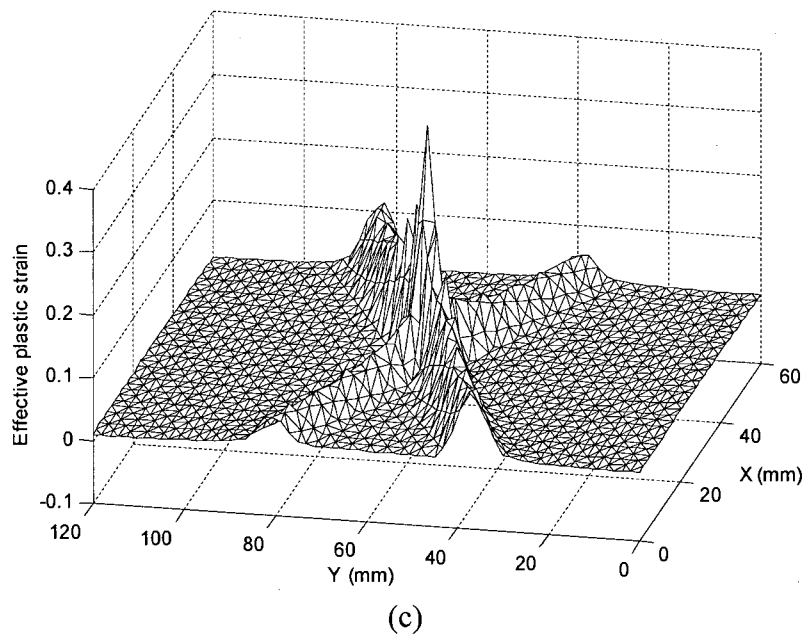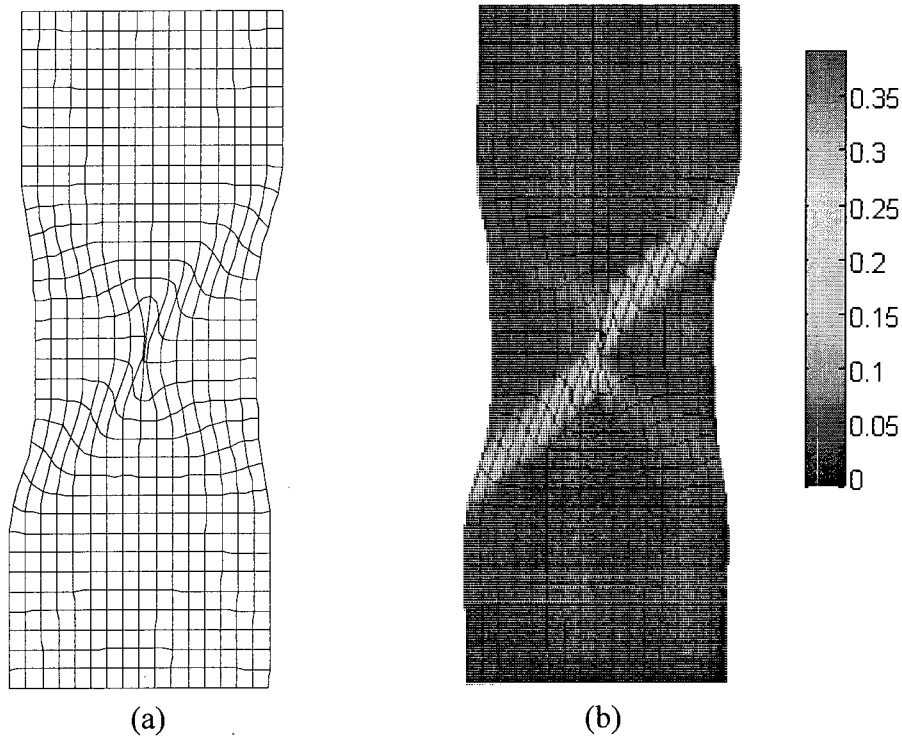
Figure 3.30 Computational results of the plain strain tensile test at u = 2.6 mm based on perfect plasticity: (a) deformed mesh (scaling factor =10); (b) contour plot of the effective plastic strain; (c) 3-D plot of the effective plastic strain. The weak element is located at the center of the specimen (See Figure 3.21). The mesh includes 512 elements and 1633 nodal points.
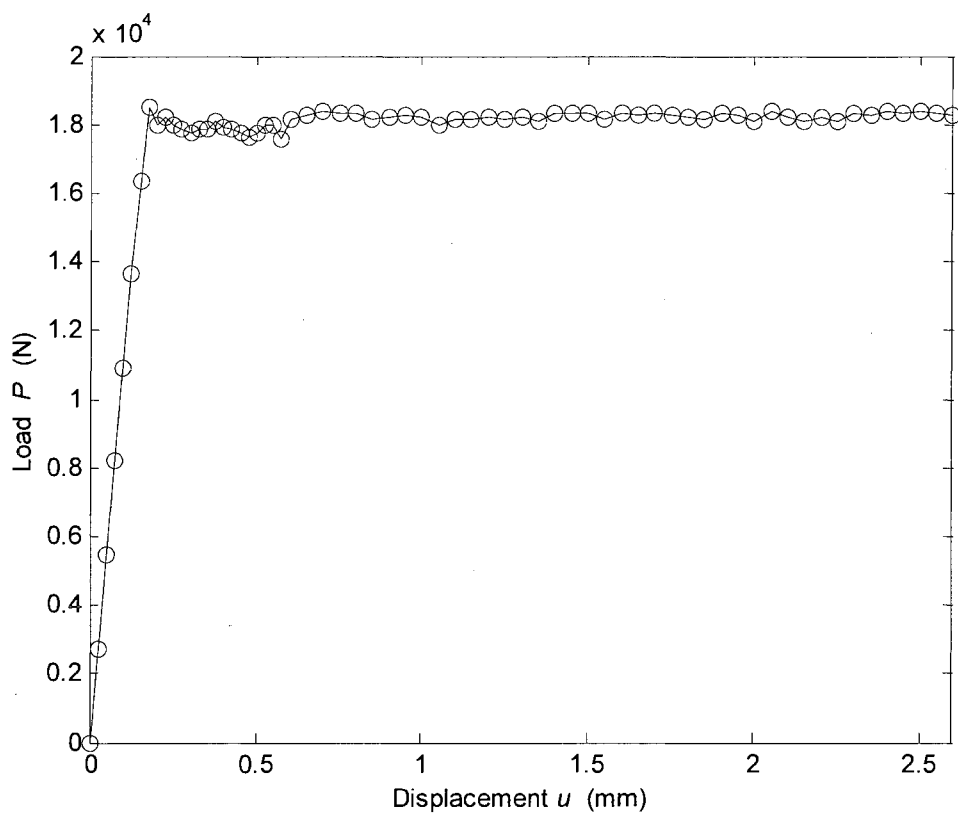
Figure 3.31 Computational results of the plain strain tensile test based on perfect plasticity: plot of the load-displacement response. The weak element position: the center of the specimen. The mesh includes 512 elements and 1633 nodal points.

3.5 <u>Summary</u>

Two computer programs, EP1D and EPLAS, are developed to simulate strain localization caused by strain softening plasticity for 1-D and 2-D problems, respectively. The two-noded constant stress element is used in EP1D and 4-node isoparametric quadrilateral element. The 8-node Serendipity quadrilateral element and the 9-node Lagrangian quadrilateral element are used in EPLAS. The 8-node Serendipity quadrilateral element is employed in the 2-D numerical example. The program structure is outlined in Figure 3.1. Strain localization and shear band localization are well demonstrated through 1-D and 2-D numerical examples using the developed computer programs. Seven different meshes for the 1-D problem and three different meshes for the 2-D problems are used in the illustration of the mesh dependency of the simulation results based on the classical continuum mechanics. Different locations of the weak zone are specified to examine the relations of the shear band position with the weak zone location. As an extreme case of the strain softening plasticity, a perfect plasticity model is also used in the simulation, and the resulting shear band patterns are compared with the results from the strain softening model. The comparison indicates that the shear band patterns and load-displacement responses for these two models are obviously different. The reason for this difference is that the governing differential equations for the two models are different even though both the models can exhibit material instability and strain localization.

CHAPTER 4

COMPARISON OF BOUNDARY CONDITIONS
OF GRADIENT ELASTICITY AND
GRADIENT PLASTICITY

4.1 Introduction

As demonstrated in Chapter 3, the computational simulation of strain localization

based on classical continuum mechanics suffers from spurious mesh dependency. Several

methods and theories have been proposed to regularize the mesh dependency, among

which the gradient plasticity theory provides well-posed governing differential equations

for the strain softening problems (see Aifantis [54, 55] and de Borst [60, 63]).

The gradient plasticity theory is the extension of the gradient elasticity theory to

the description of plastic behavior. Both gradient theories, gradient elasticity, and

gradient plasticity theories, are within the framework of nonlocal continuum mechanics

(see Eringen [56] and Bažant [57]) and are appropriate for describing heterogeneous

phenomena [54-57]. The common feature of these two gradient theories is that the

higher-order gradients of constitutive quantities (e.g. stresses or strains) enter the

constitutive models and result in the constitutive equations to be 2nd or higher order

differential equations [54; 58-60]. To solve the differential constitutive equations,

appropriate boundary conditions have to be introduced. However, gradient elasticity and

gradient plasticity are proposed for different purposes with analogous mathematical

expressions [59; 61]. The purpose of gradient elasticity is to smooth the heterogeneity, while that of the gradient plasticity is to introduce heterogeneity (see Askes [62]). To fulfill these contrary purposes, different boundary conditions should be adopted. Up to now, the boundary conditions have not been thoroughly investigated and clearly specified, especially for the nonstandard ones. While research on the boundary conditions in the literature so far is mainly addressed from the physical point of view (see Polizzotto [61]), the studies from the mathematical point of view are lacking.

In this chapter, two one-dimensional (1-D) bars under tension, one for gradient elasticity and the other for gradient plasticity, are solved analytically using Neumann and Dirichlet boundary conditions, respectively. The resulting solutions are compared to examine the regularizing effects of different boundary condition on the strain fields in order to identify the correct boundary conditions for the gradient plasticity model to regularize the mesh dependency of the simulation of the strain localization. The stability and uniqueness of the solutions for two versions of the 2nd order gradient models, involving l^2 and $(-l^2)$ (l is the internal length scale), respectively, are also illustrated and discussed. The results obtained in this chapter will provide the theoretical evidence for the application of the nonlocal model developed in Chapter 5 to the simulation of the strain localization.

4.2 Gradient Elasticity for Regularizing Singularities

The general constitutive equation in the gradient elasticity theory reads

$$\boldsymbol{\sigma} = \lambda(\operatorname{tr}\boldsymbol{\varepsilon})\boldsymbol{1} + 2\mu\boldsymbol{\varepsilon} - c\nabla^2[\lambda(\operatorname{tr}\boldsymbol{\varepsilon})\boldsymbol{1} + 2\mu\boldsymbol{\varepsilon}], \qquad (4.1)$$

where $\boldsymbol{\sigma}$ is Cauchy stress tensor and $\boldsymbol{\varepsilon}$ the strain tensor, λ and μ are Lamé constants, and c is a gradient coefficient that is related to the internal length scale of the material, l.

Consider a 1-D bar of length L and cross-section area A (Figure 4.1) [61], given that one end at $x = -L/2$ is fixed and the other end $x = +L/2$ subjected to a uniformly distributed load p, which is equivalent to a uniformly distributed stress $\sigma = p/A$ along the bar. The bar is made of two sections that have equal lengths and cross-section areas, but different Young's modulus E and βE, respectively, implying that there is a material property jump at the interface of the two sections. Obviously, application of classical continuum mechanics to this nonhomogeneous bar will lead to a singularity of the strain field at the middle section of the bar. To avoid this problem, a gradient elasticity model has to be used. In this one-dimensional case, the constitutive equation (4.1) reduces to

$$\sigma = E(\varepsilon - c\frac{\partial^2 \varepsilon}{\partial x^2}) \qquad \forall : -L/2 \leq x \leq L/2 . \tag{4.2}$$
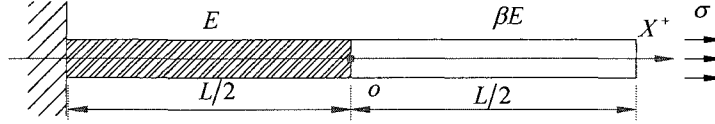
Figure 4.1. One-dimensional bar with jump of Young's modulus.

Let the origin of material coordinate axis, x, be in the center of the bar. The standard boundary conditions are

$$\varepsilon^+(0) = \varepsilon^-(0) , \tag{4.3}$$

$$(\partial \varepsilon^+ / \partial x) = (\partial \varepsilon^- / \partial x) \quad \text{at } x = 0 , \tag{4.4}$$

$$\sigma^-(-\tfrac{L}{2} \leq x \leq 0^-) = \sigma , \tag{4.5}$$

$$\sigma^+(0^+ \leq x \leq +\tfrac{L}{2}) = \sigma , \tag{4.6}$$

and the non-standard boundary conditions read

$$(\partial \varepsilon^+/\partial x) = 0 \quad \text{at} \quad x = L/2, \tag{4.7}$$

$$(\partial \varepsilon^-/\partial x) = 0 \quad \text{at} \quad x = -L/2, \tag{4.8}$$

where boundary condition (4.4), (4.7) and (4.8) are Neumann boundary conditions. The differential constitutive Equation (4.2) with the boundary conditions (4.3) – (4.8) results in two types of analytical solutions, hyperbolic functions and harmonic functions, depending on the sign of the coefficient c.

(a) *Hyperbolic solution* ($c = l^2$)

If $c = l^2$, where l is the internal length scale, Equation (4.2) can be rewritten as

$$\sigma = E(\varepsilon - l^2 \frac{\partial^2 \varepsilon}{\partial x^2}) \ , \quad \forall : -L/2 \le x \le L/2. \tag{4.9}$$

The general analytical solutions of the above differential equation are of the following exponential form:

$$\varepsilon^-(x) = c_1^- e^{\frac{x}{l}} + c_2^- e^{-\frac{x}{l}} + c_3^-, \quad \forall : -L/2 \le x \le 0, \tag{4.10a}$$

$$\varepsilon^+(x) = c_1^+ e^{\frac{x}{l}} + c_2^+ e^{-\frac{x}{l}} + c_3^+, \quad \forall : 0 \le x \le L/2. \tag{4.10b}$$

Application of boundary conditions (4.3) – (4.8) to the above equations results in the constants c_1^-, c_2^-, c_3^-, c_1^+, c_2^+, and c_3^+ to be as follow

$$c_1^- = \varepsilon_0 \left(\frac{1-\beta}{\beta} \right) \left(\frac{e^{L/l} - 1}{2(e^{L/l} - e^{-L/l})} \right); \ c_2^- = \varepsilon_0 \left(\frac{1-\beta}{\beta} \right) \left(\frac{1 - e^{-L/l}}{2(e^{L/l} - e^{-L/l})} \right); \ c_3^- = \varepsilon_0, \tag{4.11a}$$

$$c_1^+ = -c_2^- ; \ c_2^+ = -c_1^- ; \ c_3^+ = \varepsilon_0/\beta \ . \tag{4.11b}$$

where $\varepsilon_0 = \sigma/E$. Substitution of (4.11a) and (4.11b) into (4.10a) and (4.10b) gives the following hyperbolic solutions

$$\varepsilon^-(x) = \varepsilon_0 \left(\frac{1-\beta}{\beta} \right)\left(\cosh\left(\frac{x}{l} \right) + \tanh\left(\frac{L}{2l} \right)\sinh\left(\frac{x}{l} \right) \right) + \varepsilon_0, \quad \forall : -L/2 \le x \le 0,$$

$$(4.12a)$$

$$\varepsilon^+(x) = -\varepsilon_0 \left(\frac{1-\beta}{\beta} \right)\left(\cosh\left(\frac{x}{l} \right) - \tanh\left(\frac{L}{2l} \right)\sinh\left(\frac{x}{l} \right) \right) + \frac{\varepsilon_0}{\beta}, \quad \forall : 0 \le x \le L/2.$$

$$(4.12b)$$

(b) *Harmonic solution* ($c = -l^2$)

If $c = -l^2$, Equation (4.2) becomes

$$\sigma = E(\varepsilon + l^2 \frac{\partial^2 \varepsilon}{\partial x^2}), \quad \forall : -L/2 \le x \le L/2. \qquad (4.13)$$

The general solution is

$$\varepsilon^-(x) = c_1^- \sin\left(\frac{x}{l} \right) + c_2^- \cos\left(\frac{x}{l} \right) + c_3^-, \quad \forall : -L/2 \le x \le 0, \qquad (4.14a)$$

$$\varepsilon^+(x) = c_1^+ \sin\left(\frac{x}{l} \right) + c_2^+ \cos\left(\frac{x}{l} \right) + c_3^+, \quad \forall : 0 \le x \le L/2. \qquad (4.14b)$$

Applying the same boundary condition (4.3) – (4.8) to the above equations gives

$$c_1^- = \frac{1}{2}\varepsilon_0 \left(\frac{\beta-1}{\beta} \right)\tan\left(\frac{L}{2l} \right), \quad c_2^- = \frac{1}{2}\varepsilon_0 \left(\frac{1-\beta}{\beta} \right), \quad c_3^- = \varepsilon_0, \qquad (4.15a)$$

$$c_1^+ = c_1^-, \quad c_2^+ = -c_2^-, \quad c_3^+ = \varepsilon_0/\beta. \qquad (4.15b)$$

The final solution of strain field is of harmonic type:

$$\varepsilon^-(x) = \frac{1}{2}\varepsilon_0 \left(\frac{1-\beta}{\beta} \right)\left(\cos\left(\frac{x}{l} \right) - \tan\left(\frac{L}{2l} \right)\sin\left(\frac{x}{l} \right) \right) + \varepsilon_0, \quad \forall : -L/2 \le x \le 0, \quad (4.16a)$$

$$\varepsilon^+(x) = -\frac{1}{2}\varepsilon_0 \left(\frac{1-\beta}{\beta} \right)\left(\cos\left(\frac{x}{l} \right) + \tan\left(\frac{L}{2l} \right)\sin\left(\frac{x}{l} \right) \right) + \frac{\varepsilon_0}{\beta} \quad \forall : 0 \le x \le L/2. \quad (4.16b)$$

As an example, given $L = 500\,\text{mm}$, $\varepsilon_0 = 0.0001$, the two types of solutions for different values of β and l, are plotted in Figure 4.2. As shown in the figure, the strain jump caused by the material property jump at the mid section of the bar is smoothed due to the introduction of the standard Neumann boundary condition (4.4) and nonstandard ones, (4.7) and (4.8). The hyperbolic function gives a stable and unique solution of the strain distribution. However, the harmonic solution, although satisfying all the boundary conditions, gives nonrealistic and unstable strain distributions, which were also demonstrated by Altan and Aifantis [59] and other authors [62]. It is also shown that the strain distribution is affected by the internal length scale l.
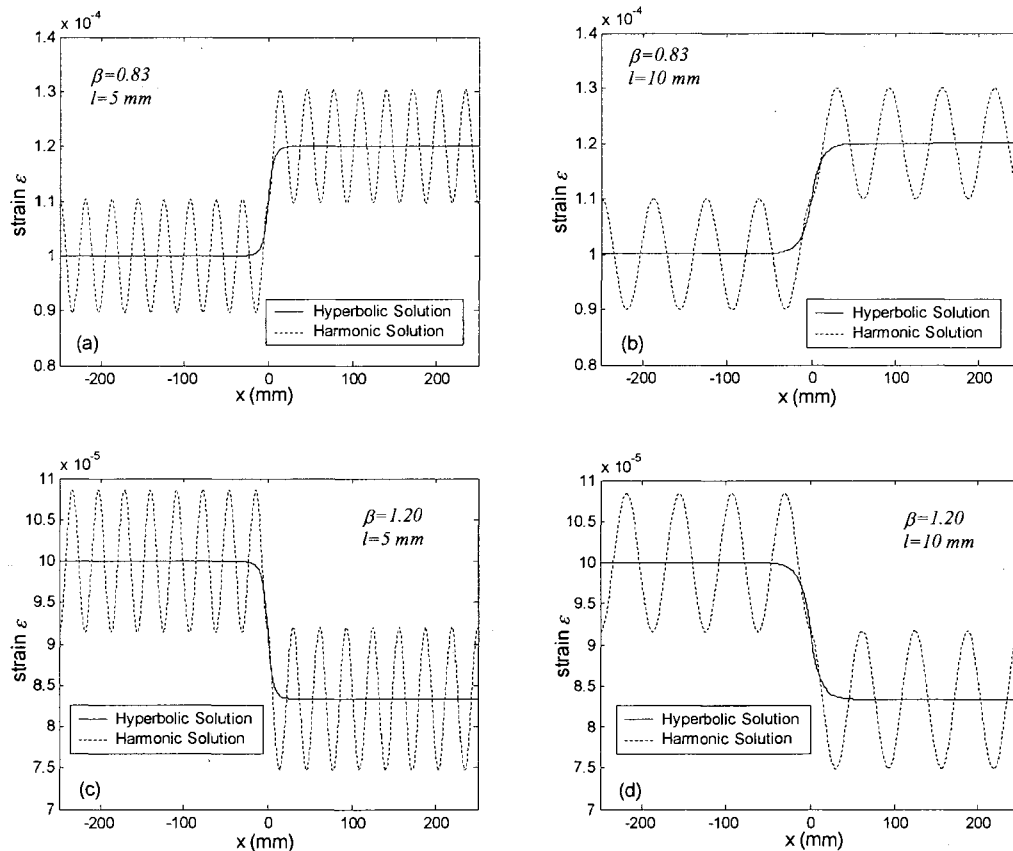
Figure 4.2 Elastic strain distribution resulting from gradient elasticity model.

4.3 Gradient Plasticity for Regularizing
Mesh-Dependency of Strain Localization

In the gradient plasticity theory, the yield function in the stress space depends not only on stress state and internal state variables, but also on the spatial gradient of the internal state variables [54, 55, 60, 63]. The yield function of the 2nd-order gradient plasticity model has the following general form [55, 63]:

$$f(\boldsymbol{\sigma}, \eta, \nabla^2 \eta) = 0 . \tag{4.17}$$

The flow rule and hardening/softening law obey the following Kuhn-Tucker complementarity condition [43]

$$\gamma \geq 0 , \quad f(\boldsymbol{\sigma}, \eta, \nabla^2 \eta) \leq 0, \quad \text{and} \quad \gamma f(\boldsymbol{\sigma}, \eta, \nabla^2 \eta) = 0, \tag{4.18}$$

and the consistency requirement

$$\gamma \dot{f}(\boldsymbol{\sigma}, \eta, \nabla^2 \eta) = 0, \tag{4.19}$$

where η is the internal state variable and γ is the consistency parameter. During plastic loading, $\gamma > 0$, consistency condition (4.15) becomes

$$\dot{f}(\boldsymbol{\sigma}, \eta, \nabla^2 \eta) = 0 . \tag{4.20}$$

In 1-D linear plastic strain softening, taking $\eta = \varepsilon^P$, the yield function (4.17) has the following form:

$$f(\boldsymbol{\sigma}, \eta, \nabla^2 \eta) = \sigma - \left[\sigma_Y + E_P(\varepsilon^P - c \frac{\partial^2 \varepsilon^P}{\partial x^2}) \right], \tag{4.21}$$

where ε^P is the accumulative plastic strain, E_P the plastic softening modulus, σ_Y the yield strength, and c the gradient coefficient related to the internal length scale of the material. Note that $E_P < 0$ for plastic strain softening (see Figures 4.3 and 4.4).

During plastic strain softening, the plastic strain is localized into a small region. Assuming that material in the localization zone enters the strain softening stage and the other part of the material keeps elastic, the yield condition for the localization zone reads

$$\sigma - \left[\sigma_Y + E_P(\varepsilon^P - c\frac{\partial^2 \varepsilon^P}{\partial x^2}) \right] = 0, \quad \forall : -S/2 < x \le S/2, \tag{4.22}$$

where S is the length of localization zone, which is symmetric to the origin of the coordinate axis, x (see Figure 4.3). The plastic strain distribution is controlled by differential Equation (4.22) and appropriate boundary conditions. From a physical point of view, the plastic strains at the intersection points of the plastic part and the elastic part should be zero. In the 1-D case, this condition leads to the following nonstandard boundary conditions:

$$\varepsilon^P = 0 \quad \forall : x = -S/2 \text{ and } x = +S/2, \tag{4.23}$$

which is a Dirichlet boundary condition.
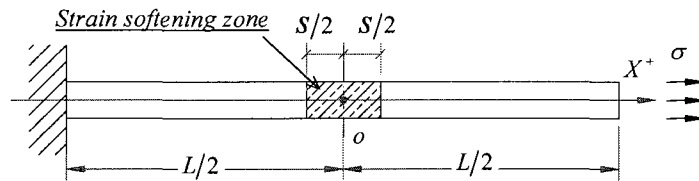
Figure 4.3 The 1-D bar with strain softening zone.
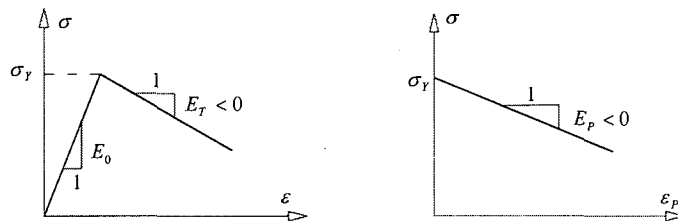
Figure 4.4 Constitutive model for linear strain softening.

Similar to gradient elasticity, the differential Equation (4.22) has two types of analytical

solutions, hyperbolic and harmonic, depending on the sign of coefficient c.

(a) *Hyperbolic solution* ($c = l^2$)

If $c = l^2$, Equation (4.22) becomes

$$\sigma - \left[\sigma_Y + E_P(\varepsilon^P - l^2 \frac{\partial^2 \varepsilon^P}{\partial x^2}) \right] = 0, \quad \forall : -S/2 < x \leq S/2. \tag{4.24}$$

The solution is of hyperbolic type:

$$\varepsilon^P(x) = \frac{\sigma_Y - \sigma}{E_P} \frac{\cosh(x/l)}{\cosh(S/2l)} - \frac{\sigma_Y - \sigma}{E_P}, \quad \forall : -S/2 < x \leq S/2. \tag{4.25}$$

(b) *Harmonic solution* ($c = -l^2$)

If $c = -l^2$, Equation (4.22) can be written as

$$\sigma - \left[\sigma_Y + E_P(\varepsilon^P + l^2 \frac{\partial^2 \varepsilon^P}{\partial x^2}) \right] = 0, \quad \forall : -S/2 < x \leq S/2, \tag{4.26}$$

The solution is of harmonic type:

$$\varepsilon^P(x) = \frac{\sigma_Y - \sigma}{E_P} \frac{\cos(x/l)}{\cos(S/2l)} - \frac{\sigma_Y - \sigma}{E_P}, \quad \forall : -S/2 < x \leq S/2. \tag{4.27}$$

To illustrate the above two solutions, the following structural and material

parameters are considered [63]: $L = 100\,mm$, $E = 20000\,N/mm^2$, $\sigma_Y = 2.0\,N/mm^2$,

$E_P = -0.1E = -2000\,N/mm^2$, $l = 5\,mm$. Given that material is in the stress state of

$\sigma = 0.5\sigma_Y = 1.0 N/mm^2$, corresponding to localization length $S = 31.4\,mm$, the plastic

strain distribution within the localization zone of the bar from the above two solutions are

plotted in Figure 4.5(a). The two functions are also plotted separately over the whole

length of the bar in Figure 4.5 (b) and (c). It can be seen that the hyperbolic distribution

of plastic strain is stable and unique within the localization zone, while the harmonic solution only has realistic distribution for $0 \leq S/2l \leq \pi$. If $S/2l > \pi$, there is a possibility that negative plastic strains will occur in the localization zone, which is inadmissible from a physical point of view. However the harmonic strain distribution results in more intense plastic strain in the strain localization zone than does the hyperbolic solution. In numerical simulations, using a harmonic function makes the plastic strain localize rapidly and stably into a narrow zone as soon as the stress reaches the bifurcation point (see de Borst [60, 63]). There have been successful applications of using harmonic functions for numerical simulation of strain localization in both one-dimensional and two-dimensional cases [63, 64]. However, the relation of the size of the localization zone (such as shear band width, necking zone, and crack band width, etc.) to the material internal length scale is still an open problem.
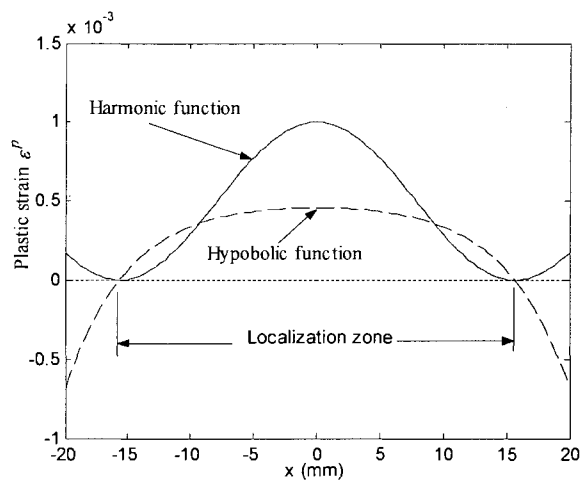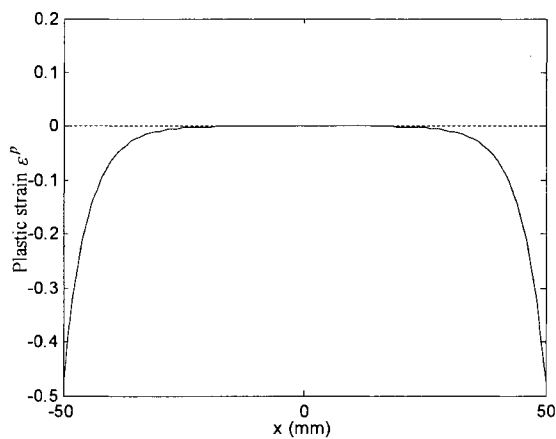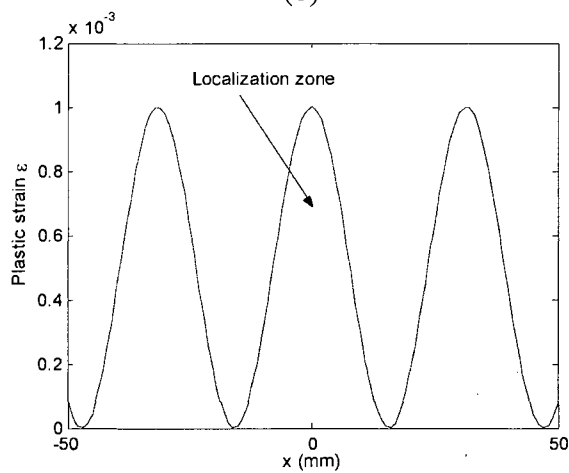
Figure 4.5 Plastic strain distribution resulting from gradient plasticity model: (a) plastic strain within localization zone; (b) hyperbolic distribution extended to whole bar; (c) harmonic distribution extended to whole bar.

4.4 **Comparison of Boundary Conditions**

The analytical solutions of the gradient elasticity model show that the standard Neumann boundary condition (4.4) removes the singularity of the elastic strain field caused by the material property jump, while the nonstandard Neumann boundary conditions (4.7) and (4.8) make the gradient effect negligible at the material points far from the singular point. In other words, the heterogeneity is smoothed by the application of Neumann boundary conditions to the higher gradient models. However, for gradient plasticity, if Neumann boundary conditions are used, the resulting plastic strains will be zero in the localization zone, which is nonrealistic. Forcing the plastic strain localized into a narrow region is equivalent to introducing heterogeneity into the strain field. Motivated from this point, the first derivative of the plastic strain field should not be specified at the boundary, and instead, the plastic strains themselves should be specified. The above analytical solutions of the strain softening problem with gradient plasticity model shows that plastic strains are surely localized into a narrow zone when the nonstandard Dirichlet boundary condition (4.23) is used, indicating that due to the Dirichlet boundary condition, the gradient plasticity model introduces heterogeneity into the strain field and makes the boundary value problem of strain localization well-posed.

4.5 **Summary**

The Neumann boundary condition is a correct one for gradient elasticity to regularize singularity of strain field, while the Dirichlet boundary condition forces the strain to be localized into a small region and removes the mesh-dependency in the modeling of strain localization and, therefore is an appropriate boundary condition for the gradient plasticity problem. Only with correct boundary conditions can these two gradient

theories regularize the nonrealistic mechanical response and make the boundary value problems well-posed. The constitutive equations with $c = l^2$ give unique and stable solutions for both gradient theories, while the gradient models with $c = -l^2$ result in unstable solutions. However, provided $0 \leq S/2l \leq \pi$, the gradient plasticity model with $c = -l^2$ can still give successful mesh-independent modeling of strain localization.

CHAPTER 5

NUMERICAL SIMULATION OF STRAIN
LOCALIZATION BASED ON NONLOCAL
PLASTICITY MODEL AND
C^0 FINITE ELEMENTS

5.1 Introduction

It is well established that the pathological, mesh-dependent solutions of strain

localization based on the classical continuum mechanics are caused by the loss of

ellipticity of the governing differential equations describing the mechanical responses of

materials with heterogenous properties [60, 65, 66]. From a mathematical point of view,

the boundary value problem becomes ill-posed when the classical continuum models are

employed to describe the inhomogenous deformation of materials in the presence of a

high strain gradient [60, 67, 68].

Various theories and models have been suggested or proposed to preserve the

ellipticity of the governing differential equations and restore the well-posedness of the

boundary value problems. These theories and models approximately fall into two

categories: the modified classical continuum model and the nonlocality-based continuum

theory. In the first category, localization is viewed as a bifurcation phenomenon, and the

bifurcation analysis is used to determine the geometry of the localized deformation modes [35, 69, 70]. The bifurcation point is found through the use of Hill's general theory of bifurcation and uniqueness for elasto-plastic solids [30]. When the onset of localization is detected, post-bifurcation behavior is modeled through setting up additional shape functions which closely reproduce the localized deformation patterns [65], smearing the deformation within a shear band over the elements that contain it [71], or assuming an enhanced strain field to reflect the strong discontinuity or displacement jumps [72-74]. Numerical analyses based on the modified classical continuum models can give objective load-displacement responses and displacement field. The drawback of this type of model is that the thickness of the shear band is still sensitive to the mesh refinement. However, the thickness of shear band in geotechnical materials, such as soils, sands, rocks, and concrete, is small as compared with the typical dimensions of geotechnical structures; for this reason the accurate prediction of shear band thickness is not important [72]. On the other hand, the shear bands observed in a variety of metals are of finite thickness, and their accurate prediction is of theoretical and practical significance [8]. The second type of theory, the nonlocality-based continuum theory, can be viewed as the generic name of a class of theory that considers the microstructure of materials (e. g. particle size, lattice arrangement, etc.), in the constitutive characterization [54, 55, 57, 75-79]. The salient feature of this type of theory is that the internal length scales of materials, which reflect the long-range cohesive forces, enter the constitutive representation of material behavior [54, 55, 76, 79-81]. Among the popular theories of this kind are Cosserat continuum theory [60, 82-85]; Toupin-Mindlin's micropolar theory

[77, 78]; Eringen-Bazănt's nonlocal theory [75, 76, 86, 87]; and high-order gradient theory [54, 55, 63, 64, 88-90].

Eringen-Bazănt's nonlocal theory takes into account the behavior of the microstructure of materials and long-range interactions between material particles by statistically averaging constitutive quantities [76, 86]. The underlying assumption of the nonlocal continuum theory is that the stress at a reference point in the body depends not only on strain history at that point but also on strain histories at all other points of the body [56, 57]. In the classical continuum mechanics, the stress at a material point depends only on the strain history at that point. Actually, this assumption of locality is too strong to reflect the microstructure behavior and is abandoned in the nonlocal continuum theory. In Eringen-Bazănt's nonlocal model, the nonlocal counterpart of a field variable at a material point, e.g. nonlocal strain, is expressed as the weighted averaging of the local variable over a spatial neighborhood of that point. When the local variable is substituted for by its truncated Taylor series, the integral-type nonlocal model reduces to the gradient-type nonlocal model whose mathematical expression has the same form as that of the high-order gradient model [80]. Both integral-type and gradient-type nonlocal models introduce internal length scales of materials in their constitutive relations. Direct application of integral-type nonlocal models to numerical analyses of strain softening were conducted by Bažant and Lin [91], and Bažant and Chang [86, 87] by way of their imbricate continuum model. The integration of nonlocality equations is approximated by finite sums over all the integration points of all the elements in the material body. With similar approach and different solution strategy, Stromberg and Ristinmaa [92] directly applied the integral-type nonlocal plasticity model to the analysis

of shear band localization. Their studies have shown that nonlocal theory can make the boundary value problem of strain softening well-posed and give mesh-independent simulation of strain localization. However, the numerical integration algorithms for incremental constitutive equations involving nonlocal quantities and stress updating schemes in these studies are much different from the regular time-step integration algorithm, and their numerical convergence and stability are not always assured. Also the physical meaning of the internal length scale and its relationship with the size of localization zone is not clearly defined.

In this chapter, a nonlocal plasticity model, which is based on the nonlocal plasticity theory, is developed to simulate the strain localization with the purpose of regularizing the mesh-dependency. A numerical analysis of the one dimensional plastic strain softening is carried out to demonstrate the ability of this model to simulate the strain localization without mesh-dependency.

5.2 Nonlocal Plasticity Model (Theory)

5.2.1 Introduction to the Nonlocal Theory and CRVE

Let x represent the position of a material point in a global reference system and ξ the position of a material point in a local reference system with its origin located at x (see Figure 5.1). For a local field, $Y(x)$, defined in domain Ω, its corresponding nonlocal counterpart, $\widetilde{Y}(x)$ (see Figure 5.2), is defined as:

$$\widetilde{Y}(x) = \frac{1}{\widetilde{V}_{RVE}(x)} \int_{\Omega_{RVE}(x)} w(x,\xi)Y(x+\xi)dV \quad \forall : x \in \Omega ; \xi \in \Omega_{RVE}(x), \tag{5.1}$$

in which

$$\widetilde{V}_{RVE}(\boldsymbol{x}) = \int_{\Omega_{RVE}(\boldsymbol{x})} w(\boldsymbol{x}, \boldsymbol{\xi}) dV \ , \tag{5.2}$$

where $\Omega_{RVE}(\boldsymbol{x})$ represents the domain occupied by a representative volumetric element (RVE) at the reference material point $\boldsymbol{x}$, $w(\boldsymbol{x}, \boldsymbol{\xi})$ is a nonlocal weighting function over $\Omega_{RVE}(\boldsymbol{x})$. The symbol "~" over a variable denotes the nonlocal counterpart of that variable. Equation (5.1) implies that a nonlocal variable is the weighted averaging of its local counterpart.
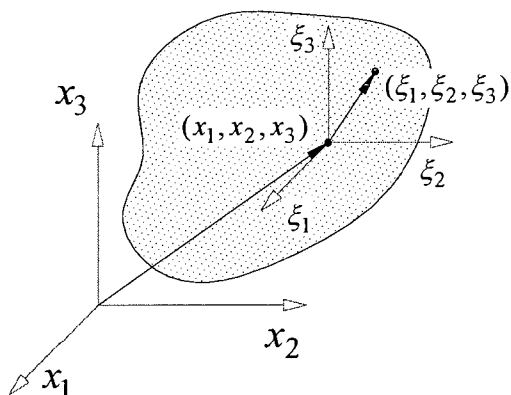
Figure 5.1 The nonlocal reference frame.
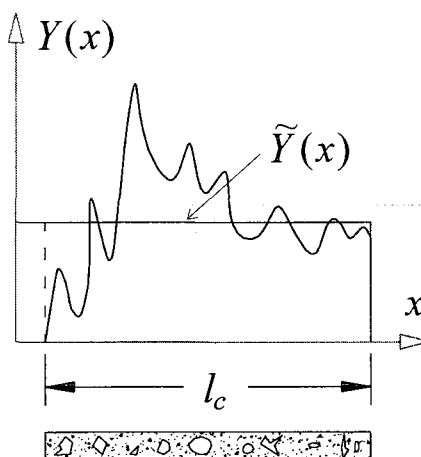
Figure 5.2 Nonlocal averaging.

The nonlocal weighting function $w(\boldsymbol{x},\boldsymbol{\xi})$ is a non-negative function and monotonically decreases with $\|\boldsymbol{\xi}\|$ increasing. At $\|\boldsymbol{\xi}\| = 0$, the $w(\boldsymbol{x},\boldsymbol{\xi})$ acquires its maximum and when $\|\boldsymbol{\xi}\| \to \infty$, $w(\boldsymbol{x},\boldsymbol{\xi}) \to 0$. The nonlocal weighting function $w(\boldsymbol{x},\boldsymbol{\xi})$ actually reflects the nonlocal interaction between two points no matter how far they are from each other. Accurate determination of $w(\boldsymbol{x},\boldsymbol{\xi})$ should rely on the analysis of atomic lattice dynamics, particle physics, or statistical mechanics. In numerical analyses, currently only semi-empirical distribution functions are adopted. According to Bažant and Lin [91], $w(\boldsymbol{x},\boldsymbol{\xi})$ could be defined as a uniformly distributed function as shown in Figure 5.3(a)

$$w(\boldsymbol{x},\boldsymbol{\xi}) = 1, \tag{5.3}$$

or a normally distributed function (Gaussian distribution function) as in Figure 5.3(b)

$$w(\boldsymbol{x},\boldsymbol{\xi}) = e^{-(k\|\boldsymbol{\xi}\|/l)^2}, \tag{5.4}$$

where k is a constant and l the characteristic length of the material that defines the size of the representative volumetric element. For the sake of simplicity, only a uniformly distributed weighting function is considered in the present study.

Consider a cubic representative volumetric element (CRVE) with side length of l_c (Figure 5.4). Suppose that the center of this CRVE is located at $\boldsymbol{x}^o = (x_1^o, x_2^o, x_3^o)$ in the global Cartesian coordinate system and serves as the origin of a local Cartesian coordinate system $\boldsymbol{\xi} = (\xi_1, \xi_2, \xi_3)$. If the field $Y(\boldsymbol{x})$ is sufficiently smooth within this CRVE, it can be expanded as the following Taylor series:

$$Y(\boldsymbol{x}^o + \boldsymbol{\xi}) = Y(\boldsymbol{x}^o) + \left(\left.\frac{\partial Y(\boldsymbol{x})}{\partial x_i}\right|_{\boldsymbol{x}=\boldsymbol{x}^o}\right)\xi_i + \frac{1}{2}\left(\left.\frac{\partial^2 Y(\boldsymbol{x})}{\partial x_i \partial x_j}\right|_{\boldsymbol{x}=\boldsymbol{x}^o}\right)\xi_i\xi_j + O\left(\xi_i\xi_j\xi_k\right), \qquad (5.5)$$

where Einstein's summation convention applies to the dummy indices.
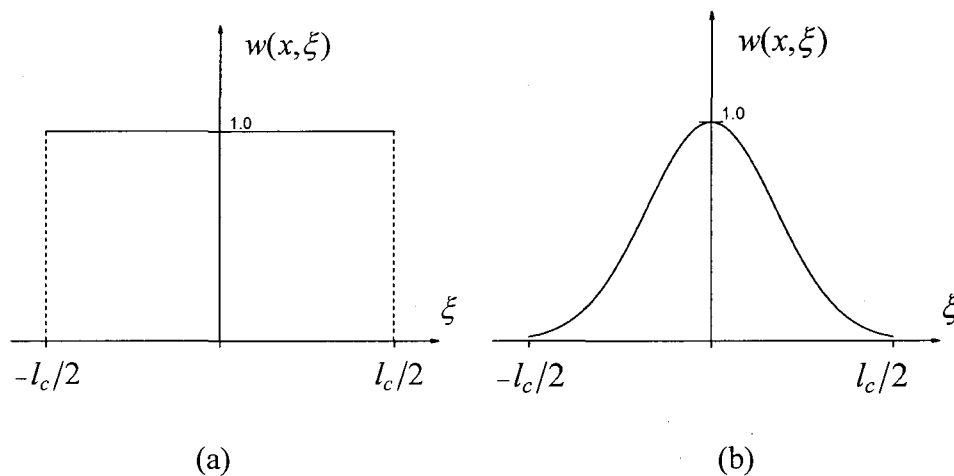
Figure 5.3 The nonlocal weighting function: (a) uniform distribution function; (b) Gaussian distribution function.
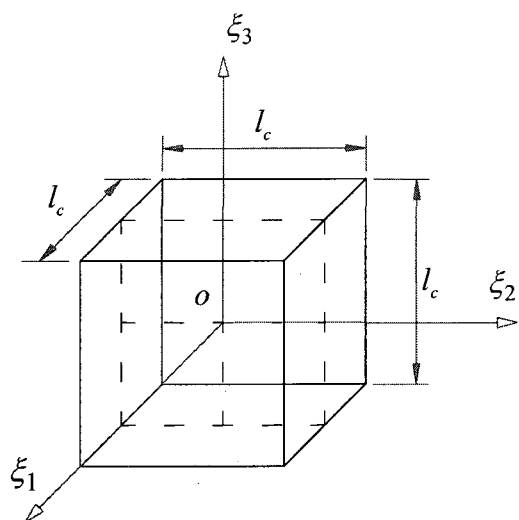
Figure 5.4 The cubic representative volumetric element (CRVE).

Generally, for every material point at $x \in \Omega$, there is a CRVE centered at x. If $Y(x)$ is smooth enough for all $x \in \Omega$, then Equation (5.5) is valid for $x \in \Omega$ and $\xi \in \Omega_{RVE}(x)$. Replacing x^o with x and substituting Equation (5.5) and (5.3) into Equation (5.1) and (5.2), with the fourth and higher order terms neglected, results in the following differential equation [80, 93]:

$$\tilde{Y}(x) = Y(x) + \frac{l_c^2}{24} \nabla^2 Y(x),$$ (5.6)

which is an approximate expression of the integral-type nonlocal model, as given by Equation (5.1).

Equation (5.6) is of the same form as the explicit gradient model except for the difference in the coefficients in front of the gradient term between Equation (5.6) and the gradient model. It is the truncated Taylor expansion, as given by Equation (5.5), which establishes a link between the nonlocal integral-type model and the gradient model, and provides an approximate approach to introduce the nonlocal effect by adding a 2nd or higher order gradient of the local field into the original local field. In the later section we will show that this link makes it possible to use C^0 elements to solve the nonlocal field.

The dimension length l_c, defined as the side length of a CRVE, and often called the characteristic length of the CRVE, enters into Equation (5.6). In the literature of nonlocal or gradient theory [55, 57, 68, 93, 94], an internal length scale c is usually defined through

$$\tilde{Y}(x) = Y(x) + c^2 \nabla^2 Y(x).$$ (5.6a)

Comparing Equation (5.6) with Equation (5.6a), one can obtain

$$c = \frac{l_c}{\sqrt{24}} . \qquad (5.6b)$$

The implication of this definition is that the nonlocal interaction between the reference point at the center of the CRVE and the material points outside the CRVE are not considered. This definition is based on the assumption that the nonlocal interaction between two material points will become negligible when their physical distance exceeds a characteristic length. As a consequence, a link between the size of the localization zone or shear band width and the CRVE is well established. It will be shown in the later section that the size of the localization zone is equal to the characteristic length of the CRVE.

5.2.2 The Nonlocal Plasticity

Recall Equations (2.3) through (2.5). In the classical theory of plasticity, the yield function in the stress space at a material point generally depends on the local stress state and the local internal state variables at that material point [41-42]. All of the quantities in Equations (2.3) through (2.5) are local quantities. In the presence of strain softening plasticity, the boundary value problem (BVP) with all local quantities involved in the yield function becomes ill-posed. To regularize the ill-posedness, some local variables have to be replaced with their nonlocal counterparts. In Eringen's nonlocal plasticity theory, the elastic stresses or total strains are nonlocal, and the resulting formulation cannot be used as a localization limiter [76]. Bažant and Chang [86], Vardoulakis and Aifantis [94], de Borst and Mühlhaus [63], and other researchers [88, 89, 95] treat the internal state variable or plastic strains as nonlocal quantities and give mesh-independent modeling of strain localization. In the present study, only nonlocality of the internal state variable and plastic strains are considered in our nonlocal plasticity model.

Substituting the nonlocal internal variable $\tilde{\eta}$ for the local variable η in Equations (2.3) and (2.4) gives the following nonlocal yield function and yield stress:

$$f(\boldsymbol{\sigma}, \tilde{\eta}) := \mathscr{F}(\boldsymbol{\sigma}) - \sigma_Y(\tilde{\eta}) = 0, \tag{5.7}$$

$$\sigma_Y(\tilde{\eta}) = \sigma_{Y0} + \chi(\tilde{\eta}). \tag{5.8}$$

If the differential Equation (5.6) is adopted as the approximate relation between $\tilde{\eta}$ and η, i.e.

$$\tilde{\eta}(\boldsymbol{x}) = \eta(\boldsymbol{x}) + \frac{l_c^2}{24}\nabla^2\eta(\boldsymbol{x}), \tag{5.9}$$

the nonlocal yield function and the yield stress will take the form of a 2nd order differential equation in the local internal variable η:

$$f(\boldsymbol{\sigma}, \eta + \frac{l_c^2}{24}\nabla^2\eta) := \mathscr{F}(\boldsymbol{\sigma}) - \sigma_Y(\eta + \frac{l_c^2}{24}\nabla^2\eta) = 0, \tag{5.7a}$$

$$\sigma_Y(\eta + \frac{l_c^2}{24}\nabla^2\eta) = \sigma_{Y0} + \chi(\eta + \frac{l_c^2}{24}\nabla^2\eta). \tag{5.8a}$$

The advantage of Equation (5.7a) and Equation (5.8a) over Equation (5.7) and Equation (5.8) is that we can derive the weak form of Equations (5.7a) and (5.8a) and use C^0 finite elements to obtain the solution of the local field η. After obtaining η, Equation (5.1) can be used to solve the nonlocal field $\tilde{\eta}$, and then $\tilde{\eta}$ is substituted into Equation (5.7) and Equation (5.8) to check if the yield condition is satisfied. With this methodology, we can avoid employing C^1 elements to evaluate the Laplacian term $\nabla^2\eta$.

5.3 Finite Element Formulation of the Two Coupled Fields

5.3.1 The Governing Differential Equations

Suppose that at a given instant of time t, a domain Ω is in a state of static equilibrium, and the state of stress $\boldsymbol{\sigma}$ and its loading history is known throughout the domain. The external force increment $d\hat{\boldsymbol{F}}$ is prescribed on $\partial_g\Omega$, and the displacement $d\hat{\boldsymbol{u}}$ is prescribed on $\partial_u\Omega$, where ∂_g and ∂_u denote the boundary associated with the given force and displacement (Figure 5.5). The boundary value problem of incremental elastoplasticity is to find the incremental displacement field $d\boldsymbol{u}$ that satisfies, in Ω,

the equation of equilibrium

$$\operatorname{div} d\boldsymbol{\sigma} + d\boldsymbol{b} = 0, \tag{5.9}$$

the strain--displacement relation

$$d\boldsymbol{\varepsilon} = \frac{1}{2}\left(\nabla d\boldsymbol{u} + \left(\nabla d\boldsymbol{u}\right)^T\right), \tag{5.10}$$

the constitutive relation

$$d\boldsymbol{\sigma} = \boldsymbol{C}^e : \left(d\boldsymbol{\varepsilon} - d\boldsymbol{\varepsilon}^p\right), \tag{5.11}$$

and *the boundary condition*

$$d\boldsymbol{\sigma} \cdot \boldsymbol{n} = d\hat{\boldsymbol{F}} \quad \text{on } \partial_g\Omega \quad \text{and} \tag{5.12}$$

$$d\boldsymbol{u} = d\hat{\boldsymbol{u}} \quad \text{on } \partial_u\Omega, \tag{5.13}$$

where $\partial_g\Omega \bigcup \partial_u\Omega = \partial\Omega$, $\partial_g\Omega \bigcap \partial_u\Omega = \emptyset$. The domain Ω can be divided into an elastoplastic domain Ω_{ep} and an elastic domain Ω_e, i.e. $\Omega = \Omega_{ep} \bigcup \Omega_e$. In the elastic domain Ω_e, we have $d\varepsilon^p = 0$. In the elastoplastic domain Ω_{ep}, when the material experiences unloading, we have $d\varepsilon^p = 0$. If it experiences plastic loading, we have

$d\varepsilon^p > 0$. If the plastic loading obeys the associative normal flow rule, the plastic strains relate to stresses by

$$d\boldsymbol{\varepsilon}^p = d\lambda \frac{\partial f}{\partial \boldsymbol{\sigma}}.$$ (5.14)

The plastic loading/unloading condition obeys the following Kuhn-Tucker complementarity condition [42, 43]

$$d\lambda \geq 0 \ , \ f(\boldsymbol{\sigma},\widetilde{\eta}) \leq 0, \ \text{and} \ d\lambda f(\boldsymbol{\sigma},\widetilde{\eta}) = 0,$$ (5.15)

and satisfies the consistency requirement

$$d\lambda \dot{f}(\boldsymbol{\sigma},\widetilde{\eta}) = 0.$$ (5.16)

During plastic loading, $d\lambda \geq 0$, Equation (5.15) and Equation (5.16) turn out to be

$$f(\boldsymbol{\sigma},\widetilde{\eta}) = 0 \quad \text{in } \Omega_{ep},$$ (5.17)

$$\dot{f}(\boldsymbol{\sigma},\widetilde{\eta}) = 0 \quad \text{in } \Omega_{ep}.$$ (5.18)
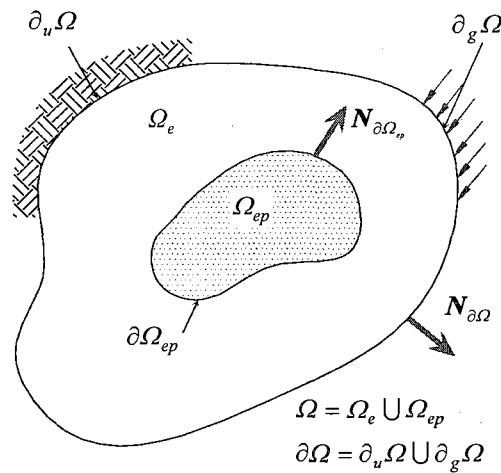
Figure 5.5 Domain of two coupled elasto-plastic boundary-value problems.

Using the chain rule and nonlocal relation Equation (5.6a), Equation (5.7), and Equation (5.9), the consistency Equation (5.18) can be rewritten as

$$\frac{\partial f}{\partial \boldsymbol{\sigma}} : d\boldsymbol{\sigma} - \frac{\partial \sigma_Y(\tilde{\eta})}{\partial \tilde{\eta}}\left(d\eta + c^2 \nabla^2 d\eta\right) = 0,\tag{5.19}$$

If the plastic modulus E_p is defined as

$$E_p = \frac{\partial \sigma_Y(\tilde{\eta})}{\partial \tilde{\eta}} = \frac{\partial \sigma_Y(\eta)}{\partial \eta},\tag{5.20}$$

and the tensor $\boldsymbol{a}$, which is related to the normal direction of the yield surface, is written as

$$\boldsymbol{a} = \frac{\partial f}{\partial \boldsymbol{\sigma}}.\tag{5.21}$$

Equation (5.18) becomes

$$\boldsymbol{a} : d\boldsymbol{\sigma} - E_p d\eta - E_p c^2 \nabla^2 d\eta = 0.\tag{5.22}$$

Letting

$$k = E_p c^2,\tag{5.23}$$

and substituting k into Equation (5.22), we obtain

$$\boldsymbol{a} : d\boldsymbol{\sigma} - E_p d\eta - k \nabla^2 d\eta = 0.\tag{5.24}$$

Equation (5.24) is a 2nd-order differential equation with respect to the internal variable η and only valid under the following condition

$$\boldsymbol{x} \in \Omega_{ep} \text{ and } \eta > 0 \text{ (i.e. plastic loading),}\tag{5.25}$$

To solve Equation (5.24), the boundary conditions related to $\eta(x)$ have to be prescribed on $\partial\Omega_{ep}$. According to the results obtained in Chapter 4, Dirichlet boundary conditions should be applied on $\partial\Omega_{ep}$, that is

$$d\eta = 0 \quad \text{on} \quad \partial\Omega_{ep}. \tag{5.26}$$

The boundary value problem of the field $d\eta(x)$ is to find the internal variable $\eta(x)$ in domain Ω_{ep} that satisfies Equation (5.24), Equation (5.25), and the boundary condition of Equation (5.26). The internal variable η can be related to the equivalent plastic strain, ε_{eq}^{p}, through

$$d\eta = d\varepsilon_{eq}^{p}. \tag{5.27}$$

With associative flow rule (5.14) and the assumption of isotropic strain hardening/softening, for many yield functions the relation between $d\eta$ and $d\lambda$ has the following linear form [63, 95]:

$$d\eta = \gamma d\lambda. \tag{5.28}$$

For the von Mises yield function, one can derive (see Appendix A)

$$\gamma = 1, \quad d\eta = d\lambda. \tag{5.29}$$

For other yield functions, γ can be formulated by substituting the specific yield function into Equation (5.14), and then Equation (2.7), and finally Equation (5.27). Our research effort will be only focused on the von Mises yield function. Substitution of Equation (5.29) into Equation (5.24) results in

$$\boldsymbol{a} : d\boldsymbol{\sigma} - E_{p}d\lambda - k\nabla^{2}d\lambda = 0. \tag{5.30}$$

We can see that the two fields, the displacement field u and the plastic multiplier field λ (or the internal variable field η) are coupled with each other. These two fields involve two sets of coupled 2nd order partial differential equations and independent boundary conditions, which are summarized as follows:

$$\boxed{\begin{aligned} &\textit{Displacement field}: \qquad \operatorname{div} d\sigma + db = 0 \quad \forall : x \in \Omega \\ &\textit{Plastic multiplier field}: a : d\sigma - E_p d\lambda - k\nabla^2 d\lambda = 0, \quad \forall : x \in \Omega_{ep} \ \& \ d\lambda > 0 \end{aligned}} \tag{5.31}$$

Notice that the governing equations for the displacement field hold for the whole problem domain Ω, while the governing equations for the plastic multiplier field are only valid in the elasto-plastic domain Ω_{ep} under the condition of $d\lambda > 0$. This situation brings some complexities in the design of solution algorithms for the nonlinear system of equations resulting from finite element discretization.

5.3.2 Variational Formulation of Two Coupled Field Equations

Following Mühlhaus and Aifantis [58] and de Borst and Mühlhaus [63], we derive the weak forms of the differential field Equation (5.31) as follows.

For the displacement field du, the weak form of the Equation (5.9) is the same as derived in Chapter 2, which is rewritten in the following

$$\int_{\Omega} \delta\varepsilon : d\sigma \, dV = \int_{\Omega} db \cdot \delta u \, dV + \int_{\partial\Omega_g} d\hat{F} \cdot \delta u \, dS. \tag{5.32}$$

Substitution of Equations (5.10), (5.11), (5.14), (5.21) into the above equation results in

$$\int_{\Omega} \delta\varepsilon : C : (d\varepsilon - d\lambda a) dV = \int_{\Omega} db \cdot \delta u \, dV + \int_{\partial\Omega_g} d\hat{F} \cdot \delta u \, dS. \tag{5.33}$$

The variational statement of the boundary value problem for the displacement field is to find du such that

$$\int_{\Omega} \delta d\varepsilon : C : (d\varepsilon - d\lambda a)dV = \int_{\Omega} db \cdot \delta du dV + \int_{\partial\Omega_g} d\hat{F} \cdot \delta du dS \Bigg\}$$

$$du = d\hat{u} \qquad \text{on } \partial_u \Omega$$

(5.34)

For the plastic multiplier, we can write the variational form of the field Equation (5.30) as

$$\int_{\Omega_{ep}} \delta d\lambda (a : d\sigma - E_p d\lambda - k\nabla^2 d\lambda) = 0,$$

(5.35)

where $\delta d\lambda$ is the variation of the solution $d\lambda$. To make the derivation convenient, we take the alternative form of Equation (5.35)

$$\int_{\Omega_{ep}} (\delta d\lambda a : d\sigma - E_p \delta d\lambda d\lambda - k\delta d\lambda \nabla^2 d\lambda) = 0.$$

(5.36)

Integrating the third term of Equation (5.36) by parts yields

$$\int_{\Omega_{ep}} \delta d\lambda (\nabla^2 d\lambda)dV = \int_{\Omega_{ep}} \nabla \cdot (\delta d\lambda (\nabla d\lambda))dV - \int_{\Omega_{ep}} \nabla(\delta d\lambda) \cdot (\nabla d\lambda)dV.$$

(5.37)

Applying the divergence theorem

$$\int_{\Omega_{ep}} \nabla \cdot (\delta d\lambda (\nabla d\lambda))dV = \int_{\partial\Omega_{ep}} \delta d\lambda (\nabla d\lambda) \cdot \mathbf{n} dV,$$

(5.38)

to the first term of right hand side of Equation (5.37) and considering the nonstandard boundary condition (5.26) and Equation (5.29), we arrive at

$$\int_{\Omega_{ep}} \delta d\lambda (\nabla^2 d\lambda)dV = - \int_{\Omega_{ep}} \nabla(\delta d\lambda) \cdot (\nabla d\lambda) dS.$$

(5.39)

Substitution of Equation (5.39) into Equation (5.36) results in the weak form of the governing equation of the plastic multiplier field as

$$\int_{\Omega_{ep}} (\delta d\lambda a : d\sigma - E_p \delta d\lambda d\lambda + k\nabla(\delta d\lambda) \cdot \nabla d\lambda)dV = 0.$$

(5.40)

The variational statement of the boundary value problem for the plastic multiplier field is

to find $d\lambda$ such that

$$
\left.
\begin{aligned}
&\int_{\Omega_{ep}}\left(\delta d\lambda\, \boldsymbol{a} : d\boldsymbol{\sigma} - E_p \delta d\lambda\, d\lambda + k\nabla(\delta d\lambda)\cdot\nabla d\lambda\right)dV = 0 \\
&d\lambda = 0 \;\; \text{on}\;\; \partial\Omega_{ep},\&\;\; d\lambda > 0,\;\; \forall\, \boldsymbol{x} \in \Omega_{ep}
\end{aligned}
\right\}.
\tag{5.41}
$$

Observe that $d\lambda$ is unknown for Equation (5.34), and $d\boldsymbol{\sigma}$ is unknown for

Equation (5.41). Thus $d\boldsymbol{u}$ can not be found by only solving Equation (5.34) and $d\lambda$ can

not be found by only solving Equation (5.41). To find the solutions of $d\boldsymbol{u}$ and $d\lambda$, we

have to solve the two field equations simultaneously. The variational statement of these

two coupled field equations should be defined as: to find $d\boldsymbol{u}$ and $d\lambda$ such that Equation

(5.34) and Equation (5.41) are satisfied simultaneously. We summarize the weak form of

these two coupled field equations in the following box

$$
\left.
\boxed{
\begin{aligned}
&\left.
\begin{aligned}
&\int_{\Omega}\delta d\boldsymbol{\varepsilon} : \boldsymbol{C} : (d\boldsymbol{\varepsilon} - d\lambda \boldsymbol{a})dV = \int_{\Omega} d\boldsymbol{b}\cdot\delta d\boldsymbol{u}\,dV + \int_{\partial\Omega_g} d\hat{\boldsymbol{F}}\cdot\delta d\boldsymbol{u}\,dS \\
&d\boldsymbol{u} = d\hat{\boldsymbol{u}} \qquad \text{on}\;\; \partial_u\Omega
\end{aligned}
\right\} \;\forall : \boldsymbol{x}\in\Omega \\
&\left.
\begin{aligned}
&\int_{\Omega_{ep}}\left(\delta d\lambda\, \boldsymbol{a} : d\boldsymbol{\sigma} - E_p \delta d\lambda\, d\lambda + k\nabla(\delta d\lambda)\cdot\nabla d\lambda\right)dV = 0 \\
&d\lambda = 0 \;\; \text{on}\;\; \partial\Omega_{ep},\&\;\; d\lambda > 0,\;\; \forall\, \boldsymbol{x}\in\Omega_{ep}
\end{aligned}
\right\} \;\forall : \boldsymbol{x}\in\Omega_{ep}
\end{aligned}
}
\right.
\tag{5.42}
$$

5.3.3 Galerkin's Formulation

Following the procedure in Section 2.5 of Chapter 2, let us discretize the domain

Ω into the element domain $\Omega^e, 1 \le e \le n_{el}$, where n_{el} is the total number of elements.

The displacement field $d\boldsymbol{u}$ within Ω^e can be approximated by Equation (2.53), and the

strain-displacement relations can be expressed in matrix form as Equation (2.54). For the

same element domain Ω^e, if $\Omega^e \subseteq \Omega_{ep}$ and $d\lambda > 0$, the plastic multiplier field $d\lambda$ can

be approximated by

$$\{d\lambda\} = \lfloor \boldsymbol{\Phi} \rfloor \{d\lambda_\lambda^e\}, \tag{5.42}$$

where $\lfloor \boldsymbol{\Phi} \rfloor$ is the shape function of $\{d\lambda\}$, defined as

$$\lfloor \boldsymbol{\Phi} \rfloor = \lfloor \Phi_1 \quad \Phi_2 \cdots \cdots \Phi_{n_{en}} \rfloor. \tag{5.43}$$

The gradient of $\{d\lambda\}$ is written as

$$\nabla\{d\lambda\} = [\nabla\boldsymbol{\Phi}]\{d\lambda_\lambda^e\} = [\boldsymbol{\Psi}]\{d\lambda_\lambda^e\}, \tag{5.44}$$

where

$$[\boldsymbol{\Psi}] = [\nabla\boldsymbol{\Phi}] = [\nabla\Phi_1 \ \nabla\Phi_2 \ \cdots \ \nabla\Phi_{n_{en}}] = \begin{bmatrix} \Phi_{1,1} & \Phi_{2,1} & \cdots \cdots & \Phi_{n_{en},1} \\ \Phi_{1,2} & \Phi_{2,2} & \cdots \cdots & \Phi_{n_{en},2} \end{bmatrix}, \text{ for } n_{sd} = 2, \tag{5.45}$$

$$[\boldsymbol{\Psi}] = [\nabla\boldsymbol{\Phi}] = [\nabla\Phi_1 \ \nabla\Phi_2 \ \cdots \ \nabla\Phi_{n_{en}}] = \begin{bmatrix} \Phi_{1,1} & \Phi_{2,1} & \cdots \cdots & \Phi_{n_{en},1} \\ \Phi_{1,2} & \Phi_{2,2} & \cdots \cdots & \Phi_{n_{en},2} \\ \Phi_{1,3} & \Phi_{2,3} & \cdots \cdots & \Phi_{n_{en},3} \end{bmatrix}, \text{ for } n_{sd} = 3, \tag{5.46}$$

Substituting Equation (2.53), Equation (2.54) and Equation (5.42)-(5.46) into Equations (5.34) and (5.41) yields

$$\{\delta u_h^e\}^T \int_{\Omega^e} [B]^T [C] ([B]\{du_h^e\} - \lfloor \boldsymbol{\Phi} \rfloor \{d\lambda_h^e\}\{a\}) dV = \{\delta u_h^e\}^T \left(\int_{\Omega^e} [N]^T \{db\} dV + \int_{\partial\Omega_g^e} [N]^T \{d\hat{F}\} dS \right),$$

$$\tag{5.47}$$

$$\{\delta d\lambda_h^e\}^T \int_{\Omega_{ep}^e} (\lfloor \boldsymbol{\Phi} \rfloor^T \{a\}^T [C] ([B]\{du_h^e\} - \{a\}\lfloor \boldsymbol{\Phi} \rfloor\{d\lambda_h^e\}) - E_p \lfloor \boldsymbol{\Phi} \rfloor^T \lfloor \boldsymbol{\Phi} \rfloor\{d\lambda_h^e\} + k[\boldsymbol{\Psi}]^T [\boldsymbol{\Psi}]\{d\lambda_h^e\}) dV = 0.$$

$$\tag{5.48}$$

Because Galerkin's Equations (5.47) and (5.48) hold for arbitrary $\{\delta u_h^e\}$ and $\{\delta d\lambda_h^e\}$, it

follows that

$$\int_{\Omega^e}[B]^T[C]\big([B]\{du_h^e\}-\{a\}\lfloor\Phi\rfloor\{d\lambda_h^e\}\big)dV = \int_{\Omega^e}[N]^T\{db\}dV + \int_{\partial\Omega_g^e}[N]^T\{d\hat{F}\}dS, \qquad (5.49)$$

$$\int_{\Omega_{ep}^e}\big(\lfloor\Phi\rfloor^T\{a\}^T[C][B]\{du_h\}-\big(\lfloor\Phi\rfloor^T\{a\}^T[C]\{a\}\lfloor\Phi\rfloor+E_p\lfloor\Phi\rfloor^T\lfloor\Phi\rfloor-k[\Psi]^T[\Psi]\big)\{d\lambda_h\}\big)dV = 0.$$

$$(5.50)$$

After rearranging the terms in Equation (5.49) and Equation (5.50), we obtain the following concise form

$$\begin{bmatrix} K_{uu}^e & K_{u\lambda}^e \\ \big(K_{u\lambda}^e\big)^T & K_{\lambda\lambda} \end{bmatrix}\begin{Bmatrix} du_h^e \\ d\lambda_h^e \end{Bmatrix} = \begin{Bmatrix} d\hat{F}_h^e \\ 0 \end{Bmatrix}, \qquad (5.51)$$

where

$$[K_{uu}^e] = \int_{\Omega^e}[B]^T[C][B]dV, \qquad (5.52)$$

$$[K_{u\lambda}^e] = -\int_{\Omega_{ep}^e}[B]^T[C]\{a\}\lfloor\Phi\rfloor dV, \qquad (5.53)$$

$$[K_{\lambda\lambda}^e] = \int_{\Omega_{ep}^e}\big(\lfloor\Phi\rfloor^T\{a\}^T[C]\{a\}\lfloor\Phi\rfloor+E_p\lfloor\Phi\rfloor^T\lfloor\Phi\rfloor-k[\Psi]^T[\Psi]\big)dV, \qquad (5.54)$$

$$\{d\hat{F}_h^e\} = \int_{\Omega^e}[N]^T\{db\}dV + \int_{\partial\Omega_g^e}[N]^T\{d\hat{F}\}dS. \qquad (5.55)$$

In Equation (5.54), E_p and k have the following properties:

$$\begin{vmatrix} E_p > 0, k > 0 & \text{for strain hardening} \\ E_p = 0, k = 0 & \text{for perfect plascity} \\ E_p < 0, k < 0 & \text{for strain softening} \end{vmatrix}. \qquad (5.56)$$

Equation (5.51) can be written in a more concise form as

$$[K^e]\{d\mathcal{U}_h^e\} = \{d\hat{\mathcal{F}}_h^e\}, \qquad (5.57)$$

with

$$[\boldsymbol{K}^e] = \begin{bmatrix} \boldsymbol{K}^e_{uu} & \boldsymbol{K}^e_{u\lambda} \\ \left(\boldsymbol{K}^e_{u\lambda}\right)^T & \boldsymbol{K}_{\lambda\lambda} \end{bmatrix}, \tag{5.58}$$

$$\{d\boldsymbol{\mathcal{U}}^e_h\} = \begin{Bmatrix} d\boldsymbol{u}^e_h \\ d\lambda^e_h \end{Bmatrix}, \quad \{d\hat{\boldsymbol{\mathcal{F}}}^e_h\} = \begin{Bmatrix} d\hat{\boldsymbol{F}}^e_h \\ \boldsymbol{0} \end{Bmatrix}. \tag{5.59}$$

Notice that the element stiffness matrix $[\boldsymbol{K}^e]$ is symmetric when the associative

flow rule is applied. This property makes it possible to take advantage of the existing

symmetric equation solvers to save program coding work. Also we notice that C^0

continuity is enough to find the solution of $\{d\boldsymbol{u}\}$ and $\{d\lambda\}$ in the finite element context.

5.4 Solution Strategy of the Two Groups of Nonlinear Equations

5.4.1 General Methodology

In Section 2.6 of Chapter 2, we have shown that for the incremental-iterative

solution process, the linearized equilibrium equations for $(k+1)^{th}$ iteration become

$$\int_{\Omega^e} [\boldsymbol{B}]^T [\Delta\boldsymbol{\sigma}] dV = \{\Delta\hat{\boldsymbol{F}}^e_h\} + \{\Delta\hat{\boldsymbol{F}}^e_h\}^{unb}_k. \tag{5.60}$$

Following similar methodology as in Section 2.6, we can show that the linearized

Galerkin's equations (5.51) for the two coupled fields become

$$\begin{bmatrix} \boldsymbol{K}^e_{uu} & \boldsymbol{K}^e_{u\lambda} \\ \left(\boldsymbol{K}^e_{u\lambda}\right)^T & \boldsymbol{K}_{\lambda\lambda} \end{bmatrix} \begin{Bmatrix} \Delta\boldsymbol{u}^e_h \\ \Delta\lambda^e_h \end{Bmatrix} = \begin{Bmatrix} \Delta\hat{\boldsymbol{F}}^e_h + (\Delta\hat{\boldsymbol{F}}^e_h)^{unb}_k \\ \boldsymbol{0} \end{Bmatrix}, \tag{5.61}$$

where,

$$\{\Delta\hat{\boldsymbol{F}}^e_h\} = \int_{\Omega^e} [\boldsymbol{N}]^T \{\Delta\boldsymbol{b}\} dV + \int_{\partial\Omega^e_g} [\boldsymbol{N}]^T \{\Delta\hat{\boldsymbol{F}}\} dS, \tag{5.62}$$

$$\left\{ \varDelta \hat{F}_h^e \right\}_k^{unb} = \int\limits_{\Omega^e} [N]^T \{b\}_k \, dV + \int\limits_{\partial\Omega_g^e} [N]^T \{\hat{F}\}_k \, dS - \int\limits_{\Omega^e} [B]^T [\sigma]_k \, dV = \{\hat{F}_h^e\}_k - \int\limits_{\Omega^e} [B]^T [\sigma]_k \, dV .$$

$$(5.63)$$

Equations (5.61)-(5.63) are based on the assumption that $[\sigma]$ and $\{\hat{F}\}$ are linearly additive, i.e

$$[\sigma]_{k+1} = [\sigma]_k + [\varDelta\sigma],$$ $$(5.64)$$

$$\{\hat{F}\}_{k+1} = \{\hat{F}\}_k + \{\varDelta\hat{F}\}.$$ $$(5.65)$$

Solutions of displacements and plastic multipliers at the $(k+1)^{th}$ iteration can be obtained by

$$\left\{ \begin{matrix} u_h^e \\ \lambda_h^e \end{matrix} \right\}_{k+1} = \left\{ \begin{matrix} u_h^e \\ \lambda_h^e \end{matrix} \right\}_k + \left\{ \begin{matrix} \varDelta u_h^e \\ \varDelta\lambda_h^e \end{matrix} \right\}.$$ $$(5.66)$$

It should be noticed that the yield condition (5.17) is not exactly satisfied at each iteration but only the consistency condition (5.18) is satisfied. However, in the governing equation for the plastic flow, only linear terms of the Taylor expansion of the yield function are considered, and the higher order terms are truncated, which means that Equation (5.17) will not generally be satisfied at any stage of computation. Because the elasto-plastic problems are driven by the displacement field, and also u and λ are coupled with each other, we can not adjust $\{\lambda_h^e\}$ in a similar way as we do with $\{u_h^e\}$. Instead, we need to construct an alternative algorithm to adjust $\{\lambda_h^e\}$ to force the λ to satisfy the yield condition and then compute the unbalanced nodal forces to reflect this adjustment in the equilibrium equations. This algorithm will be described in the following section.

5.4.2 The Moving Boundary Technique and Nonlocal Element

The governing equations of the two coupled fields, $\{u\}$ and $\{\lambda\}$, consist of two parts: one is the equilibrium equation and the other the yield condition. These two sets of governing equations are associated with one another through the flow rule and consistency condition. Therefore, there is no doubt that the linearized Galerkin's equation (5.61) is valid only for the domain where the material has entered the plastic stage and is under plastic loading. For the same domain, the yield condition is not involved in the governing equations in the following three cases: elastic loading and unloading, unloading from the plastic stage, and reloading before reaching the new yield surface. In these three cases, the yield condition will not be satisfied, and it will not enter the finite element formulation. On the other hand, for the same structures under loading, some parts of it may be in the elastic stage whereas the other parts are experiencing plastic flow. This situation still results in the exclusion of the yield conditions from the governing equations for some elements. In the present research, we use the moving boundary technique and nonlocal element to realize the exclusion and inclusion of yield condition in the Galerkin's equation by means of adjusting the degrees of freedom (DOFs) of the plastic multiplier field, $\{\lambda\}$.

Recall the definition of the cubic representative volumetric element (CRVE) in Section 5.2.1. For the 2-D cases, if domain Ω has unit thickness, the CRVE reduces to a square RVE (SRVE) with a side length of l_c (Figure 5.6(a)). In the same way, for the one dimensional cases, a SRVE further reduces to a bar of length l_c with a cross-section area of A_c, which is called a line RVE or LRVE (Figure 5.6(b)). For a discretized 2-D domain

Ω, a SRVE is composed of all the elements inside a square region *ABCD*. All these elements inside this square region are called the *nonlocal elements* attached to the *local element*, $e_i^{(0)}$, which is located in the center of the region. In other words, every finite element itself is not only a local element, but also has a set of adjacent finite elements attached to it. These adjacent elements that attach to a certain local element are called nonlocal elements whose *host element* is the local element located in the center of the RVE. In Figure 5.6(a), element $e_i^{(j)}$, $j = 0, 1, \cdots, 8$, constitutes a set of 2-D nonlocal elements whose host element is a 2-D element $e_i^{(0)}$. In Figure 5.6(b), elements $e_i^{(j)}$, $j = 0, 1, \cdots, 4$, constitutes a set of 1-D nonlocal elements whose host element is a 1-D element $e_i^{(0)}$. Notice that a host element itself serves as one of its nonlocal elements.

According to the above definition, a local element is both a host element and a nonlocal element attached to some other host elements. Consequently the nonlocal elements for some host elements are overlapped within the discretized domain. For example, in Figure 5.7, the nonlocal elements of the host elements e_5, e_{10}, and e_{18} are overlapped (Table 5.1).

The purpose of defining a set of nonlocal elements for a host element is to evaluate the nonlocal constitutive quantities of a local element. In the current study, the only nonlocal constitutive quantity is the equivalent plastic strain or plastic multiplier, λ. If at the kth iteration of the nth load step, the stress state at some Gaussian integration point, say, GP_i, in the local element e_i meets the yield condition, the whole element e_i is thought as to be in yielding and all of the DOFs at its nodal points for λ, are activated, that is,

$$\lambda_{h_j}^{e_i} \neq 0 \quad, \; j = 1, 2, \ldots, n_e \; , \tag{5.67}$$

where $\lambda_{h_j}^{e_i}$ represents the values of λ at nodal points of element e_i, h_j is the global node

number, n_e is the total number of nodal points in element e_i, and j represents the local

node number, for example, $j = 1, 2, \cdots, 8.$, for an 8-noded isoparametric element. In this

way, the yield condition (5.17), enters the governing equations. On the contrary, if any

Gaussian integration points are in an elastic or unloading stage from the yield surface or

reloading but not reaching the new yield surface, the DOFs of its all nodal points for λ,

will be inactive, that is,

$$\lambda_{h_j}^{e_i} = 0 \quad, \; j = 1, 2, \ldots, n_e. \tag{5.68}$$

As a result, the yield condition will quit the governing equations. By making the DOFs of

element nodal points for λ active or inactive, the yield condition is controlled to come

into or quit from playing in the governing equations. This approach is actually equivalent

to moving the elasto-plastic boundary according to the stress state of local elements

(Figure 5.7).
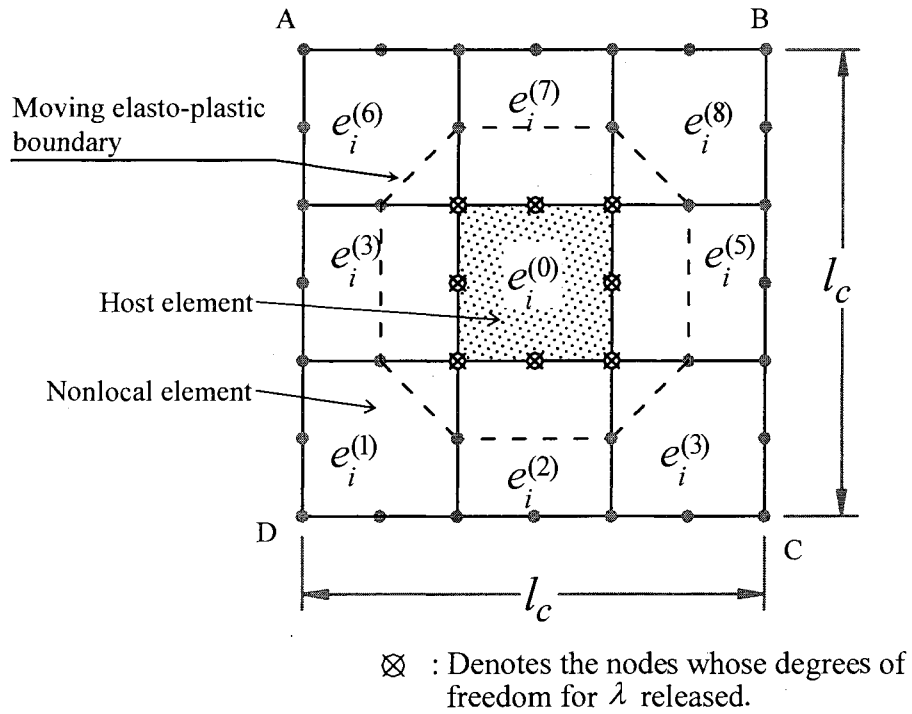
(a)
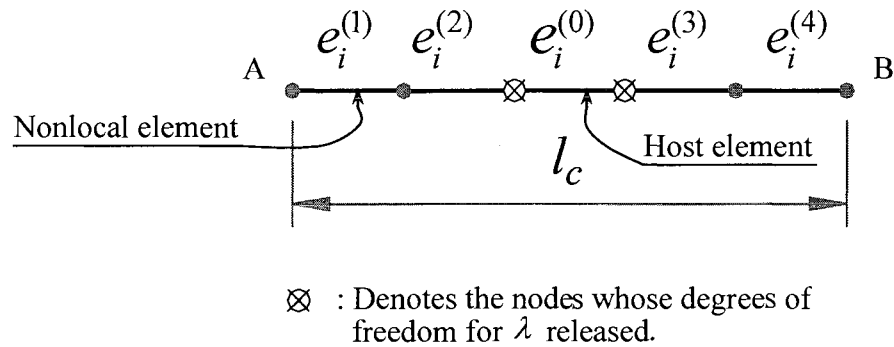
(b)

Figure 5.6. The moving elasto-plastic boundary and nonlocal elements: (a) 2-D; (b) 1-D.
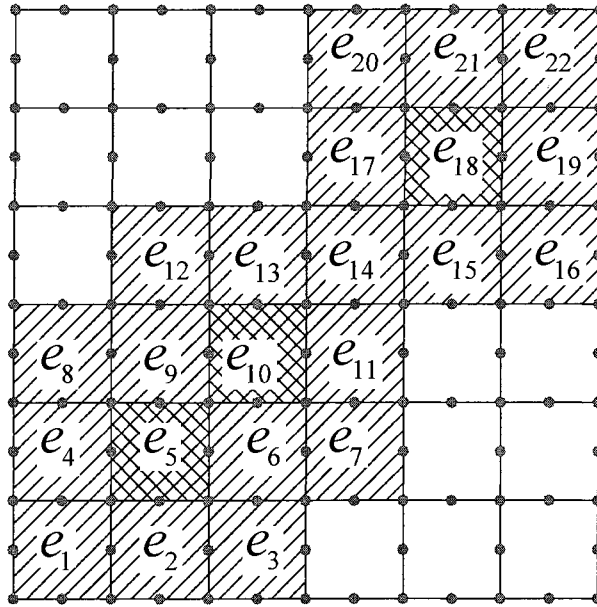
Figure 5.7 The overlapped nonlocal elements.

Table 5.1 The overlapped nonlocal elements

Host elements	Nonlocal elements
$\Downarrow$	$\Downarrow$
$e_5 \longleftrightarrow$	$\left(e_1,\ e_2,\ e_3,\ e_4,\ e_5,\ e_6,\ e_7,\ e_8,\ e_9\right)$
$e_{10} \longleftrightarrow$	$\left(e_5,\ e_6,\ e_7,\ e_9,\ e_{10},\ e_{11},\ e_{12},\ e_{13},\ e_{14}\right)$
$e_{18} \longleftrightarrow$	$\left(e_{14},\ e_{15},\ e_{16},\ e_{17},\ e_{18},\ e_{19},\ e_{20},\ e_{21},\ e_{22}\right)$

If a uniform weighting function is assumed, the nonlocal plastic multiplier $\tilde{\lambda}_i$ for

a host element e_i can be evaluated by

$$\tilde{\lambda}_i = \frac{\sum\limits_{j=0}^{m_i}\left(\hat{\lambda}_i^j A_i^{(j)}\right)}{\sum\limits_{j=0}^{m_i} A_i^{(j)}}\ ,\tag{5.69}$$

where $\hat{\lambda}_i^j$ is the averaged λ over the nonlocal element e_i^j that is attached to host element

e_i. In 2-D cases, Gaussian numerical integration can be used to evaluate $\hat{\lambda}_i^j$, i.e.

$$\hat{\lambda}_i^j = \frac{\displaystyle\sum_{p=1}^{n_{int}^{(1)}} \sum_{q=1}^{n_{int}^{(2)}} G_p G_q \lambda_i^j (\xi_p^{(1)}, \xi_q^{(2)})}{A_i^j}, \qquad (5.70)$$

where $\xi_p^{(l)}, l = 1, 2$, is the coordinate of the pth integration point in the lth dimension, and

G_p is the weight of the pth integration point.

Because of $d\lambda = d\eta$ for the von Mises yield criterion, $\lambda = \eta$ and further $\tilde{\lambda} = \tilde{\eta}$

can be reasonably obtained. Provided that $\tilde{\lambda}_i$ is obtained for a local element e_i, we can

substitute it into the yield function (5.17) to check if the yield condition is satisfied. If it

is, the unbalanced stresses will be computed. However for the higher-order finite element

that involves nonlinear interpolation functions, stresses and strains are usually evaluated

at Gaussian integration points. In this situation, $\tilde{\lambda}_i$ is taken to be constant over the local

element e_i and the values of λ at all the Gaussian points of element e_i are treated to be

equal to $\tilde{\lambda}_i$. This treatment can be equivalently viewed as if the plastic strains are

"smeared" over the whole local element. When a coarse mesh is used in the discretization,

the approximate solution will be very rough. With the refinement of the mesh, the results

will converge to the exact solution.

The significance of using nonlocal plastic strain instead of local plastic strain is

that the variation of plastic strains in one element will affect the plastic strains in other

elements that are within the characteristic region of a RVE. Because of the overlapping of

the nonlocal elements and the application of the nonlocal plastic strains in the yield

function, the nonlocality of plasticity is reflected in the interaction of plastic strains of local elements with one another.

5.4.3 The Stress Updating Algorithm

In the classical computational methodology for plasticity, stress updating is achieved by integrating the local constitutive equations with given initial conditions. Because the local incremental constitutive equations involve plastic strains and state variables only as local quantities, the integration schemes are carried out locally at each material point on the constitutive level. However, for the current nonlocal plasticity model, the plastic multiplier serves as an independent variable, and the yield condition is not locally satisfied. Instead, it is satisfied in an integral sense and the local stress integration scheme does not apply any more. Therefore, the stress updating for nonlocal plasticity has to be carried out on a global level with a regular finite-element procedure combined with the moving elasto-plastic boundary technique.

Recall the linearized Galerkin's Equation (5.61). Taking the assumption of $\tilde{\eta} = \tilde{\lambda}$ for the von Mises yield criterion, the second part of the equation is associated with the truncated Taylor expansion of the yield function at the kth iteration:

$$f(\boldsymbol{\sigma}_{k+1}, \tilde{\lambda}_{k+1}) = f(\boldsymbol{\sigma}_k, \tilde{\lambda}_k) + \frac{\partial f}{\partial \boldsymbol{\sigma}}\bigg|_k : \Delta\boldsymbol{\sigma} - \left(\frac{\partial \sigma_Y(\tilde{\lambda})}{\partial \tilde{\lambda}}\right)\bigg|_k \Delta\tilde{\lambda} = 0, \qquad (5.71)$$

under the yield condition of

$$f(\boldsymbol{\sigma}_k, \tilde{\lambda}_k) = 0. \qquad (5.72)$$

However, because the 2nd and higher order terms of the Taylor expansion of $f(\boldsymbol{\sigma}, \tilde{\lambda})$ at $(\boldsymbol{\sigma}_k, \tilde{\lambda}_k)$ are truncated, the yield condition at the $(k+1)^{th}$ iteration, generally are not exactly satisfied, i.e.

$$f(\boldsymbol{\sigma}_{k+1}, \widetilde{\lambda}_{k+1}) = f(\boldsymbol{\sigma}_k + \Delta\boldsymbol{\sigma}, \widetilde{\lambda}_k + \Delta\widetilde{\lambda}) \neq 0. \tag{5.73}$$

To make the yield condition satisfied at the $(k+1)^{th}$ iteration, namely,

$$f(\boldsymbol{\sigma}_{k+1}, \widetilde{\lambda}_{k+1}) = 0, \tag{5.74}$$

we have to adjust $\Delta\boldsymbol{\sigma}$ or $\Delta\widetilde{\lambda}$ or both. We notice that $\Delta\boldsymbol{\sigma}$ and $\Delta\widetilde{\lambda}$ are solutions of the two coupled field equations and $\Delta\boldsymbol{\sigma}$ is related to $\Delta\widetilde{\lambda}$ by

$$\Delta\boldsymbol{\sigma} = \boldsymbol{C} : \left(\Delta\boldsymbol{\varepsilon} - \Delta\widetilde{\lambda}\boldsymbol{a}\right). \tag{5.75}$$

From a computational standpoint, this problem can always be regarded as strain-driven in the sense that the state variables are computed from a given deformation history [43]. After comparing Equation (5.73) with Equation (5.75), it is indicated that we only need to adjust $\Delta\widetilde{\lambda}$ at the end of the $(k+1)^{th}$ iteration to force the yield condition to be satisfied with $\Delta\boldsymbol{\varepsilon}$ unchanged. Expanding the yield function into a Taylor series at the $(k+1)^{th}$ iteration with respect to $\widetilde{\lambda}$ with nonlinear terms truncated, one can obtain

$$f_{k+1} + \left.\frac{\partial f}{\partial\boldsymbol{\sigma}}\right|_{k+1} : \Delta\boldsymbol{\sigma}' - \left.\left(\frac{\partial\sigma_Y(\widetilde{\lambda})}{\partial\widetilde{\lambda}}\right)\right|_{k+1} \Delta\widetilde{\lambda}' = f_{k+1} - \Delta\widetilde{\lambda}'\boldsymbol{a}_{k+1}^T : \boldsymbol{C} : \boldsymbol{a} - \Delta\widetilde{\lambda}'E_p = 0, \tag{5.76}$$

and

$$\Delta\widetilde{\lambda}' = \frac{f(\boldsymbol{\sigma}_{k+1}, \widetilde{\lambda}_{k+1})}{\boldsymbol{a}_{k+1}^T : \boldsymbol{C} : \boldsymbol{a} + E_p}, \tag{5.77}$$

where the $\Delta\widetilde{\lambda}'$ is the adjustment value of $\Delta\widetilde{\lambda}$. The adjusted value of $\widetilde{\lambda}_{k+1}^{new}$ is

$$\widetilde{\lambda}_{k+1}^{new} = \widetilde{\lambda}_{k+1} + \Delta\widetilde{\lambda}' = \widetilde{\lambda}_k + \Delta\widetilde{\lambda} + \Delta\widetilde{\lambda}'. \tag{5.78}$$

We notice that the solutions of λ are obtained only at the discretized nodal points, whereas the adjustment value $\Delta\widetilde{\lambda}'$ is solved for each element. To make the solution consistent, we have to transform the value of $\Delta\widetilde{\lambda}'$ for each element onto its nodal points.

Because of the nonlocality of $\Delta\tilde{\lambda}'$, the values of λ at all of the nodal points of every nonlocal element attached to the host element that has a nonzero value of $\Delta\tilde{\lambda}'$ should be adjusted. To this end, we use a proportional adjustment approach based on the equivalent averaged plastic multiplier to obtain the adjustment value at each relevant nodal point.

Suppose that an adjustment value, $\Delta\tilde{\lambda}'_{k+1}$, at any material point in the elasto-plastic domain, Ω_{ep}, at the $(k+1)^{th}$ iteration is proportional to the total value $\tilde{\lambda}_{k+1}$ at the same point by the following relationship

$$\Delta\tilde{\lambda}'_{k+1} = Q\tilde{\lambda}_{k+1} , \tag{5.79}$$

where Q is a proportionality factor. For a host element e_i, an adjustment value $\Delta\tilde{\lambda}'^{(i)}_{k+1}$ can be found from Equation (5.77). Notice that $\Delta\tilde{\lambda}'^{(i)}_{k+1}$ is the averaged adjustment value for all of the nonlocal elements attached to host element e_i. To obtain the actual adjustment value for each material point, we need to compute Q first. Considering that the averaged adjustment value should be equal to $\Delta\tilde{\lambda}'^{(i)}_{k+1}$ after adjustment according to Equation (5.78), we have

$$\sum_{j=1}^{m_i} \int_{A_j} \left(Q\tilde{\lambda}_{k+1}\right) dA_i^{(j)} = \Delta\tilde{\lambda}'^{(i)}_{k+1} \sum_{j=1}^{m_i} A_i^{(j)} , \tag{5.80}$$

$$Q = \frac{\Delta\tilde{\lambda}'^{(i)}_{k+1} \sum_{j=1}^{m_i} A_i^{(j)}}{\sum_{j=1}^{m_i} \int_{A_j} \tilde{\lambda}_{k+1} dA_i^{(j)}} , \tag{5.81}$$

where m_i is the number of nonlocal elements for host element e_i.

For a nodal point p that belongs to one of the nonlocal element attached to the host element i, the adjustment value of λ can be obtained by

$$\Delta \widetilde{\lambda}_{k+1}^{\prime (p,i)} = Q \widetilde{\lambda}_{k+1}^{(p,i)} . \tag{5.82}$$

The final adjustment value of λ at nodal point p can be found by

$$\Delta \widetilde{\lambda}_{k+1}^{\prime (p,\bullet)} = \frac{\displaystyle\sum_{i=0}^{n_p-1} \Delta \widetilde{\lambda}_{k+1}^{\prime (p,i)}}{n_p} , \tag{5.83}$$

where n_p is the total number of the host elements that take the point p as a nodal point for one of their nonlocal elements. The updated incremental and total value of λ at point p can be computed as

$$\Delta \lambda_{k+1}^{(p)(new)} = \Delta \lambda_{k+1}^{(p)} + \Delta \lambda_{k+1}^{\prime (p,\bullet)} , \tag{5.84}$$

$$\lambda_{k+1}^{(p)(new)} = \lambda_k^{(p)} + \Delta \lambda_{k+1}^{(p)} . \tag{5.85}$$

From the updated incremental and total values of λ at the nodal points, the nonlocal plastic strain, both incrementally and totally, for each host element, can be obtained by using Equation (5.69), and the updated stress increment can be calculated according to Equation (5.75).

The implementation of the algorithm described above is summarized in Table 5.2.

Table 5.2 The stress updating algorithm

1. Initialize at n^{th} load increment and $(k+1)^{th}$ iteration :

$$\{\varDelta\lambda_h^e\}_{k+1}^n = 0 \; ; \quad \text{If } k+1=1, \quad \text{Then } \{\varDelta\hat{F}_h^e\}_{k+1}^n = \{\varDelta\hat{F}_h^e\}; \quad \text{Else } \{\varDelta\hat{F}_h^e\}_{k+1}^n = 0 \quad \text{End IF}$$

2. Compute stiffness matrix $[K^e]_k = \begin{bmatrix} K_{uu}^e & K_{u\lambda}^e \\ (K_{u\lambda}^e)^T & K_{\lambda\lambda} \end{bmatrix}_k$ according to σ_k^n and λ_k^n

3. Solve $\{\varDelta u_h^e\}_{k+1}^n$ and $\{\varDelta\lambda_h^e\}_{k+1}^n$

$$\begin{Bmatrix} \varDelta u_h^e \\ \varDelta\lambda_h^e \end{Bmatrix}_{k+1}^n = \begin{bmatrix} K_{uu}^e & K_{u\lambda}^e \\ (K_{u\lambda}^e)^T & K_{\lambda\lambda} \end{bmatrix}_k^{-1} \left\{ \begin{matrix} (\varDelta\hat{F}_h^e)_{k+1}^n + (\varDelta\hat{F}_h^e)_k^{nb} \\ 0 \end{matrix} \right\}$$

4. Compute strain, stress and plastic strain

$$\varDelta\tilde{\lambda}_i = \sum_{j=0}^{m_i}\left(\varDelta\hat{\lambda}_i^j A_i^j\right) \Bigg/ \sum_{j=0}^{m_i} A_i^j, \quad \varDelta\hat{\lambda}_i^j = \left(\sum_{p=1}^{n_{int}^{(1)}} \sum_{q=1}^{n_{int}^{(2)}} G_p G_q \lambda_i^j (\xi_p^{(1)}, \xi_q^{(2)})\right)\Bigg/ A_i^j$$

$$\{\varDelta\varepsilon\}_{k+1} = [B]\{\varDelta u_h^e\}_{k+1}, \quad \varepsilon_{k+1} = \varepsilon_k + \varDelta\varepsilon_{k+1}$$

$$\varDelta\sigma_{k+1} = C : \left(\varDelta\varepsilon_{k+1} - \varDelta\tilde{\lambda}_{k+1} a_k\right) \quad \sigma_{k+1} = \sigma_k + \varDelta\sigma_{k+1}$$

5. Check if $f(\sigma_{k+1}, \tilde{\eta}_{k+1}) \geq 0$?

     IF $f(\sigma_{k+1}, \tilde{\eta}_{k+1}) \geq 0$ THEN :

         IF the DOFs of element e_i for λ have been released, THEN :

             Find $\varDelta\tilde{\lambda}'\,_{k+1}^{(p)}$ according to Eq.(107) - (112), then GOTO step 6

         ELSE :

             Release the DOFs of element e_i for λ, then GOTO step 3 to

             recompute $\{\varDelta u_h^e\}_{k+1}^n$, $\{\varDelta\lambda_h^e\}_{k+1}^n$, $\varDelta\tilde{\lambda}_i$, $\{\varDelta\varepsilon\}_{k+1}$, ε_{k+1}, $\varDelta\sigma_{k+1}$, and σ_{k+1}

         END IF

     ENDIF

6. Update plastic strain and stress

$$\varDelta\tilde{\lambda}_i = \varDelta\tilde{\lambda}_i + \varDelta\tilde{\lambda}_i', \quad \{\varDelta\lambda_h^e\}_{k+1}^n = \{\varDelta\lambda_h^e\}_{k+1}^n + \{\varDelta\lambda_h'^e\}_{k+1}^n, \quad \{\lambda_h^e\}_{k+1}^n = \{\lambda_h^e\}_{k+1}^n + \{\varDelta\lambda_h^e\}_{k+1}^n$$

$$\varDelta\sigma_{k+1} = C : \left(\varDelta\varepsilon_{k+1} - \varDelta\tilde{\lambda}_{k+1} a_k\right), \quad \sigma_{k+1} = \sigma_k + \varDelta\sigma_{k+1}$$

7. Compute unbalanced nodal forces

$$\{\varDelta\hat{F}_h^e\}_{k+1}^{unb} = \{\hat{F}_h^e\}_{k+1} - \int_{\Omega^e}[B]^T[\sigma]_{k+1}dV$$

8. Check convergence of the unbalanced nodal forces

     IF $\left\|\{\varDelta\hat{F}_h^e\}_{k+1}^{unb}\right\|_2 \leq$ TOL , THEN : GOTO next load increment $\rightarrow (n+1)$;

     ELSE : $k \leftarrow k+1$ GOTO step 2

     ENDIF

5.5 Simulation of the One-Dimensional Plastic Strain Softening

5.5.1 Problem Definition and the Finite Element Modeling

To illustrate the methodology presented in the preceding sections, we consider the one-dimensional bar subjected to pure tension, which is described Section 3.3 of Chapter 3 (see Figure 3.4). The bar has a length of $L = 100\,mm$ with unit cross-sectional area, $A = 1\ mm^2$, The material parameters are shown in Table 3.1. To focus on the demonstration of the solution strategy, linear plastic strain softening is assumed (see Figure 3.5). The internal length scale $c = 5\,mm$ is assumed and correspondingly, $l_c = 25\,mm$ is taken for the LRVE. Gradient coefficient k is calculated as

$$k = E_p c^2 = -2000\,\text{N/mm}^2 \cdot 25\,\text{mm}^2 = -50000\ \text{N}\,.$$

Table 5.3 The finite element discretization data

n_{total}^{el}	$L_i^{el}\ ^\dagger$(mm)	$n_{nlc}\ ^\S$
21	5	5
45	2.23	11
85	1.17	21
167	0.60	41

† L_i^{el} is the typical length of most elements. Some elements may have the length more or less than the typical length to fit the bar length.

§ n_{nlc} is the number of nonlocal elements for each host element.

The finite element discretization is shown in Figure 3.7. Four different meshes, 21-element, 45-element, 85-element and 167-element, are used, respectively, with a different number of nonlocal elements for each host element (see Table 5.3). To trigger the plastic strain localization, the local element located in the center of the bar for each

mesh is treated as a weak element with the yield strength 10% off the normal yield strength σ_Y. The size of the weak element decreases with the refinement of the mesh.

5.5.2 Numerical Results

The effective plastic strain distributions and the load-displacement curves from the four different meshes at $u = 0.02\,\text{mm}$ are shown in Figure 5.8 and Figure 5.9, respectively. In Figure 5.8, we can see that the plastic strain, resulting from the nonlocal model, is localized into a region that spans over several elements after the weak element yields, whereas the plastic strain from the classical model (local model) is localized into only one single element—the weak element. With refinement of meshes, the size of the localization zone is almost unchanged except that there is a little difference between the results of the 21-element mesh and that of other three meshes. Since the 21-element mesh is relatively coarse compared with other meshes, this result is reasonable. Figure 12 also shows that the distributions of the plastic strain over the localization zone for the 21-element, 45-element, 85-element, and 167-element cases are very similar and are of harmonic type, which agrees with the solution in de Borst and Mühlhaus [63] and the theoretical results obtained in Chapter 4. We notice that the four distributions tend to converge towards a steady distribution with mesh refinement.

Figure 5.9 shows the well-posedness of the plastic strain softening problem with the nonlocal model employed. The post-peak branch of the load-displacement curve descends gradually after yielding of the weak element. This response is consistent with the reasonable plastic distribution that is associated with a localization zone over more than one element. For an ill-posed strain softening problem, the post-peak branch of the load-displacement curve is not unique and generally depends on the mesh pattern and the

stress updating algorithm [97, 98]. If a small positive plastic modulus and an algorithm of Newton's type are used, the post-peak response will be an all-of-a-sudden decrement of the applied load, followed by a rapid increment of displacement with a constant residual load that is either very small or zero (see Figure 3.9). The results in Figure 5.9 also show the convergence of the post-peak branch of the load-displacement curve, even though the curve from the 21-element mesh deviates somewhat from the results of other meshes due to the coarse mesh.

The total strain distributions of the bar after yielding for different meshes at $u = 0.0125$ mm are shown in Figure 5.10. The elements other than those in the localization zone experience elastic deformation while the elements within the localization zone are in the elasto-plastic state. Most of the deformation of the bar after yielding comes from the plastic deformation of the localization zone. Figure 5.11 shows the evolution of the plastic distribution over the bar at the end displacements of $u = 0.01$ mm, 0.0125 mm, 0.015 mm and 0.02 mm, respectively. It is shown that the localization zone remains unchanged with increased end displacement after triggering of the localization. The distributions of plastic strain at each loading stage after localization are all of similar harmonic type.
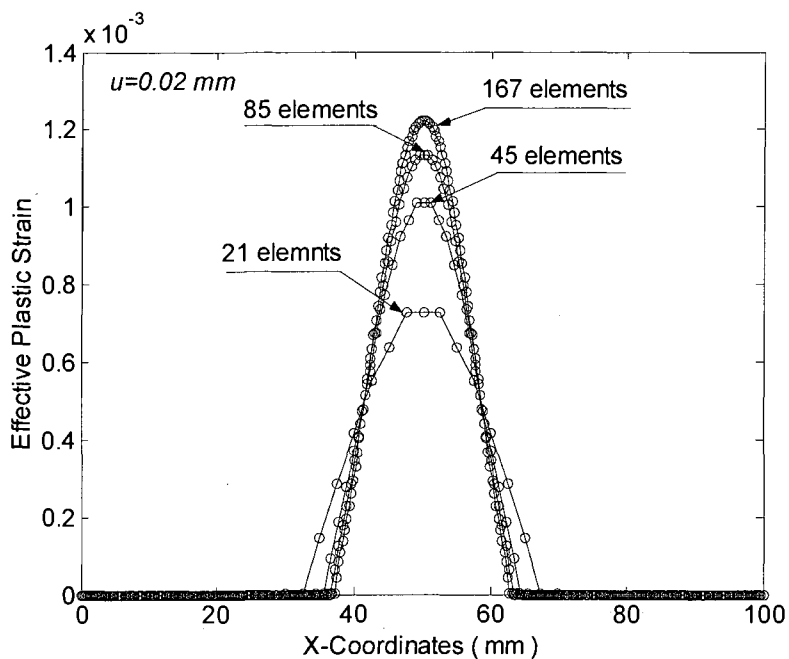
Figure 5.8 Mesh independent result: the effective plastic strain distribution of the bar under tension with the nonlocal model.
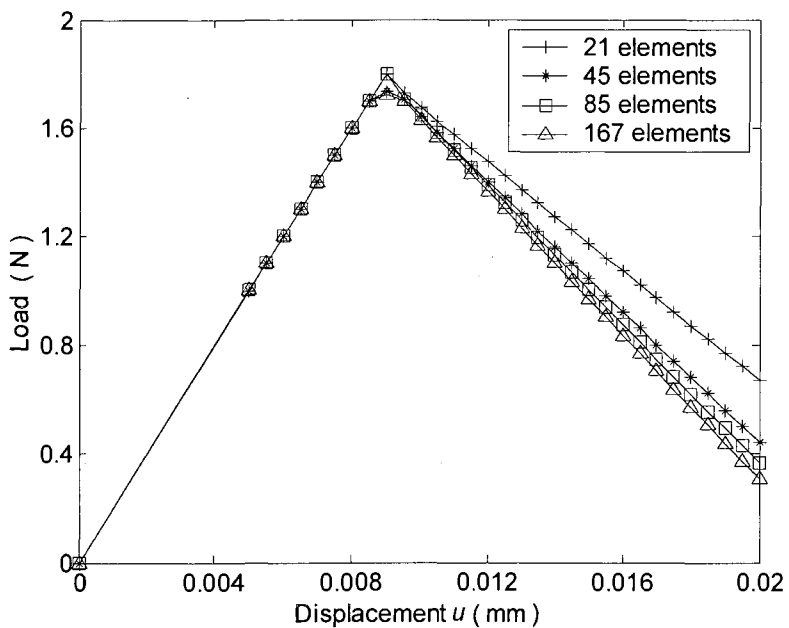
Figure 5.9 Mesh-independent results: load-displacement curve of the bar under tension with the nonlocal model.
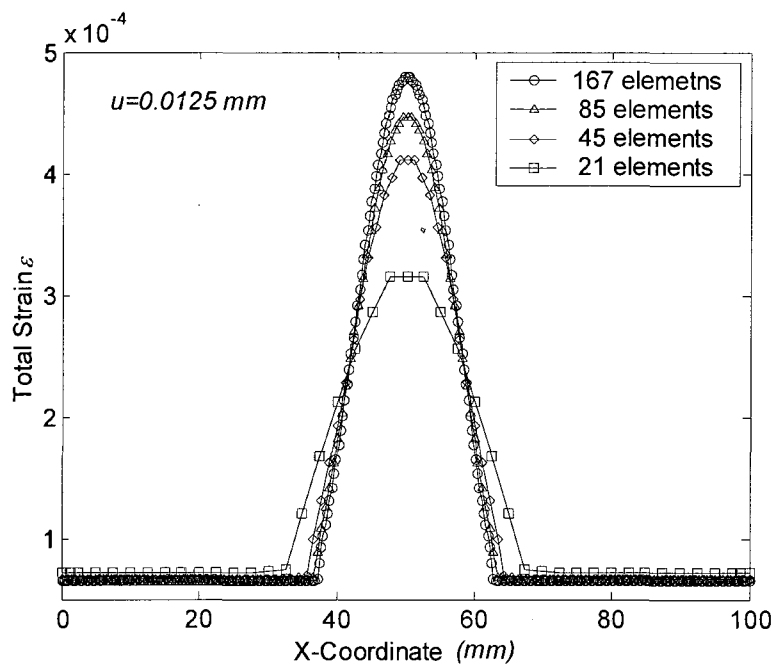
Figure 5.10 Mesh-independent results: the total strain distribution of the bar under tension at $u = 0.0125$ mm with the nonlocal model.
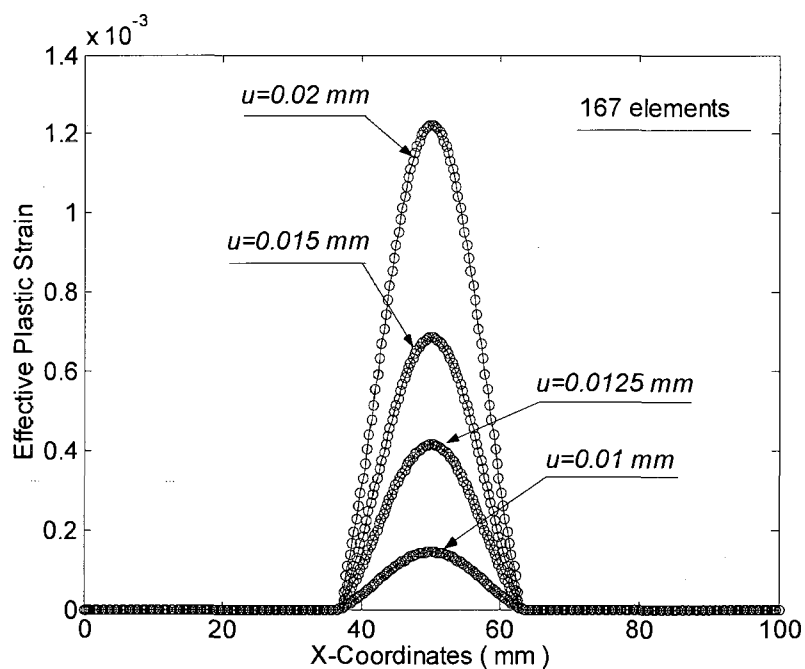
Figure 5.11. Mesh-independent results: evolution of the effective plastic strain distribution of the bar under tension at different end displacements with the nonlocal model.

5.6 <u>Summary</u>

A new methodology that combines the nonlocal plasticity model with C^0 finite elements is proposed to simulate strain localization. The nonlocal field is introduced as a weighted averaging of its local counterpart over a representative volumetric element (RVE), and therefore is of integral type. Based on the uniformly distributed weighting function and the truncated Taylor expansion of the local field at the center of RVE, an approximate expression of the integral-type nonlocal model is derived, which is a 2nd order differential equation. This approximate expression is similar to the explicit gradient model. Thus, a link is established between an integral type nonlocal model and its equivalent differential form. This link serves two purposes: on the one hand, the consistency equation, which originally is an algebraic equation with respect to the nonlocal plastic multiplier (or state variable), becomes a 2nd order differential equation with respect to the local plastic multiplier. To solve this differential consistency equation in the finite element context, we can derive its variational form with the local plastic multiplier as an independent field variable; on the other hand, to avoid using C^1 elements in the finite element approximation to evaluate the 2nd order gradient of the local plastic multiplier field, we can take advantage of its integral-type nonlocal model to evaluate its nonlocal counterpart. With this method, C^0 elements are efficient enough for the finite element approximation of the plastic multiplier field.

Variational formulation and Galerkin's equations of the two coupled fields, displacement and plastic multiplier fields, are presented based on the C^0 element. A solution strategy and an algorithm are constructed to solve these coupled nonlinear systems of field equations. The method of solution is still within the framework of

Newton's type with linearization of nonlinear operator equations. However, because the problem is displacement-driven, the convergence is controlled by the norm of unbalanced nodal forces, which is reflected in the linearized equation (95). Stress integration is implemented by means of an algorithm that employs a so-called moving boundary technique and nonlocal elements, which are summarized as follows:

(i) If the stress state of an element in an averaged sense satisfies the yield condition, the degrees of freedom for the plastic multiplier field at all nodal points of this element are activated, and Equation (5.61) is resolved with the same applied loads. With load increased, more nodal points are activated regarding the plastic multiplier and the elasto-plastic boundary moves with increased plastic deformation. We use this technique to control the exclusion and inclusion of yield conditions in the governing equations.

(ii) A nonlocal plastic multiplier λ for a local element is evaluated as an averaging of local plastic multiplier over all of its nonlocal elements. A nonlocal element attached to a local element (also called a host element) is one of the local elements included in a region that has the characteristic size of a RVE. Nonlocal elements are generally overlapped with each other, and it is just this overlapping that contributes to the nonlocality of plastic strains for local elements.

Numerical simulation for a 1-D bar under tension shows that the methodology presented is capable of giving rise to a mesh independent solution of strain localization. The size of the localization zone will approach to a limit value when the mesh is refined, and this size is roughly equal to the characteristic size of the RVE. The plastic strain distributions and load-displacement curves are both convergent and realistic.

CHAPTER 6

CONCLUSIONS AND FUTURE WORK

Within the frame of the classical continuum mechanics, a rate-independent strain softening plasticity model is formulated to simulate the strain localization caused by plastic strain softening. A necessary condition for the occurrence of localized plastic deformation is $E_p < 0$. Based on the incremental constitutive equation, the variational equation of the incremental elasto-plastic boundary value problem is developed and the finite element approximation of this variational equation is formulated through Galerkin's method. To solve the resulting nonlinear system of equations, a method of Newton's form is applied. A forward-Euler integration algorithm is developed to integrate the incremental constitutive equation.

Two computer programs, EP1D and EPLAS, are developed to simulate strain localization for 1-D and 2-D problems, respectively. Strain localization and shear band localization is well demonstrated through 1-D and 2-D numerical examples. It is shown that the simulation result of the size of the localization zone and the load-displacement response are mesh-dependent. This mesh-dependency is caused by the loss of ellipticity of the governing differential equations that come from the classical continuum mechanics-based strain softening plasticity model. Numerical examples also show that the location of the shear band is sensitive to the location of the weak zone. As an extreme

case of the strain softening plasticity, a perfect plasticity model is also used in the simulation, and the results are compared with those from the strain softening model. The comparison indicates that the shear band patterns and load-displacement responses for these two models are obviously different. The reason for this difference is that the governing differential equations for the two models are different even though both models can exhibit the material instability and the strain localization.

To regularize the mesh-dependency and make the boundary-value problem well-posed, a new methodology that combines the nonlocal plasticity model with the C^0 finite elements is proposed to simulate strain localization. In this model, the nonlocal field is introduced as a weighted averaging of its local counterpart over a representative volumetric element (RVE), and therefore is of integral type. Based on the uniformly distributed weighting function and the truncated Taylor expansion of the local field at the center of RVE, an approximate expression of the integral-type nonlocal model is derived, which is a 2nd order differential equation. This approximate expression is similar to the explicit gradient model. Thus, a link is established between an integral type nonlocal model and its equivalent differential form. This link serves two purposes: on the one hand, the consistency equation, which originally is an algebraic equation with respect to the nonlocal plastic multiplier (or state variable), becomes a 2nd order differential equation with respect to the local plastic multiplier. To solve this differential consistency equation in the finite element context, we can derive its variational form with the local plastic multiplier as an independent field variable; on the other hand, to avoid using C^1 element in the finite element approximation to evaluate the 2nd order gradient of the local plastic multiplier field, we can take advantage of its integral-type nonlocal model to evaluate its

nonlocal counterpart. With this method, the C^0 elements are efficient enough for the finite element approximation of the plastic multiplier field.

Variational formulation and Galerkin's equations of the two coupled fields, displacement field and plastic multiplier field, are presented based on the C^0 element. A solution strategy and an algorithm are constructed to solve these coupled nonlinear systems of field equations. The method of solution is still within the framework of Newton's type with linearization of nonlinear operator equations. However, because the problem is displacement-driven, the convergence is controlled by the norm of unbalanced nodal forces. Stress integration is implemented by means of an algorithm that employs a so-called moving boundary technique and nonlocal elements.

Analytical solutions of two 1-D bars under tension with gradient elasticity and gradient plasticity are compared to identify the correct boundary conditions for the 2nd order differential constitutive equations resulting from the above mentioned nonlocal model. It is shown that the Dirichlet boundary conditions force the strain localized into a small region and remove the mesh-dependency in the modeling of strain localization and thus are appropriate boundary conditions for the gradient plasticity problems.

Numerical simulation for a 1-D bar under tension shows that the methodology presented here is capable of giving rise to a mesh independent solution of strain localization. The size of the localization zone will approach to a limit value when the mesh is refined, and this size is roughly equal to the characteristic size of the RVE. The plastic strain distributions and load-displacement curves are both convergent and realistic.

The future studies should include the following aspects:

1. Simulation of the 2-D strain localization using the nonlocal model and C^0 elements. The 2-D problems are more complex than 1-D problem regarding the nonlocality in that the uniformly distributed weighting function may result in the divergence or oscillation of the stress integration process. This result occurs because the yield criterion is not satisfied at every material point; instead, it is only satisfied in the distributive sense. Thus, the weighting function of the plastic multiplier will have a major influence on the satisfaction of the yield criterion.

2. Triangular constant strain elements, 9-noded elements and other higher order elements should be used in the simulation to examine the effect of different types of elements on the initiation and propagation of the shear band pattern.

3. The implicit stress integration algorithms should be developed to improve the accuracy and convergence property. In the current model and the computational procedures, only the explicit algorithm and inconsistent tangent modulus matrix are used. This choice only meets the research need. If the model and the procedures are to be incorporated into commercial software packages, an efficient stress integration algorithm is in demand. Development of a more efficient and fast stress integration algorithm is always a difficult task for the simulation of elasto-plastic problems.

4. Further research into application of the current model and the computational procedures in engineering practice. The application should include incorporating the current model and the procedures into commercial software packages and employing the computer program presented in this dissertation to simulate the

strain localization phenomena in geotechnical engineering, trenchless engineering,

and structural engineering.

APPENDIX A

THE RELATION BETWEEN THE PLASTIC MULTIPLIER AND THE EQUIVALENT PLASTIC STRAIN FOR THE VON MISES YIELD FUNCTION AND THE ASSOCIATIVE FLOW RULE

The von Mises yield function reads

$$f(\boldsymbol{\sigma}, \varepsilon_{eq}^q) := \sqrt{3J_2} - \sigma_Y(\varepsilon_{eq}^p) = 0, \tag{A.1}$$

where

$$
\begin{aligned}
J_2 &= \frac{1}{2} S_{ij} S_{ij} = \frac{1}{2}\left[S_x^2 + S_y^2 + S_z^2 + 2\left(\tau_{xy}^2 + \tau_{yz}^2 + \tau_{zx}^2\right)\right] \\
&= \frac{1}{6}\left[(\sigma_x - \sigma_y)^2 + (\sigma_y - \sigma_z)^2 + (\sigma_z - \sigma_x)^2 + 6\left(\tau_{xy}^2 + \tau_{yz}^2 + \tau_{zx}^2\right)\right] \tag{A.2} \\
&= \frac{1}{6}\left[(\sigma_1 - \sigma_2)^2 + (\sigma_2 - \sigma_3)^2 + (\sigma_3 - \sigma_1)^2\right].
\end{aligned}
$$

The equivalent plastic strain ε_{eq}^p is defined by

$$d\varepsilon_{eq}^p = \sqrt{\tfrac{2}{3} d\varepsilon_{ij}^p d\varepsilon_{ij}^p}, \tag{A.3}$$

$$\varepsilon_{eq}^p = \int d\varepsilon_{eq}^p. \tag{A.4}$$

The associative flow rule is expressed as

$$d\varepsilon_{ij}^p = d\lambda \frac{\partial f}{\partial \sigma_{ij}}, \tag{A.5}$$

154

Substituting Equation (A.5) into Equation (A.3) gives

$$d\varepsilon_{eq}^{p} = d\lambda \sqrt{\frac{2}{3} \frac{\partial f}{\partial \sigma_{ij}} \frac{\partial f}{\partial \sigma_{ij}}} \ . \tag{A.6}$$

Using Equation (A.1), we can obtain the partial derivative of $f(\boldsymbol{\sigma}, \varepsilon_{eq}^{q})$ with respect to σ_{ij}

$$\frac{\partial f}{\partial \sigma_{ij}} = \frac{\partial f}{\partial J_2} \frac{\partial J_2}{\partial \sigma_{ij}} = \frac{\sqrt{3}}{2\sqrt{J_2}} \frac{\partial J_2}{\partial \sigma_{ij}} \ . \tag{A.7}$$

From Equation (A.2), one can obtain that

$$\frac{\partial J_2}{\partial \sigma_{ij}} = S_{ij} \ . \tag{A.8}$$

Then we have

$$\frac{\partial f}{\partial \sigma_{ij}} = \frac{\sqrt{3}}{2\sqrt{J_2}} S_{ij} \ . \tag{A.9}$$

Substituting Equation (A.9) into (A.6) yields

$$d\varepsilon_{eq}^{p} = d\lambda \sqrt{\frac{2}{3}\left(\frac{\sqrt{3}}{2\sqrt{J_2}} S_{ij}\right)\left(\frac{\sqrt{3}}{2\sqrt{J_2}} S_{ij}\right)} = d\lambda \sqrt{\frac{S_{ij} S_{ij}}{2 J_2}} \ . \tag{A.10}$$

Since $J_2 = \frac{1}{2} S_{ij} S_{ij}$, it follows that

$$d\varepsilon_{eq}^{p} = d\lambda \ . \tag{A.11}$$

Thus, we conclude that for the von Mises yield function and the associative flow rule, the equivalent plastic strain increment is equal to the plastic multiplier.

BIBLIOGRAPHY

[1]   Desrues, J. "Experimental characterization of failure, degradation, and instability in geomaterials," PowerPoint slides, Laboratoire 3S Sols, solids, Structures, Université de Grenoble –CNRS, France, October 15, 2004.

[2]   Viggiani, G., Lenoir, N., Bésuelle, P., Di Michiel, M., Marello, S., Desrues, J., and Kretzschmer, M. "X-ray micro tomography characterization of strain localization upon deviatoric loading of saturated fine-grained stiff soils," *Comptes Rendus Mecanique* 2004; **332**(10):819-826.

[3]   Alshibli, K. A. and Sture, S. "Shear band formation in plane strain experiments of sand," *Journal of Geotechnical and Geoenvironmental Engineering* 2000; **126**(6):495-503.

[4]   Ehlers, W., Scholz, B., Ammann, M., Markert, M. "Material behavior and localization phenomena in the theory of porous media (TPM)," *Research Project A6*, Institute of Applied Mechanics (CE), Universität Stuttgart, 2004; 11-12.

[5]   Asaro, R. J. "Geometrical effects in the inhomogeneous deformation of ductile single crystals," *Acta Metallurgica* 1979; **27**:445-453.

[6]   Chang, Y. W., and Asaro, R. J. "Lattice rotations and localized shearing in single crystals," *Archives of Mechanics* 1980; **32**:369-388.

[7]   Anand, L., and Spitzig, W. A. "Initiation of localized shear bands in plane strain," *Journal of Mechanics and Physics in Solids* 1980; **28**:113-128.

[8]   Wang, W. M., "Stationary and propagative instabilities in metals – A computational point of view," Dissertation, Delft University of Technology; Delft, 1997.

[9]   Desrues, J., Chambon, R., Mokni, M., and Mazerolle, F. "Void ratio evolution inside shear bands in triaxial sand specimens studied by computed tomography," *Géotechneque* 1996; **46**:529-546.

[10]   Vardoulakis, I. "Shear band inclination and shear modulus of sand in biaxial test," *International Journal for Numerical and Analytical Methods in Geomechanics* 1980; **4**:103-119.

[11] Tvergarrd, V., Needleman A., and Lo, K. K. "Finite element analysis of localization in plasticity," in: Oden, J. T. and Carey, G. F. eds. *Finite Elements – Special problems in Solid Mechanics*. Prentice Hall: Englewood Cliffs, NJ, 1983, **5**:94-157.

[12] Atkinson, J. *An Introduction to the Mechanics of Soils and Foundations: through Critical State Soil Mechanics*. McGraw-Hill: New York, 1993.

[13] Jaeger, J. C. and Cook, N. G. W. *Fundamentals of Rock Mechanics*. 2nd ed. Chapman and Hall: London, 1976.

[14] Chen, W. F. *Plasticity in Reinforced Concrete*. McGraw-Hill: New York, 1982.

[15] Read, H. E. and Hegemier, G. A. "Strain softening of rock, soil and concrete – A review article," *Mechanics and Materials* 1984; **3**:271-294.

[16] Regueiro, R. A. *Finite Element Analysis of Strain Localization in Geomaterials Taking a Strong Discontinuity Approach*. Dissertation, Stanford University, 1998.

[17] Imbeni, V., Mehta, A., Robertson, S.W., Duerig, T.W., Pelton, A. and Ritchie, R.O. "On the mechancal behavior of nitinol under multiaxial loading conditions and in situ synchrotron X-ray diffraction," *http://www.lbl.gov/Ritchie/Library/PDF /SMSTfinalfig.doc*.

[18] Wood, D. M. *Soil Behavior and Critical State Soil Mechanics*. Cambridge University Press: New York, 1990.

[19] Seydel, R. *Practical Bifurcation and Stability Analysis—From Equilibrium to Chaos*. Spring-Verlag: New York, 1994.

[20] Hale, J. K. *Topics in Dynamic Bifurcation Theory*. Regional Conference Series in Mathematics, No.47, Conference Board of the Mathematical Sciences, Expository Lectures from the CBMS Regional Conference held at the University of Texas at Arlington, June 16–20, 1980.

[21] Zwillinger, D. Handbook of Differential Equations. Academic Press, Inc.: San Diego, 1989.

[22] Tvergarrd, V., Needleman, A., and Lo, K. K. "Flow localization in the plane strain tensile test," *Journal of the Mechanics and Physics of Solids* 1981; **29**:115–142.

[23] Belytschko, T, and Mish, K. "Computability in non-linear solid mechanics," *International Journal for Numerical Methods in Engineering* 2001; **52**:3–21.

[24]   Hadamard, J. *Leçons sur la Propagation des Ondes et les Équations de L'Hydrodynamique*. Librairie Scentifique A. Hermann: Paris, 1903.

[25]   Drucker, D. C. "Some implications of work hardening and ideal plasticity," *Quarterly of Applied Mathematics* 1950; **7**:411–418.

[26]   Thomas, T. Y. *Plastic Flow and Fracture in Solids*. Academic Press: New York, 1961.

[27]   Mandel, J. "Conditions de stabilité et postulat de Drucker," *Rheology and Soil Mechanics*, eds. J. Kravtchenko and P. M. Sirieys. 58–68. Springer-Verlag: Berlin, 1966.

[28]   Hill, R. "Acceleration waves in solids," *Journal of Mechanics and Physics in Solids* 1962, **10**:1-16.

[29]   Rice, J. R. "The localization of plastic deformation," in *Theoretical and Applied Mechanics*, Proceedings of the 14th International Congress on Theoretical and Applied mechanics, ed. W. T. Koiter. 207-220. Amersterdam, North-Holland, 1976.

[30]   Hill, R. "A general theory of uniqueness and stability in elastic-plastic solids," *Journal of Mechanics and Physics in Solids* 1958, **8**:236–249.

[31]   Leroy, Y. and Ortiz, M. "Finite element analysis of strain localization in frivtinal materials," *International Journal for Numerical and Analytical Methods in Geomechanics* 1989; **13**:53–74.

[32]   Rudnicki, J., W. and Rice, J. R. "Conditions for the localization of deformation in pressure-sensitive dilatant materials," *Journal of Mechanics and Physics in Solid* 1975; **23**:371–394.

[33]   Ottosen, N. S. and Runesson, K. "Properties of discontinuous bifurcation solutions in elasto-plasticity," *International Journal of Solids and Structures* 1991, **27**:401–421.

[34]   Bardet, J. P. "A comprehensive review of strain localization in elasto-plastic soils," *Computers and Geotechnics* 1990; **10**:163–188.

[35]   Neilsen, M. K. and Schreyer, H. L. "Bifurcations in elastio-plastic materials," *International Journal of solids and Structures* 1993; **30**:521–544.

[36]   de Borst, R., Sluys, L. J., Mühlhaus, H. -B., Pamin, J. "Fundamental issues in finite element analyses of localization of deformation," *Engineering Computations* 1993; **10**:99–121.

[37] Tomita, Y., "Simulations of plastic instabilities in solid mechanics," *Applied Mechanics Reviews* 1994; **47** (No.6, part 1):171–205.

[38] Bigoni, D., and Hueckel, T. "Uniqueness and localization—associative and nonassociative elastoplasticity," *International Journal of Solids and Structures* 1991; **28**:197–213.

[39] Hill, R. *Mathematical Theory of Plasticity*. Oxford University Press: Oxford, U. K., 1950.

[40] Owen, D. R. J., and Hinton, E. *Finite Element in Plasticity: Theory and Practice*, Pineridge Press Limited: Swansea, U. K. 1980.

[41] Mendelson, A. *Plasticity: Theory and Application*, The Macmillan Company: New York, 1968.

[42] Han, W. and Reddy B. D. Plasticity: Mathematical Theory and Numerical Analysis.Springer-Verlag: New York, 1999.

[43] Simo, J. C., and Hughes, T. J. R. *Computational Inelasticity*. Springer-Verlag: New York, 1998.

[44] Washizu, K. *Variational Methods in Elasticity and Plasticity*. Pergamon Press: New York, 1982.

[45] Oden, J. T. *Finite Elements of Nonlinear Continua*. McGraw-Hill: New York, 1972.

[46] Becker, E. B., Carey, G. F., and Oden, J. T. *Finite Elements: An Introduction*, Volume I. Prentice-Hall: Englewood Cliffs, N. J., 1981.

[47] Hughes T. J. R. *Finite Element Method: Linear Static and Dynamic Finite Element Analysis*. Prentice-Hall: Englewood Cliffs, N. J., 1987.

[48] Bathe, K. J. *Finite Element Procedures*. Prentice-Hall: Englewood Cliffs, N. J., 1997.

[49] Rheinboldt, W. C. *Methods for Solving Systems of Nonlinear Equations*. Society for Industrial and Applied Mathematics, 1998.

[50] Crisfield, M. A. *Non-Linear Finite Element Analysis of Solids and Structures*. Volume 1, John Wiley & Sons, Inc: New York, 1997.

[51] Smith, I. M. and Griffiths, D. V. *Programming the Finite Element Methods*. 4th Ed, John Wiley and Sons, Ltd: New York, 2004.

[52]   Conte, S. D., and Boor, C. *Elementary Numerical Analysis: An Algorithmic Approach*. McGraw-Hill: New York, 1980.

[53]   Zienkiewicz, O. C. *The Finite Element Method*. 3rd Ed. McGraw-Hill: New York, 1977.

[54]   Aifantis, E. C. "Gradient deformation models at nano, micro, and macro scales," *Journal of Engineering Materials and Technology* 1999; **121**:189–202.

[55]   Aifantis, E. C. "On the role of gradients in the localization of deformation and fracture," *International Journal of Engineering Science* 1992; **30**:1279–1299.

[56]   Eringen, A. C. "On differential equations of nonlocal elasticity and solutions of screw dislocation and surface waves," *Journal of Applied Physics* 1983; **54**:4703–4710.

[57]   Bažant, Z. P. and Jirásek M. "Nonlocal integral formulations of plasticity and damage: Survey and progress," *Journal of Engineering Mechanics* 2002; **128**:1119–1149.

[58]   Mühlhaus, H.–B. and Aifantis, E. C. "A variational principle for gradient plasticity," *International Journal of Solids and Structures* 1991; **28**:845–857.

[59]   Altan, B. S. and Aifantis, E. C. "On some aspects in the special theory of gradient elasticity, " *Journal of the Mechanical Behavior of Materials* 1997, **8**:231–282.

[60]   de Borst, Sluys, R., L. J. Mühlhaus, H.–B. and Pamin J. "Fundamental issues in finite element analyses of localization of deformation," *Engineering Computations* 1993; **10**:99–121.

[61]   Polizzotto, C. "Gradient elasticity and nonstandard boundary conditions," *International Journal of Solids and Structures* 2003; **40**:7399–7423.

[62]   Askes, H., Suiker, A. S. J. and Sluys, L. J. "A classification of higher-order strain-gradient models–linear analysis," *Archives of Applied Mechanics* 2002; **72**:171–188.

[63]   de Borst, R., Mühlhaus, H.–B. "Gradient-dependent plasticity: formulation and algorithm aspects," *International Journal for Numerical Methods in Engineering* 1992; **35**:521–539.

[64]   de Borst, R., Pamin, J. "Some novel developments in finite element procedures for gradient-dependent plasticity," *International Journal for Numerical Methods in Engineering* 1996; **39**:2477- 2505.

[65]   Ortiz, M., Leroy, Y., Needleman, A. "A finite element method for localized failure analysis," *Computer Methods in Applied Mechanics and Engineering* 1987; **61**:189–214.

[66]   Needleman, A., Ortiz, M. "Effect of boundaries and interfaces on shear-band localization," *International Journal of Solids and Structures* 1991; **28**:859–877.

[67]   Schaeffer, D., "Instability and ill-posedness in the deformation of granular materials," *International Journal of Numerical and Analytical Methods in Geomechanics* 1990; **14**:253–278.

[68]   Peerlings, R. H. J., de Borst, R., Brekelmans, W. A. M., Geers, M. G. D. "Localization issues in local and nonlocal continuum approaches to fracture," *European Journal of Mechanics A/Solids* 2002; **21**:175–189.

[69]   Borja, R. I. "Bifurcation of elastoplastic solids to shear band mode at finite strain," *Computer Methods in Applied Mechanics and Engineering* 2002; **191**:5287–5314.

[70]   Stein. E., Steinmann, P., Miehe, C. "Instability phenomena in plasticity: Modeling and computation," *Computational Mechanics* 1995; **17**:74–87.

[71]   Pietruszczak, S. T., Mróz, Z. "Finite element analysis of deformation of strain-softening materials," *International Journal for Numerical Methods in Engineering* 1981; **17**:327–334.

[72]   Borja, R. I., Regueiro, R. A. "Strain localization in frictional materials exhibiting displacement jumps," *Computer Methods in Applied Mechanics and Engineering* 2001; **190**:2555–2580,

[73]   Borja, R. I. "A finite element model for strain localization analysis of strong discontinuous field based on standard Galerkin approximation," *Computer Methods in Applied Mechanics and Engineering* 2000;**190**:1529–1549.

[74]   Simo, J. C., Oliver, J., Armero, F. "An analysis of strong discontinuities induced by strain-softening in rate-independent inelastic solids," *Computational Mechanics* 1993; **12**:277–296.

[75]   Eringen, A. C. "Vistas of nonlocal continuum physics," *International Journal of Engineering Science* 1992; **30**:1551–1565.

[76]   Eringen, A.C. "Theory of nonlocal plasticity," *International Journal of Engineering Science* 1983; **21**:741–751.

[77]   Toupin, R. A. "Elastic materials with couple-stresses," *Archive for Rational Mechanics and Analysis* 1962; **11**:385–414.

[78] Mindlin, R. D. "Micro-structure in linear elasticity," *Archive for Rational Mechanics and Analysis* 1964; **16**:51–78.

[79] Al Hattamleh, O., Muhunthan, B., Zbib, H. M. "Gradient plasticity modeling of strain localization in granular materials," *International Journal for Numerical and Analytical Methods in Geomechanics* 2004; **28**:465–481.

[80] Peerlings, R. H. J., Geers, M. G. D., de Borst, R., Brekelmans, W. A. M. "A critical comparison of nonlocal and gradient-enhanced softening continua," *International Journal of Solids and Structures*, 2001; **38**:7723–7746.

[81] Zbib, H. M. "On the gradient-dependent theory of plasticity and shear banding," *Acta Mechanica* 1992; **92**:209–225.

[82] Vardoulakis, I., Sulem, J. *Bifurcation Analysis in Geomechanics*. Blackie Academic & Professional, Chapman & Hall, 1995.

[83] Tejchman, J., Wu, W. "Dynamic patterning of shear bands in Cosserat continuum," *Journal of Engineering Mechanics* 1997; **123**: 123–134.

[84] Lages, E. N., Paulino, G. H., Menezes, I. F. M., Silva, R. R. "Nonlinear finite element anlaysis using object-oriented philosophy–Application to beam elements and the Cosserat continuum," *Engineering with Computers* 1999; **15**:73–89.

[85] Tabarraei, A. *Numerical simulation of strain localization using Cosserat continuum theory*. Department of Civil and Environmental Engineering, University of California, Davis, 2004.

[86] Bažant, Z. P., Chang, T-P. "Instability of nonlocal continuum and strain averaging," *Journal of Engineering Mechanics* 1984; **110**:1441–1450.

[87] Bažant, Z. P., Chang, T-P. "Nonlocal finite element analysis of strain softening solids," *Journal of Engineering Mechanics* 1987; **113**:89–105.

[88] Voyiadjis, G.Z., Dorgan, R. J. "Bridging of length scales through gradient theory and diffusion equation of dislocations," *Computer Methods in Applied Mechanics and Engineering* 2004; **193**: 1671–1692.

[89] Abu Al-Rub, R. K., Voyiadjis, G. Z. "A direct finite element implementation of the gradient-dependent theory," *International Journal for Numerical Methods in Engineering* 2005; **63**:603–629.

[90]   Meftah, F., Pijaudier-Cabot, G., Reynouard, J. M. "A C^0 finite element in gradient plasticity for localized failure modes analysis. in: S. Idelsohn, E. Oñate and E. Dvorkin (Eds.), *Computational Mechanics, New Trends and Applications*. CIMNE: Barcelona, Spain, 1998.

[91]   Bažant, Z. P., Lin, F–B. "Nonlocal smeared cracking model for concrete fracture," *Journal of structural Engineering* 1988; **114**(11):2493–2510.

[92]   Stromberg, L., Ristinmaa, M. "FE-formulation of a nonlocal plasticity theory," *Computer Methods in Applied Mechanics and Engineering* 1996; **136**:127–144.

[93]   Vardoulakis, I. "2nd gradient flow theory of plasticity," in: Darve, F. and Vardoulakis, I. (editors), *Degradations and Instabilities in Geomaterials*, Chapter 5, CISM, DIGA-sponsored Course, Springer, 2004.

[94]   Vardoulakis, I, and Aifantis, E. C. "A gradient flow theory of plasticity for granular materials," *Acta Mechanica* 1991; **87**:197–217.

[95]   Ramaswamy, S., and Aravas, N. "Finite element implementation of gradient plasticity models Part I: Gradient-dependent yield functions," *Computer Methods in Applied Mechanics and Engineering* 1998; **163**:11–32.

[96]   Ramaswamy, S., Aravas, N. "Finite element implementation of gradient plasticity models Part II: Gradient-dependent evolution equations," *Computer Methods in Applied Mechanics and Engineering* 1998; **163**:33–35.

[97]   Schreyer, H. L., and Chen, Z. "One-dimensional strain softening with localization," *Journal of Applied Mechanics* 1986; **53**:791–797.

[98]   Crisfield, M. A. *Non-Linear Finite Element Analysis of Solids and Structures: Volume2, Advanced Topics*. 1st ed., John Wiley & Sons, Inc: New York, 1997.